Colloidal PbSe/CdSe Heteronanocrystals

atomic configuration, electronic structure and optical properties

Cover design by author
TEM images taken by Stephan Zevenhuizen
ISBN: 978-90-393-5831-3

Colloidal PbSe/CdSe Heteronanocrystals

atomic configuration, electronic structure and optical properties

Colloïdale PbSe/CdSe Heteronanokristallen

atomaire configuratie, elektronische structuur en optische eigenschappen

(met een samenvatting in het Nederlands)

Proefschrift

te verkrijging van de graad van doctor aan de Universiteit Utrecht op gezag van de rector magnificus, prof. dr. G.J. van Zwaan, ingevolge het besluit van het college voor promoties in het openbaar te verdedigen op woensdag 26 september 2012 des middags te 2.30 uur

door

Dominika Grodzińska

geboren op 12 februari 1983, te Krapkowice, Polen

Promotor: Prof. dr. D. Vanmaekelbergh
Co-promotor: Dr. C. de Mello Donegá

…moim rodzicom

Contents

1

Introduction and Theory of Semiconductor Heteronanocrystals

1.1 Introduction

The idea of manipulating and controlling matter at the nanoscale was first proposed in 1959 by Richard P. Feyman. In his famous lecture "There`s plenty of room at the bottom" he said: "The principles of physics, as far as I can see, do not speak against the possibility of maneuvering things atom by atom. It is not an attempt to violate any laws; it is something, in principle, that can be done; but in practice, it has not been done because we are too big".[1] A few decades later the needs of miniaturization led scientists to the discovery of *e.g.,* the scanning tunneling microscope and semiconductor nanoparticles, which are nowadays of increasing interest. The reduction of the size of semiconductor crystals to the nanoscale regime leads to spatial confinement of the charge carriers, influencing the material properties. More precisely, the confinement of the electron and hole in a small volume results in new optical and electronic properties, which can be tuned by changing the nanoparticle size and shape. This phenomenon is commonly refered as the quantum confinement effect, and will be explained in detail below. Nowadays nanoparticle research has developed into one of the major fields in modern science. The size-dependent electronic structure and related optical properties of semiconductor nanoparticles have received much attention. The development of wet chemical synthesis methods in which the size and shape of the nanocrystals (NC) can be controlled was a breakthrough in this field.[2-4] Moreover, the discovery of colloidal nanocrystals (nanocrystals dispersed evenly throughout another substance) was crucial and impacts on a wide variety of applications, *e.g.,* solar cells, LED technology, nanocrystal lasers or biological labels.

A new and very promising approach is to extend the properties of nanoparticles by combining two (or more) semiconductor materials in one single heterostructured colloidal nanoparticle (*i.e.,* a heteronanocrystal HNC). The size and the shape of each component of the heteronanocrystal and the way in which they are connected are of pivotal importance and leads to remarkable and unique properties.

This thesis focuses on the structural characterization and opto-electronic properties of PbSe/CdSe heteronanocrystals. In the next section of this chapter a general introduction to semiconductor nanocrystal quantum dots (QDs) will be given. Sections 1.3 and 1.4 deal with the electronic structure and optical properties of quantum dots. Heteronanocrystals and their electronic structure are addressed in section 1.5. Section 1.6 presents an introduction to scanning tunneling microscopy and spectroscopy. Finally, the outline of this thesis is presented.

1.2 Semiconductor Nanocrystal Quantum Dots

The spatial confinement of the charge carriers in a semiconductor nanocrystal can occur in different directions depending on the dimensions and shape of the nanocrystal and the extension of the electron and hole wave functions. Therefore, different architectures are possible for semiconductor nanostructures: *quantum well* (one dimensional confinement), *quantum wire* (two dimensional confinement) and finally *quantum dots* (three dimensional confinement). Semiconductor nanocrystal quantum dots (QDs) consist of only few hundred to a few thousand atoms and have sizes in the 1-100 nm range. As a consequence of the confinement of electron and hole in a such a small volume the kinetic energy of the charge carriers rises above their bulk value and atomic-like discrete energy levels are formed. Therefore, semiconductor QDs bridge the gap between bulk solid state and the single atom, showing a mixture of atomic-like and bulk-like properties. The energy levels and unique properties of QDs can be explained by two different approaches. The first one, called "top-down" approach, starts at the bulk semiconductor level and considers the effect of the size reduction to the nanoscale on the energy levels of the semiconductor nanocrystal. The second one is called the "bottom-up" approach and treats a QD as a very large molecule or cluster, in which energy levels rise from the atomic orbitals. The top-down and bottom-up approaches will be described in sections 1.3.2 and 1.3.3, respectively. In general, to explain the quantum confinement effect in QDs is convenient to start looking at the issue from the bulk semiconductor perspective.

The characteristic feature of a bulk semiconductor is the energy gap between conduction and valence bands, which is determined by the chemical composition and crystal structure of the material. An electron in a bulk semiconductor can be excited from the valence to the conduction band by an appropriate photon absorption. This creates a hole in the valence band. Due to their opposite charges the electron and hole form a pair bound by a Coulomb interaction that moves as a single entity called an exciton. The exciton wave function is extended over a large region (several lattice spacings), *i.e.,* the exciton Bohr radius is large, since the effective masses of charge carriers are small and the dielectric constant is high.[5, 6] In the case of quantum dots, the size reduction to a few nanometers creates a situation where the crystal dimensions becomes comparable to the exciton spatial extension. In this size range the properties of semiconductor nanocrystals start to differ from those of bulk semiconductors. The charge carriers assume higher kinetic energies leading to an increasing energy of the electron and hole levels. As a result, the HOMO (highest occupied molecular orbital)-LUMO (lowest unoccupied molecular orbital) gap and the separation between the electron (and hole) levels increases remarkably with decreasing nanocrystal size. This is commonly called quantum confinement effect and results directly from Heisenberg`s uncertainty principle.[7-9]

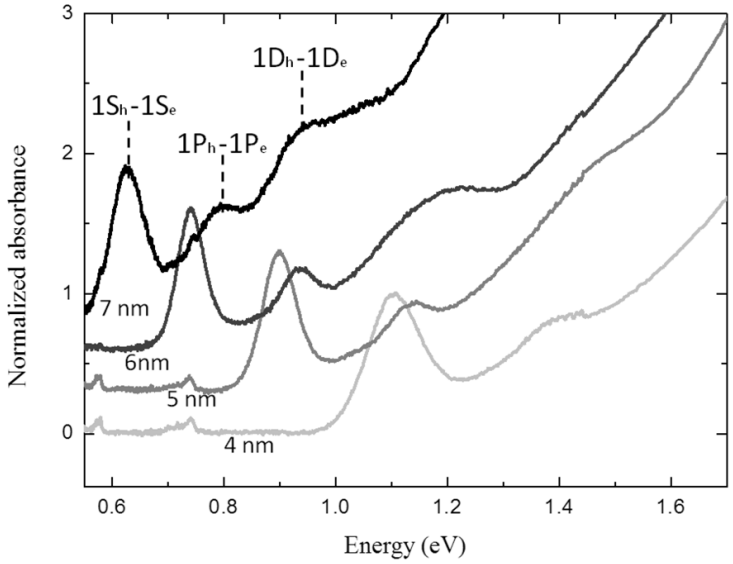

Fig. 1.1 Absorption spectra of PbSe QDs with different sizes, showing the peaks shifting to higher energy with decreasing of QDs size. The indication for first three transitions are presented in upper spectrum (with 7nm diameter QD).

Decreasing the particle size, causes the energy structure to become discrete with atomic-like states. Therefore, QDs are often called "artificial atoms".[10] Similar to atoms and molecules, the well separated energy states of QDs are labeled 1S, 1P, 1D and so on, and the energy values depend on the quantum dots diameter. By changing the nanocrystal size (and shape), its energy bandgap can be tuned, since smaller nanocrystals have bigger energy gaps. This can be seen in Fig. 1.1, which shows the absorption spectra of PbSe QDs, where absorption peaks reflect the allowed optical transitions. The optical transitions are denoted as $1S_h - 1S_e$ for first transition, $1P_h - 1P_e$ for second transition, and so on. The nature of optical transitions are determinate by selection rules (see section 1.4). The quantum confinement effect strongly influences the optical properties of QDs. The second significant effect of quantum confinement, *i.e.,* the appearance of discrete atomic-like energy levels can be clearly observed by scanning tunneling spectroscopy. Figure 1.2. shows a tunneling spectrum of a PbSe QD of 5.5 nm in diameter, where discrete levels denoted as $1S_h, 1S_e$ and so on, for hole and electron states respectively.[11] Scanning tunneling spectroscopy will be explained in more detail in section 1.6.

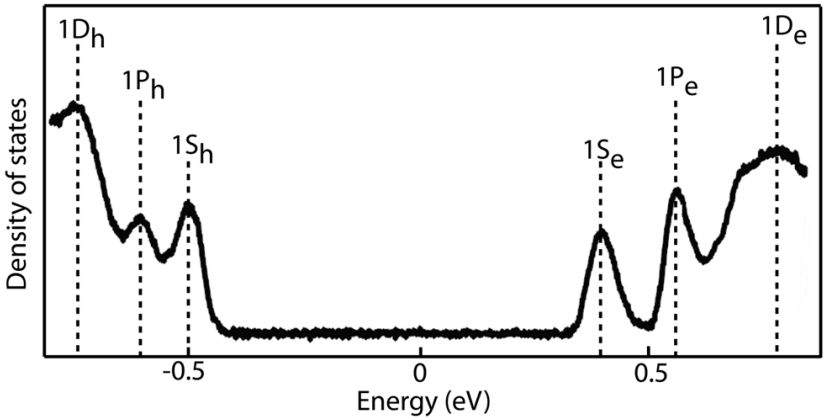

Fig. 1.2 Tunneling spectrum of PbSe QD with 5.5 nm diameter showing discrete hole and electron states. [11]

There are several methods of making nanocrystals. The first nanocrystals were fabricated in a solid host. For instance, already in the 1960s glasses doped with II-VI semiconductor nanocrystals (mostly CdS_xSe_{1-x}) were studied where by diffusion-controlled growth of nanometer sized crystallites in a glass matrix the first color cut-off filters and photochromic glasses were fabricated. Much later, the commercial photochromic glasses consisting of I-VII materials (*e.g.,* CuCl, CuBr, AgBr) were developed.[12] Different ways of NC preparation like molecular beam epitaxy (MBE)[13] or chemical vapor deposition (CVD)[14] have been developed. Colloidal chemistry methods[2, 15] provide an alternative preparation route for nanocrystal growth, and have developed dramatically since 1981, yielding an enormous variety of colloidal NCs with different size, shape, composition, crystal structure and properties.[16-18]

This PhD thesis is focused on colloidal nanocrystals and heteronanocrystals synthesized by colloidal-chemical methods. The colloidal nanoparticles possess an organic outer layer made of surfactant molecules (also called ligands or capping molecules). They contain a head group that binds to the NC surface and a hydrocarbon tail that interacts with the surrounding medium and provides repulsion between the NCs, therefore prevening them from agglomeration. The capping molecules also passivate the dangling bonds at the semiconductor surface.[19] By being so small the nanoparticles possess large surface to volume ratio, and are very sensitive to surface defects. Surface and defects states can have undesired influence on the optical properties (photoluminescence quantum yield), *i.e.,* by

trapping the electron or hole and thereby inducing non-radiative recombination. There is a big variety of molecules that can be used as a capping layer: *e.g.,* alkylamines, fatty acids or alkythiols. Depending on the shape, length and binding strength of head group to selective NC facets they determine the growth and the quality of the NCs. In general, ligands that bind strongly to the NC surface and have a linear structure lead to a higher coverage and passivate the NC surface more efficiently than bulky ligands.[17] In this thesis, the PbSe QDs and PbSe/CdSe core/shell QDs are capped by linear oleic acid (OA) molecules, which belong to fatty acid group and bind strongly to the NC surface. Some capping ligands (*e.g.*, thiols and methylviologen) possess interesting charge scavenging properties, and can be used to probe the carrier localization regime in heteronanocrystals (see chapter 2 of this thesis).

1.3 Electronic Structure of Semiconductor Quantum Dots

1.3.1 Electrons in Periodic Structures

To understand the changes of semiconductor properties due to quantum confinement of the charge carriers it is essential to first explain bulk semiconductor properties. One of the early explanations of solid state properties was given by Sommerfeld, who assumed the bulk crystal to be like a simple box filled by a free-electron-gas. According to this theory the potential energy of electrons over the whole crystal is constant and the local changes of potential due to interaction of atomic cores with electrons can be neglected (Fig. 1.3A). Inside the crystal box the electrons are treated independently but in accordance with the principles of quantum mechanics and can hence be described by the Schrödinger equation:

$$-\frac{\hbar^2}{2m_e}\nabla^2\Psi(\mathbf{r}) + \mathrm{U}(\mathbf{r})\Psi(\mathbf{r}) = \mathrm{E}\Psi(\mathbf{r}) \qquad (1.1)$$

where Ψ and E are the wave function of the electron and its energy, respectively. m_e is the free electron mass, $\hbar$ is reduced Planck`s constant, $\boldsymbol{r}$ is the position vector *(x,y,z)* and U is the potential.

Free electrons possess wave properties with wave vector **k** and wavelength λ related to their momentum **p** according to the relation discovered by de Broglie:[12] $\mathbf{p} = \hbar\mathbf{k}$, $\lambda = \frac{\mathrm{h}}{\mathrm{p}}$. Their kinetic energy is thus given by $E = \frac{p^2}{2m} = \frac{\hbar^2 k^2}{2m}$

When the free electron is placed into a quantum box with infinite walls, *i.e.,* the potential outside the box is infinite, the wave function Ψ outside the box is zero. The electrons

cannot leave the crystal thus the probability of finding electrons outside the box is zero. Considering that the potential energy U inside the box is zero the solution of Schrodinger equation is:

$$\Psi_{\mathbf{k}}(\mathbf{r}) = \frac{1}{\sqrt{\mathrm{V}}} \mathrm{e}^{\mathrm{i}\mathbf{k}\cdot\mathbf{r}} \tag{1.2}$$

where V is the crystal volume. Substitution of (1.2) into (1.1) gives the energy eigenvalues as a function of the wave vector **k**:

$$\mathrm{E}(\mathbf{k}) = \frac{\hbar^2 k^2}{2\mathrm{m}} \tag{1.3}$$

This equation (which also follows from the relation of de Broglie) describes the dispersion relation for free electrons and is graphically illustrated at Fig 1.4A. Classically, the electron has a quasi-continuum of energy levels, indicating that *k* can take any value.

We consider now electrons confined in a box with dimensions L_x, L_y, L_z surrounded by an infinite potential energy barrier. In the x – direction, the wavefunction value $\Psi_{k_x}(x)$ at point x=0 and x=L must be zero. Applying these boundary conditions, the wavefunction for one-dimensional particle-in-a-box becomes:

$$\Psi_{k_x}(x) = \sqrt{\frac{2}{\mathrm{L}}} sin(k_x x) \tag{1.4}$$

Which is the standing wave with wavelength $\lambda_e = \frac{2\pi}{k}$. The possible values of k_x satisfying equation (1.4) are:

$$k_x = \frac{n_x \pi}{L_x}, \qquad n_x = 1,2,3, \ldots \tag{1.5}$$

The first three wavefunctions for an electron in the box with quantum numbers n=1,2, 3 are graphically presented at Fig.1.3B.

In the case of a tetragonal box, the complete three-dimensional wavefunction is a product of three one-dimensional wavefunctions and can be written as:

$$\Psi_{\mathbf{k}}(\mathbf{r}) = \sqrt{\frac{8}{\mathrm{L}^3}} sin(k_x x)\, sin(k_y y)\, sin(k_z z) \tag{1.6}$$

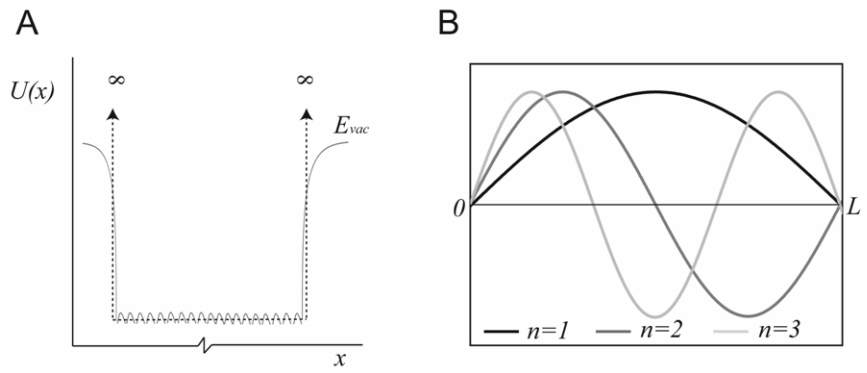

Fig. 1.3 (A) Schematic representation of the potential energy of electron for the Sommerfeld model in one-dimensional infinite potential well (dashed line) and for realistic crystal model assuming an electron in periodic potential due to atomic cores (solid grey line). (B) The wavefunction for electron in the quantum box model for n=1,2 and 3.

In contrast to the free electron case, k cannot have any value but only these specified by quantum number n. Therefore the energy is quantized and can be expressed by:

$$E = \frac{\hbar^2 \boldsymbol{k^2}}{2m} = \frac{\hbar^2}{2m}\left(k_x^2 + k_y^2 + k_z^2\right) = \frac{\pi^2\hbar^2}{2m}\left(\frac{n_x^2}{L_x^2} + \frac{n_y^2}{L_y^2} + \frac{n_z^2}{L_z^2}\right) \tag{1.7}$$

So far the Sommerfeld theory of crystal was based on the assumption that the potential over the whole crystal is constant. However, in reality, the potential varies periodically in space according to the distribution of ions in the structure, causing a significant change in dispersion relation for electrons. In perfect crystal the ions are arranged in a regular periodic array, thus the electron can be found in a potential U($\mathbf{r}$) with the periodicity of the underlying Bravais lattice:

$$\mathrm{U}(\mathbf{r} + \mathbf{R}) = \mathrm{U}(\mathbf{r}) \tag{1.8}$$

for all Bravais lattice vector $\mathbf{R} = \mathrm{n}_1\mathbf{a_1} + \mathrm{n}_2\mathbf{a_2} + \mathrm{n}_3\mathbf{a_3}$

Taking into account the periodic potential, the Schrodinger equation takes the form:

$$-\frac{\hbar^2}{2m_e}\nabla^2\Psi(\mathbf{r} + \mathbf{R}) + \mathrm{U}(\mathbf{r})\Psi(\mathbf{r} + \mathbf{R}) = \mathrm{E}\Psi(\mathbf{r} + \mathbf{R}) \tag{1.9}$$

Independent electrons that obey a one-electron Schrodinger equation with a periodic potential are called Bloch electrons.

The eigenstates Ψ of the one-electron Hamiltonian $\mathrm{H} = -\hbar^2\nabla^2/2\mathrm{m} + \mathrm{U}(\mathbf{r})$, where $\mathrm{U}(\mathbf{r}+\mathbf{R}) = \mathrm{U}(\mathbf{r})$ can be presented in the form of a plane wave ($e^{i\boldsymbol{k}\cdot\boldsymbol{r}}$) times a function with periodicity of the Bravais lattice $u_{\boldsymbol{k}}(\boldsymbol{r})$:

$$\Psi_{\mathbf{k}}(\mathbf{r}) = e^{i\boldsymbol{k}\cdot\boldsymbol{r}}u_{\boldsymbol{k}}(\boldsymbol{r}) \tag{1.10}$$

where $u_{\boldsymbol{k}}(\boldsymbol{r}+\boldsymbol{R}) = u_{\boldsymbol{k}}(\boldsymbol{r})$**.** Eq. (1.10) is called a Bloch function and its translation over the vector $\boldsymbol{R}$ gives:

$$\Psi_{\mathbf{k}}(\mathbf{r}+\mathbf{R}) = e^{i\boldsymbol{k}\cdot\boldsymbol{r}}u_{\boldsymbol{k}}(\boldsymbol{r}) = \Psi_{\mathbf{k}}(\mathbf{r}) \tag{1.11}$$

The presence of the periodic potential leads to important changes in the dispersion relation of electrons. Electrons traveling in a one-dimensional lattice with a wavelength much longer then lattice constant *a* do not feel the influence of periodic potential and their energy is similar to that of free electrons. However, electrons with short wavelength feel the periodic potential due to presence of positive ion cores (Fig.1.4B). When the wavelength of electrons is similar to *2a* the electrons will be reflected by potential, according the Bragg conditions $k = n\pi/a$. The first reflection occur at $k = \pm\pi/a$. At this value of k the electron wavefunction consist of equal parts of waves traveling to the right ($k = \pi/a$) and to the left ($k = -\pi/a$). The linear combination of these plane waves creates two standing waves $\Psi(+)$ and $\Psi(-)$, which pile up electrons at different regions. The $\Psi(+)$ concentrate the electron probability at the positive ions, lowering the potential energy; while the $\Psi(-)$ concentrate the probability in between the ions increasing the potential energy (Fig 1.4B). The differences in potential energy for both standing waves create discontinuities in the dispersion relation of electrons at $k = n\pi/a$ which is called the band gap. The region in k space between π/a and $-\pi/a$ is named *first Brillouin zone (BZ)*. The free electron dispersion relation is a good approximation for most electrons in the band, however it does fail for electrons at the edges of Brillouin zones. The dispersion relation for electrons in periodic potential in one-dimensional lattice is presented in the Figure 1.4.C.

In Figure 1.4C it can be also seen that each parabola differs in wave number by $2\pi/a$ and this is a result of periodicity of $u_{\boldsymbol{k}}(x)$ along with the periodicity of phase coefficient e^{ikx} (with respect to *kx* with period 2π). Therefore the wavenumbers differing in integer number $2\pi/a$, that is $k_1 - k_2 = (2\pi/a)n$ (for $n = \pm1, \pm2, \pm3, ...$) are equivalent, what is a direct consequence of the translational symmetry of space.

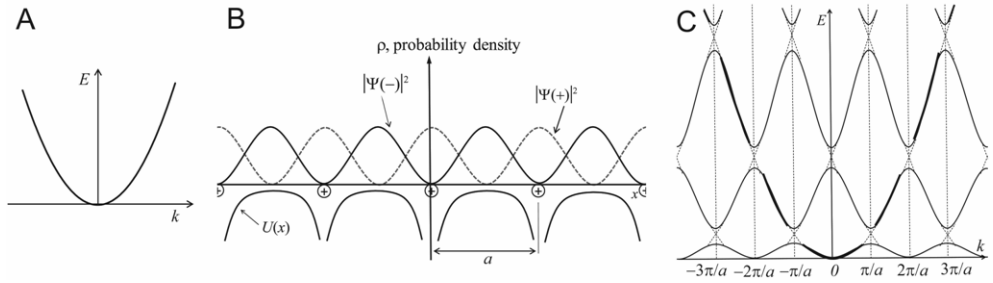

Fig. 1.4 (A) Dispersion relation for free electron model. (B) Variation of potential energy *U(x)* of an electron in one dimensional lattice; Distribution of probability density ρ, for $|\Psi(+)|^2 \propto cos^2 \pi x/a$ (dashed line) and $|\Psi(-)|^2 \propto sin^2 \pi x/a$ (solid line). The wavefunction $\Psi(+)$ concentrate electrons on the cores of positive ions, lowering therefore the potential energy, while wavefunction $\Psi(-)$ concentrate the electrons in the region between the ions, rising the potential energy. (C) Dispersion relation for electrons in periodic potential showing the energy gaps at the edges of Brillouin zones where $k = \pm n\pi/a$.

In general, electron states in the first BZ are characterized by points and lines which are labeled by Latin and Greek capitals. For the first BZ of a hexagonal close-packed (HCP) lattice (Fig. 1.5A) the fundamental band gap is located in Γ point, where $k_x = k_y = k_z = 0$. It is important to mention that there is only one Γ point for this structure. The situation looks different for face centered cubic (FCC) lattice (*e.g.,* the rock salt structure of PbSe), for which first BZ has shape of truncated octahedron (Fig. 1.5B). Here the fundamental band gap is located at L point where $k_x = k_y = k_z = \pi/a$. There are eight equivalent L points at the egdes of the first BZ. Each L-point is shared with a neighboring BZ, therefore there are 4 L points. The fundamental bandgap for PbSe is therefore 4-fold degenerated, 8 if spin degeneracy is included, for both conduction electron and valence hole energy level. That leads to 64 degenerated lowest exciton states. This degeneracy can be partially lifted by several effects *viz*., intraband coupling, electron-hole exchange and coupling between different L points (inter-valley coupling). These effects depend strongly on the PbSe QD size and can be observed for PbSe nanoparticles with diameter smaller than 4 nm, where quantum confinement effect is very strong (see Chapter 3 of this thesis). For bulk PbSe these effects have no influence on band structure (Fig. 1.5C). The band structure representation can be seen as a short version of the 3D dispersion relation (*i.e.,* only a few directions in reciprocal space and only the most relevant points in the BZ are represented).

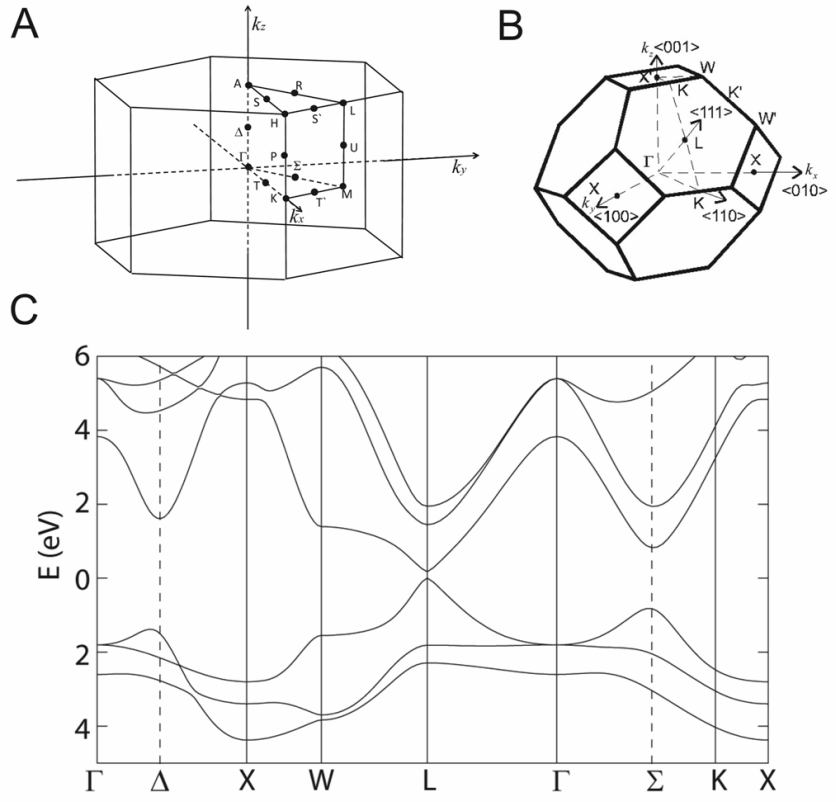

Fig. 1.5 First Brillouin Zone for a hexagonal close-packed HCP (A) and face-centered cubic (B) crystal lattice. (C) Band structure for bulk PbSe with fundamental bandgap located at L-point.[20]

The dispersion relation of electrons in periodic potential is also related to particles effective mas m^*:

$$\frac{1}{m^*} = \frac{1}{\hbar^2}\frac{d^2E}{dk^2} \tag{1.12}$$

It can be seen that the effective mass is determined by the curvature of the band, and is therefore valid only for zone boundaries, which are regions with unusually high curvature. The band structure has a different curvature in different directions, therefore there are different effective masses for different crystallographic directions and different extrema.

1.3.2 Quantum Confinement: Top-Down Approach

The "top-down" approach is one of the methods to explain the energy levels of QDs. So far only the infinite semiconductor band structure was explained. This section will show what happens when the semiconductor crystal becomes smaller and smaller, finally reaching the nanoscale size range. It can be explained by taking well-known electron wavefunction of bulk semiconductor and confining it to finite volume of nanocrystal. Assuming the nanocrystal to be spherical, the energy levels can be obtained by using a particle in "spherical quantum box model". The new wavefunction consists of a Bloch wavefunction describing bulk semiconductor properties in a periodic potential, and the envelope function that describes the confinement of charge carriers in small QD volume. The total wavefunction can therefore be written as:

$$\Psi_{tot}(\boldsymbol{r}) = u_k(\boldsymbol{r})\phi_{env}(\boldsymbol{r}) \tag{1.13}$$

The envelope wavefunction is the solution of Schrodinger equation for particles in spherical quantum box. Due to the fact that the box is no longer cubic the eigenfunction cannot be a sinusoidal function, but is a product of spherical harmonics $\Upsilon_{lm}(\vartheta, \varphi)$ and radial Bessel function $R(\boldsymbol{r})$:

$$\phi_{env}(\vartheta, \varphi, \boldsymbol{r}) = \Upsilon_{lm}(\vartheta, \varphi)R(\boldsymbol{r}) \tag{1.14}$$

Substitution of the above function into the Schrodinger equation (with spherical coordinates) results in formula for discrete energy levels of particles in the spherical potential well with diameter *D*:[21]

$$E_{nl}^{conf}(D) = \frac{2\hbar^2\chi_{nl}^2}{m^*D^2} \tag{1.15}$$

where χ_{nl} are roots of spherical Bessel functions. In contrast to energy levels of particles in cubic box which depend on quantum number (n_x, n_y, n_z), the energy levels in spherical well depend on quantum number (*n,l*), where *l=0,1,2,3* are written as *S, P, D, F* respectively. The degeneracy of energy levels is given by *2l+1* in analogy to atoms.

The full expression of the quantum dot energy bandgap is a combination of semiconductor bulk bandgap (E_g^0) and confinement energy (E_{nl}^{conf}) for electrons and holes, and is defined as:[22]

$$E_g^{tot}(D) = E_g^0 + E_{nl}^{conf}(D) = E_g^0 + \frac{2\hbar^2\chi_{nl}^2}{m_e^*D^2} + \frac{2\hbar^2\chi_{nl}^2}{m_h^*D^2} \tag{1.16}$$

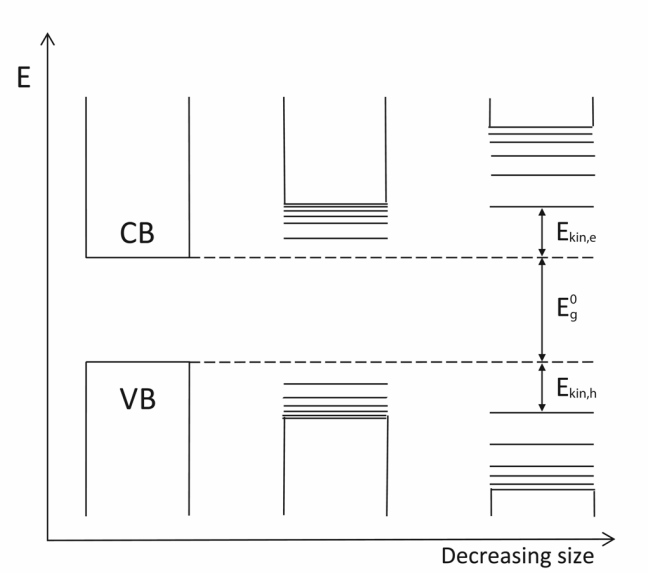

Fig. 1.6 Schematic representation of top-down approach of quantum confinement effect, showing the changes of energy bandgap with decreasing semiconductor size.

The above equation shows that confinement of charge carriers in small nanocrystal volume increases their kinetic energy by E_{nl}^{conf}. The energy bandgap thus increases with decreasing of nanocrystal size with D^{-2}. The separation between band-edge energy levels increases as well with the reduction of the semiconductor nanocrystal size (Fig. 1.6). This is visible in the absorption spectrum of nanoparticles, where peaks related to specific energy levels can be easily identified (see section 1.4 and Fig. 1.1).

Equation (1.16) is based on non-interacting electrons and holes. However, in reality, the electron and the hole interact with each other via Coulumb attractions. The interacting electron and hole form a quasiparticle corresponding to hydrogen-like bound state, called an exciton. In analogy to the hydrogen atom the exciton is also characterized by a Bohr radius a_B.The energy of the first optical transition becomes then:

$$E_{nml} = E_g^0 + \frac{2\hbar^2\chi_{ml}^2}{m_e^* D^2} + \frac{2\hbar^2\chi_{ml}^2}{m_h^* D^2} - \frac{e^2}{2n^2\varepsilon a_B}, \qquad n = 1,2,3,\ldots, \tag{1.17}$$

(where Ry is the exciton Rydberg energy $Ry = e^2/2\varepsilon a_B$), and ε is the dielectric constant. The exciton energy in a spherical quantum dot is characterized by *n*-principal quantum number and also by *m, l* - magnetic and orbital quantum numbers which are connected with center-of-mass motion.

The exciton Bohr radius and size of semiconductor nanocrystal influence strongly the properties of nanocrystal. Depending on the relation between the QD radius (*r*) and (a_B), the quantum confinement can be divided in two ranges, named 'weak and strong confinement regime'. The weak confinement regime is observed for relatively big QDs, in which the radius correspond to $r > a_B$ (in practice up to $r \cong 4a_B$). A small exciton Bohr radius results in large exciton Rydberg energy *Ry* for weak confinement regime and this is characteristic for wide-band semiconductors of I-III compounds. Moreover, the relatively large nanocrystal radius (*r*) leads to an insignificantly small confinement energy. Therefore, the large nanocrystals with radius $r \gg a_B$ exhibit in principle the same features as bulk semiconductor and their energy bang gap is equal to E_g^0. Decreasing the nanocrystal size results in shifting its absorption energy to the higher values (what is called a blue shift). The absolute value of the total shift is however smaller than the value of exciton Rydberg energy. This is a characteristic property of nanocrystals in weak confinement regime.

The strong confinement regime is characteristic for nanocrystals with radius $r \leq a_B$. In this case, the electron and the hole are not bound as in a hydrogen-like exciton, since the confinement energy of electrons and holes is larger than the Coulomb energy. Assuming uncorrelated motion of the electron and the hole, the Coulomb interaction can be ignored and the energy bandgap can be expressed by equation (1.16).

The vanishing of the last term in equation (1.17) can be observed for instance in PbSe QDs, which have a large dielectric constant ε. This facilitates the creation of free charges, making PbSe QDs (with short ligands) a promising material as active medium in solar cells.[23, 24] In general, highly mobile charges are difficult to achieve in QDs, and the elementary excitation in quantum dots is classified as an exciton, rather than free electron and hole, even if the relevant state does not obey the hydrogen-like model.

1.3.3 Quantum Confinement: Bottom-Up Approach

The previous section explained the electronic structure of nanocrystal QDs by showing the evolution with decreasing size, starting from the bulk semiconductor to a nanocrystal. Another method to explain the QD properties is based on a "bottom-up" approach, in which

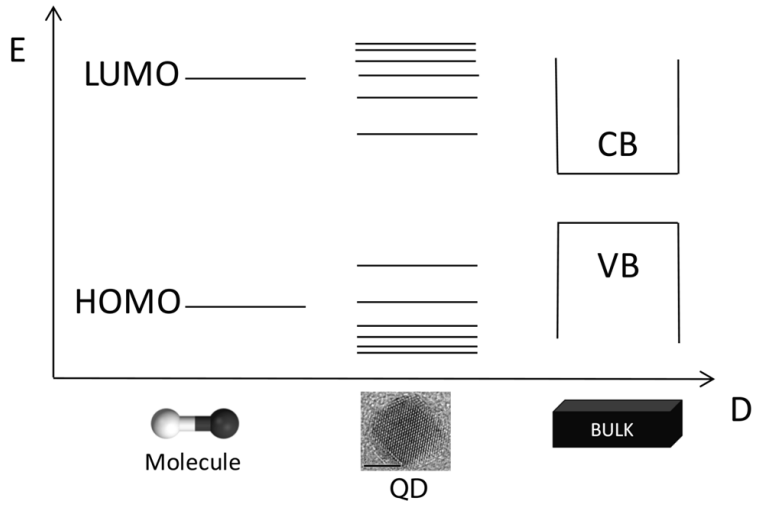

Fig. 1.7 The semiconductor size dependent evolution of energy levels illustrating bottom-up approach of quantum confinement effect.

the size is increased from atom to bulk material. In this approach the QD is assumed to be a large molecule (or cluster). In molecules the electrons are described by orbitals in analogy to electrons in atoms. The molecular orbitals (MO) are constructed by using a linear combination of atomic orbitals (LCAO). Considering for instance a molecule made of two atoms, the linear combination of atomic orbitals results in molecular orbital with lower energy (bonding orbital) and a higher energy (anti-bonding) orbital. The electrons start filling the molecular orbitals from the lowest energy one. Figure 1.7 shows the evolution from a two-atom molecule to a bulk semiconductor, illustrating the concept of bottom-up approach to the energy level structure. The number of MO increases proportionally with the number of atoms involved, and the energy bandgap between HOMO and LUMO becomes smaller. Further increase of the size of the semiconductor finally results in bulk semiconductor, where the energy spacing between the MO`s becomes so small that it can no longer be distinguished, forming quasi-continuous (valence and conduction) bands.

An example of the LCAO method representing MO for a one-dimensional PbSe crystal consisting of 8 Pb and 8 Se atoms is shown in Fig. 1.8. The high atomic number of Pb cations causes that relativistic effects contribute strongly to the electronic structure of PbSe QDs. This effect lowers the Pb 6s orbital energy and pulls it down from conduction to valence band below Se 4s and 4p levels. Therefore the conduction band consists of

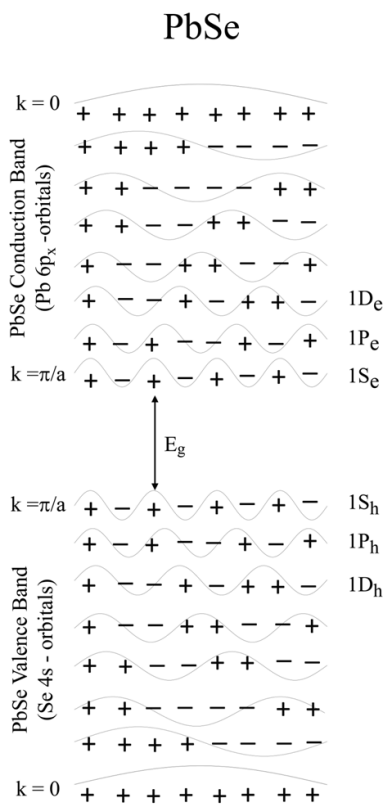

Fig. 1.8 Schematic representation of conduction and valence band levels in PbSe QDs. The orbitals combined in valence band show s-like symmetry, while conduction band orbitals combination results in p-like symmetry. The sinusoidal functions illustrate the phase of atomic orbitals. Redrawn from.[22]

remaining p orbitals and the top of the valence band is build from Se 4s orbitals.[25] In reality the valence band of PbSe QDs is more complicated and contain filled hybridized Se $4sp^3$ orbitals mixed with filled Pb 6s orbitals.[26] Both the valence band maximum and conduction band minimum are located in four-degenerated L-points in the Brillouin zone where $k = \pi/a$.

The solid grey lines in Fig.1.8 represent the sinus functions describing the phase of the atomic orbitals. Adding the wavefunctions with the same phases (+ and +) or (- and -) or with opposite phases (+ and -) gives an idea of molecular orbitals creation.

The top-down and bottom-up approaches are two different methods to explain the dependence of the energy levels of QDs. They predict slightly different size dependent energy band gaps. Bottom-up approach (based on atomistic calculations) predicts that hole states are much more dense than electron states, in contrast to the results obtained by the top-down approach. The 4×4 L-centered top-down approach for PbSe ignores intervalley coupling and limits valence-conduction coupling to be a single (double degenerated) band for each edge and neglects the L-valley anisotropy effect.[25, 27] Moreover, the overestimation of confinement in 4×4 L point calculations is apparent from the fact that its confined levels scale with the QD size, *D*, as $1/D^2$, while bottom-up calculations with finite barriers show a much weaker confinement with $1/D^n$, $(1 < n < 2)$ scaling.[25, 28] Koole *et al.* has presented experimental data showing that $E \sim 1/D^{1.5}$ for PbSe QDs.[29]

The bottom-up approach is a powerful method to explain QDs properties in a quantitative way, however it is limited only for small cluster, due to computational limits.

1.4 Optical Properties of Semiconductor Quantum Dots

The quantum confinement effect explained in previous section strongly influences the optical properties of QDs, as can be seen in their absorption spectra (Fig. 1.1). Absorption peaks reflect allowed optical transitions, which are denoted as $1S_h - 1S_e$ for first transition, $1P_h - 1P_e$ for second transition, and so on. The nature of optical transitions are determined by selection rules. In general, optical transitions can be divided in two groups: intraband and interband transitions. Intraband transitions occur between states originating from the same band (*i.e.,* transition of electron (hole) within a conduction (valence) band), while interband transitions are those taking place between different (valence-conduction) bands, leading to electron-hole pair creation. In both cases the transition from one state to another (*e.g.,* from *a* state to the *b* state) is allowed only if the resulting mixed state possess a dipole moment. From quantum mechanical point of view this means that the initial and final states must have different parity. This gives the selection rule: $\Delta l = \pm 1$.

The probability P_{ab} of optical transitions from the state *a* to the state *b* is proportional to the square of the matrix element of the momentum operator $\mathbf{p} = -\mathrm{i}\hbar\boldsymbol{\nabla}$ between both states:[30]

$$P_{ab} \propto |\langle \Psi_b | \mathbf{p} | \Psi_a \rangle|^2 \tag{1.18}$$

Bearing in mind that the wavefunction of initial *a* state has following form

$$\Psi_a(\boldsymbol{r}) = u_{k_a}(\boldsymbol{r}) \phi_{env_a}(\boldsymbol{r}) \tag{1.19}$$

where $u_{k_a}(\boldsymbol{r})$ is periodic part of the Bloch function (atomic function) and $\phi_{env_a}(\boldsymbol{r})$ is the envelope function, the matrix element can be written as[31]

$$\langle \Psi_b|\mathbf{p}|\Psi_a\rangle = \langle \phi_{env_b}|\phi_{env_a}\rangle\langle u_{k_b}|\mathbf{p}|u_{k_a}\rangle + \langle u_{k_b}|u_{k_a}\rangle\langle \phi_{env_b}|\mathbf{p}|\phi_{env_a}\rangle \quad (1.20)$$

The first term describes interband transitions, which occur for different atomic function (*e.g.*, from s-like valence Se orbitals to p-like conduction Pb orbital in PbSe QD, see Fig. 1.8) and the same envelope functions (*e.g.*, $1S_h$ to $1S_e$ state, Fig. 1.8 and 1.1). The same envelope functions ($\phi_{env_a} = \phi_{env_b}$) cause that $\langle \phi_{env_b}|\mathbf{p}|\phi_{env_a}\rangle = 0$, and (the overlap integral) $\langle \phi_{env_b}|\phi_{env_a}\rangle = 1$, therefore the matrix element for interband transitions reduces to:

$$\langle \Psi_b|\mathbf{p}|\Psi_a\rangle_{interband} = \langle u_{k_b}|\mathbf{p}|u_{k_a}\rangle \quad (1.21)$$

Thus the transitions are provided by parity changes in atomic functions ($\Delta l = \pm 1$) (*e.g.*, s to p orbital). The parity and orbital angular momentum for envelope functions are the same ($\Delta l = 0$) for interband transitions. Therefore, the allowed transitions are: $1S_h - 1S_e$, $1P_h - 1P_e$ and $1D_h - 1D_e$ and so on (see Fig. 1.1), while, for example, $1S_h - 1P_e$ interband transition is forbidden.

In contrast, the intraband transitions (*e.g.,* Se 4s to 4s orbitals within valence band of PbSe QDs, Fig. 1.8) occurs between the same atomic functions. Mixing of s-orbitals does not lead to dipole creation (*i.e.*, $\Delta l = 0$). Therefore, the dipole has to arise from changes of parity in the envelope functions. From equation (1.20) one can observe that equal atomic functions $u_{k_a} = u_{k_b}$, leads to $\langle u_{k_b}|\mathbf{p}|u_{k_a}\rangle = 0$ and $\langle u_{k_b}|u_{k_a}\rangle = 1$, therefore intraband transitions are described by:

$$\langle \Psi_b|\mathbf{p}|\Psi_a\rangle_{intraband} = \langle \phi_{env_b}|\mathbf{p}|\phi_{env_a}\rangle \quad (1.22)$$

Parity selection rules and conservation of angular momentum ($\Delta l = \pm 1$) apply to envelope functions, therefore, within *e.g.*, the conduction band, transitions like $1S_h - 1P_h$, $1P_h - 1D_h$ and so on are allowed. The intraband transitions in nanocrystals usually occurs in the infrared spectral range and are particulary interesting because they involve only one type of carriers, which allows to study separately the dynamics of electrons and holes.[30, 32]

Radiative recombination is the reverse process of absorption, therefore the selection rules for absorption apply also for radiative emission. As a consequence, the matrix element of momentum which is directly related to dipole matrix element $\mathbf{D}_{ba}$ presented below gives us information about absorption and emission transition rate. [33]

$$\mathbf{D}_{ba} = \frac{ie}{m_0 \omega_{ba}} \langle \Psi_b | \mathbf{p} | \Psi_a \rangle \,, \tag{1.23}$$

Where, $e-$ is elementary charge, $m_0 -$ elementary charge mass and $\omega_{ba} -$ angular frequency of transition $a \rightarrow b$.

The absorption transition rate between ground state *a* and excited state *b* is given by:

$$\Gamma_{ba} = \frac{\pi I(\omega_{ba}) F^2 n}{3\hbar^2 c \varepsilon_0} |\mathbf{D}_{ba}|^2 \tag{1.24}$$

Where $I(\omega_{ba})$ is intensity of radiation of angular frequency ω_{ba}, *F* is the local field factor, ε_0 is permittivity of vacuum and *n* is the refractive index. The strength of optical coupling between states *a* and *b* is very often described by a quantity without dimension named oscillator strength[30]:

$$f_{ba} = \frac{2m_0}{\hbar} \omega_{ba} |\mathbf{D}_{ba}|^2 \tag{1.25}$$

The absorption transition rate as well as the oscillator strength depend strongly on the magnitude of the transition dipole moment.

The rate of spontaneous emission has the following form, deduced from Fermi`s Golden Rule[5, 30]:

$$\Gamma_{rad} = \frac{\omega_{ba}^3 F^2 n}{3\pi c^3 \hbar \varepsilon_0} |\mathbf{D}_{ba}|^2 \tag{1.26}$$

The emission transition rate is not only dependent on the magnitude of the transition dipole moment, but also on the density of optical modes, which increases with frequency ω^2.

For quantum dots the transition rate for absorption[34] and emission[35] for lowest exciton state $1S_h - 1S_e$ can be calculated according to (1.23) if the Kane interband matrix element $P = |\langle 1S_h | \mathbf{p} | 1S_e \rangle|$ is included in dipole matrix element $\mathbf{D}_{ba} = \frac{ie}{m_0 \omega_{ba}} |\langle 1S_h | \mathbf{p} | 1S_e \rangle|$.

The rate of photon emission provides important information about the lifetime of the excitons in QDs, which is inversely proportional to Γ_{rad} (*i.e.,* $\Gamma_{rad} = \tau_{rad}^{-1}$). It is clear that the larger the dipole moment of the transition is, the larger the emission transition rates will be, leading to shorter radiative lifetime of excitons. The local field factor, which for spherical QDs has a form $F = 3\varepsilon_s/(\varepsilon_1 + 2\varepsilon_s)$,[30] (where ε_1 and ε_s are dielectric constant of a nanocrystal and surrounding medium, respectively), also influences the lifetime.

Semiconductors with large dielectric constant, like PbSe or PbS have therefore long radiative lifetime.[5] The total lifetime of excitons in QDs combine radiative and non-radiative decay processes:

$$\frac{1}{\tau_{tot}} = \Gamma_{tot} = \Gamma_{rad} + \sum \Gamma_{nrad} \tag{1.27}$$

The non-radiative decay processes in QDs are mainly caused by surface defects and impurities and can drastically limit the luminescence properties of nanocrystals. Other non-radiative processess like Auger recombination or multiphonon quenching may also play important role in total transition rate.[30, 36]

The photoluminescence quantum yield expresses the competition between the radiative exciton recombination and all other exciton decay processes:[37]

$$QY = \frac{\Gamma_{rad}}{\Gamma_{rad} + \sum \Gamma_{nrad}} \tag{1.28}$$

It can be seen that the smaller the contribution of non-radiative processes the closer the QY is to unity.

The energy bandgap and optical properties of semiconductors depends considerably on the temperature. For instance the bulk PbSe bandgap show strong temperature dependence $E_g = 125 + \sqrt{400 + 0.256T^2}$[28]. The temperature dependence of the band gap for bulk materials is dictated by lattice thermal expansion and electron-phonon interactions. Also in semiconductor nanocrystals the energy of HOMO-LUMO interband transition depends on the temperature. Here it may be influenced by lattice thermal expansion, electron-phonon interactions, mechanical strain and thermal expansion of envelope wavefunction.[38] One can expect that the latter expansion in nanocrystals is very similar to that of macroscopic crystals. The electron-phonon coupling may influence both interband and intraband transitions. The sum of all the temperature dependent effects is reflected in optical spectra of QDs. For example, the width of the peaks observed in the optical spectra is strongly temperature dependent. Typically, the peaks become narrower as the temperature decreases. This is the consequence of the reduction of the homogeneous linewidth due to the lower population of phonon modes. The total peak width contains also broadening caused by size distribution of NCs (inhomogeneous broadening).[38, 39] It will be shown in chapter 3 that total broadening of the emission peaks of PbSe QDs are due to homogeneous and inhomogeneous broadening, and additionally also due to intervalley splitting.

1.5 Semiconductor Heteronanocrystals

This thesis focuses on the characterization and properties of heteronanocrystals. In general, a heteronanocrystal can be defined as a particle composed of two different semiconductors joined together by one or more heterointerfaces. Combining different semiconductor nanomaterials can result in new properties rising from the quantum mechanical interaction between the two parts. These properties depend on the size and shape of each component of HNC and on the structure of the interface. Nowadays, heteronanostructure engineering is one of the fastest growing fields in nanoscience. Heteronanostructures can be fabricated by different methods like molecular beam epitaxy (MBE) or vapour phase epitaxy (VPE), and also by colloidal synthesis.[40, 41] Colloidal chemistry is perhaps more versatile providing enormous possibility in the variation of composition, shape and size of the colloidal heteronanocrystals. Heteronanocrystals can also be composed from semiconductors and metals. For instance metals and semiconductors (*e.g.,* Co/CdSe[42]), metals and insulator (*e.g.,* Au/Fe_3O_4[43]), different semiconductors (*e.g.,* CdTe/CdSe,[44] PbSe/CdSe[45]) and many more materials combinations are possible. HNCs based on multi-components (*e.g.,* colloidal CdSe/(Cd,Zn)S/ZnS and InAs/InP/ZnSe core/multishell QDs) have also been reported. [15, 46] Combining different nanomaterials allows for instance to mix magnetic and optical properties in one HNC (*e.g.*, FePt/PbS and FePt/PbSe dumbbells and core/shell HNC.[47] Heteronanocrystals can be covered by biocompatible coating layers which makes them stabilized and functionalized for biological imaging (*e.g.*, CdSe/CdS/ZnS lipid-coated core/shell/shell QDs).[48] Combining of different materials with different crystallographic structure by colloidal synthesis method provides the possibility of wide HNCs shape designing. The HNCs shapes like *e.g.*, core/shell dots, core/shell rods, multi-shell dots and rods, heterodimers, heterotetrapods, dots in rods/cubes and many others have already been reported.[16, 17, 49-52]

Heteronanocrystals composed of different materials, share one or more crystalographic interfaces named heterojunctions. The band alignment across a heterojunction is of pivotal importance. Depending on the energy offset between the HOMO and LUMO levels, three different electron-hole localization regimes are possible after photoexcitation, named Type I, Type $I^{1/2}$ and Type II.[17] Figure 1.9 show schematic representation of these three localization regimes in core/shell QDs model.

In the Type I regime, the electron and hole are confined in one of the semiconductor materials (the one with smaller energy band gap), resulting in a large overlap of the electron and hole wavefunctions. Conversely, in the Type II situation the electron and hole are spatially separated. This leads to the formation of spatially indirect excitons across the heterojunction. In the Type $I^{1/2}$ regime, one charge carrier is localized in one semiconductor,

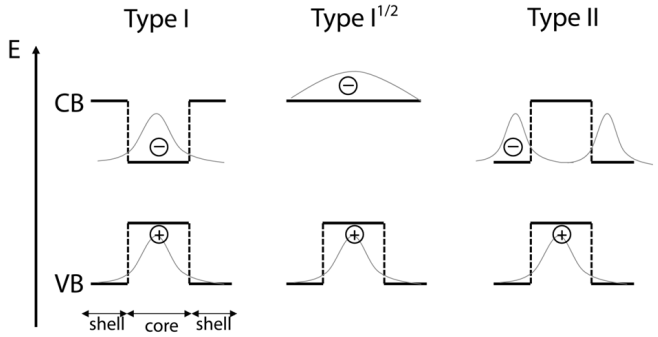

Fig. 1.9 Schematic representation of electron and hole localization regimes for core/shell QD model. The electron and hole wavefunction (grey line) are also sketched.

while the other is delocalized over the whole HNC. In principle, controlling the size, shape and composition of each HNC component, allows one to tune the energy offsets.

The best studied Type I HNCs are core/shell (CS) QDs, where the first system (CdSe/ZnS) was reported in 1996.[53] In type I CS HNCs, the shell is typically used to improve the stability against photodegradation and enhance the fluorescent quantum yield PL QY. In other words, the shell is used to passivate surface of the core and the PL QY of the Type I CS systems are high ($\geq$ 50%).[17] The emission and absorption spectra remain basically unchanged after shell overgrowth. However, a small red shift can be observed due to partial leakage of the exciton wavefunction into the shell, which occurs if the energy offset between two materials is finite. The exciton radiative lifetime remains unchanged after shell overgrowth, however the total lifetime becomes longer due to the decrease of the non-radiative recombination rate. The energy difference between the emission peak position and first absorption peak position (named non-resonant Stokes shift), remains also unchanged. Examples of type I CS HNC are: small CdSe/CdS, InP/ZnS, PbSe/PbS, PbSe/$PbSe_xS_{1-x}$.[54-58]

CdSe/CdS CS QDs are a typical example of Type $I^{1/2}$ HNCs.[59] In this system, the energy offset for the electron is too small to confine it in CdSe core and electron wavefunction is extended over the whole HNC range. The hole is however localized in the CdSe core. The opposite situation can be observed for ZnSe/CdSe CS QDs [60] where the electron localizes in CdSe shell and the hole is delocalized over the entire HNC. In both cases the electron-hole overlap decreases due to delocalization of one of the charges. Therefore, the matrix element for interband transitions (eq. 1.22) becomes smaller in magnitude reducing the

rates of light absorption and emission. The weaker confinement of the charge carriers results in a red shift of the allowed optical transitions. The Stokes shift however, remains small and comparable to that of Type I HNCs. The quantum yield can be high for Type $I^{1/2}$ HNCs.[17] There are several examples of Type $I^{1/2}$ HNCs, *e.g.*, CdSe/CdS (dot core/rod shell nanorods), CdTe/CdSe (core/thin shell HNC) or PbSe/CdSe (core/thin shell QDs).[17]

The Type II regime has been observed in heteronanocrystals of various shapes and compositions: CdTe/CdSe,[34] CdSe/ZnTe,[61] ZnTe/CdTe.[62] In this case, in which carriers are localized in two different parts of HNC, the electron-hole overlap becomes even smaller (compared to Type $I^{1/2}$), what leads to weaker absorption transition rate and much longer radiative lifetime. There is also a large redshift observed in emission and absorption spectra. It is important to realize that spatially indirect exciton transitions involve states in different materials (two different sets of k values coming from two independent Brillouin zones, where each of them has its own origin in k space). This leads to larger relaxation after photoexcitation, causing larger Stokes shifts. The quantum yield of Type II HNC is usually rather low. The reason for this may be that long radiative lifetimes result in a domination by faster non-radiative processes. However, recent work has shown that the QYs of Type II HNCs may be as high as those of Type I and Type $I^{1/2}$ HNCs.[44, 63] Type II HNCs with their interesting optical properties are now extensively investigated. These materials hold promise for a large range of possible applications.[58, 64, 65]

The colloidal PbSe/CdSe QDs investigated in this thesis can be classified as Type I or Type $I^{1/2}$ HNCs, depending on the core diameter and shell thickness (see Chapter 2).

Heterointerfaces play an important role on the optical properties and shape of HNCs. The small sizes and big surface to volume ratio of colloidal HNCs provide quite big number of crystal facets and hence interfaces. The surface free energy and interfacial free energy are therefore of crucial importance. In general, a system will always evolve forwards a direction that minimizes the total free energy. Consequently, the shape and structure of HNCs can undergo remarkable transitions upon changes in the temperature or pressure.[16, 17, 66-69] For instance, thermally induced recrystallization of Fe_2O_3-CdS and Au-Ag_2S from concentric core/shell QDs to heterodimer HNCs were found.[69, 70] Furthermore, thermal annealing may lead to crystal unification via oriented attachment (*e.g.,* PbSe QDs transformed into wide one/two dimensional nanostructures [71]). Interdiffusion of HNC into alloys may also be possible upon thermal treatment (*e.g.*, CdSe/ZnSe CS QDs transformed into gradient alloy (Cd.Zn)Se QD).[72] The temperature is thus an important parameter influencing shape and structure of HNCs. The thermal reconstruction of PbSe/CdSe CS QDs into PbSe/CdSe bi-hemisphere HNCs will be presented in Chapter 4 of this thesis.

1.6 Scanning Tunneling Microscopy and Spectroscopy

Scanning tunnelling microscopy (STM) and spectroscopy (STS) are powerful techniques providing essential information about the topography and electronic structure of individual semiconductor NCs with sub-nanometer spatial resolution. The inventors of the first scanning tunnelling microscope (STM) were Gerd Binnig and Henrich Rohrer from IBM Research Laboratory in Ruschlikon near Zurich. In 1978 they have started the study of processes of growth, structure and electronic properties of very thin oxide layers. The invention of the STM in 1982 allowed them to observe the topography of a gold Au(110) surface with atomic-resolution.[73] In 1986 G. Binnig and H. Rohrer received the Nobel prize for the invention of the STM. Before the invention of the scanning tunnelling microscope, the main source of topographic information of crystals were given by diffraction techniques,[75] which provide structure information in reciprocal space. The STM was the first device giving the information about crystal surface in real space.

The working principle of the scanning tunnelling microscope is based on the tunnelling effect,[33, 76] *i.e.,* tunnelling of the electron (or hole) through a potential barrier between two metals (conductive electrodes), as schematically presented in Fig. 1.10A. From a classical point of view, a particle travelling from left to right with energy E smaller than the height of the potential barrier V_0 will not come over the barrier but will be reflected from the barrier and start to travel in the opposite direction. According to quantum mechanics, the situation looks completely different. Here, if the electron (hole) energy is smaller than the barrier height there is a nonzero probability that the particle will tunnel through the barrier. The probability of this process can be obtained using the Schrödinger formalism and depends on the barrier height and width. We consider a tunnelling barrier that has a height ϕ and width s, and electrodes that are polarised by potential differences (bias voltage) V, as presented in Figure 1.10B. As a result of applied bias voltage, the Fermi levels (*i.e.*, the levels above which all states are empty) of both metals become mutually shifted. More precisely, opposite to filled states (left) there are empty states (right), therefore the tunnelling of electron from metal 1 to metal 2 is possible.

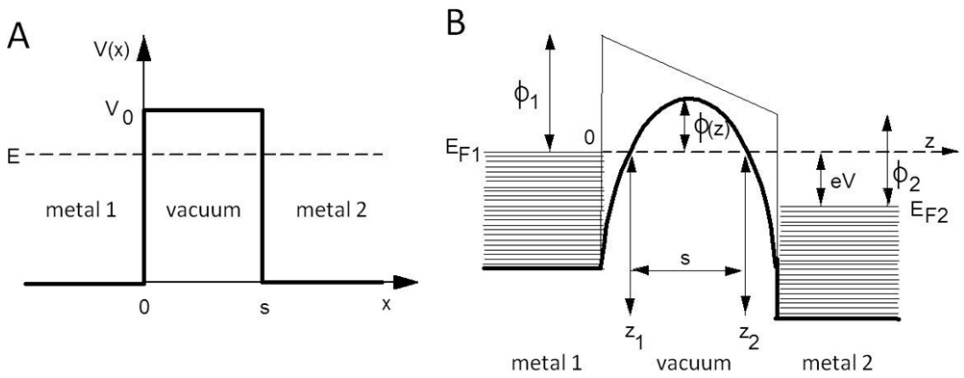

Fig. 1.10 (A) Schematic representation of simplified rectangular potential barrier. (B) More realistic view of tunnelling junction with potential difference *V*. E_{F1} and E_{F2} are the Fermi levels of both metals. The height and width of the barrier is presented as ϕ and *s*, respectively, and ϕ_1 and ϕ_2 are the work functions of two metals. Redrawn from [74]

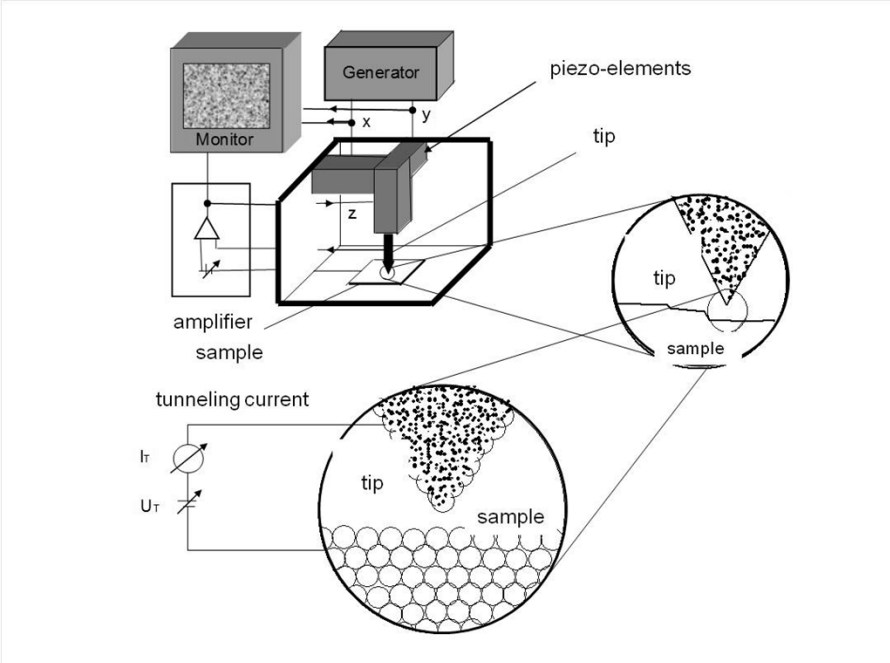

Fig. 1.11 Schematic representation of STM set-up with piezo manipulator controlling the position of tip in *x,y,x,* dimensions.

The tunnelling current measured through the potential barrier is related to the probability of finding the electron on the other side of the barrier, and has the following form:[74]

$$I \propto exp\left(-2\left[\frac{8\pi^2 m\phi}{h^2}\right]^{1/2} s\right) eV \tag{1.29}$$

It can be seen that the tunnelling current depends exponentially on the barrier height ϕ and width *s* and linearly on the bias voltage *V*.

The bias voltage is applied between two electrodes, which are the scanning tip and the measured sample. The distance between the tip and the sample is usually less than 1 nm. The tunnelling current gives information about the topography of the sample. This information is acquired by monitoring the current as the tip scans across the surface, and is usually represented in STM image form. The tip position in *x,y,x,* dimensions is manipulated by piezo-elements (see Fig. 1.11) which are controlled by feedback loop system, preventing crashing the tip on the sample. STM can provide images of the sample surface with sub-Ångstrom resolution.

Besides topography images, measurement of the tunnelling current as a function of applied bias (*i.e.*, tunnelling spectroscopy) can provide information about the local density of states (LDOS) through spectroscopy by varying tip-sample bias voltage. This method is commonly called scanning tunnelling spectroscopy (STS). Here, the local density of states is proportional to the derivative of tunnelling current with respect to bias voltage V_b:

$$\frac{dI}{dV_b} \propto LDOS(eV_b) \tag{1.30}$$

By using STS, the discrete energy levels of the valence and conduction bands of a nanocrystal can be measured. In order to study single QD with STM/STS the nanocrystals, which are usually present in a colloidal suspension, have to be deposited on atomically flat conducting substrates. Therefore, the tip-nanocrystal-substrate system forms a double barrier tunnelling junction (DBTJ), as presented in Fig. 1.12.

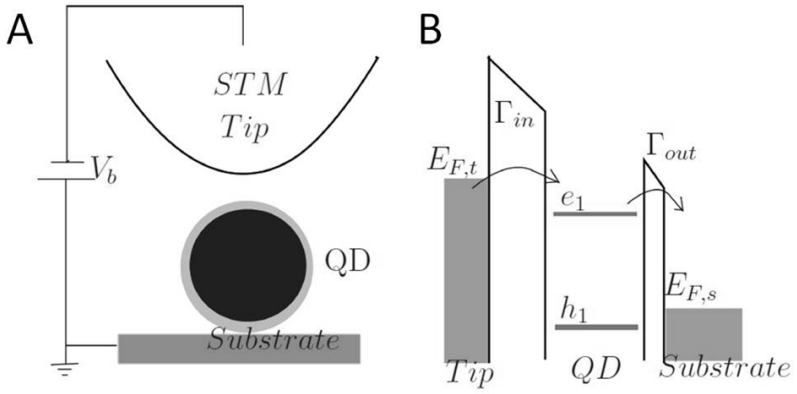

Fig. 1.12 (A) An illustration of the tip-QD-substrate configuration in the STM measurement. (B) The energy configuration of the two tunnelling junctions, where e_1 is the lowest conduction level of the QD and h_1 is the highest valence level. The Fermi energies of the tip and the substrate have a relation as : $E_{F,t} = E_{F,s} + eV_b$. Reprinted from.[77]

Figure 1.12B presents an schematic diagram of the energy configuration of DBTJ. In the situation where the applied bias voltage is small (or zero), the Fermi levels of tip and the substrate are located between the HOMO and LUMO gap of the QDs. This means that current transport is not possible, and direct tunnelling between tip and the substrate does not occur with significant probability. However, if a sufficient positive (negative) bias voltage is applied, the Fermi level of the tip can become resonant with the LUMO (HOMO) of the QD. This leads to opening of the tunnelling channel resulting in a increasing of step in the measured current. Steps in the current correspond to peaks in the tunnelling spectrum (dI/dV_b vs. V_b). Further increase of the bias voltage does not cause any changes in the tunnelling current until the next energy level of QD become resonant with the Fermi level of the tip.[77]

The double barrier tunnelling junction is usually used in a very asymmetric configuration, *i.e.,* the tip-QD barrier width considerably larger than the QD-substrate barrier width. Therefore, most of the applied bias voltage drops between tip and QD;. the fraction (η) is expressed as:[78]

$$\eta = \frac{V_{QD} - V_t}{V_b} \qquad (0 < \eta < 1) \tag{1.31}$$

where V_t is electrochemical potential of the tip, V_{QD} is the potential at the centre of the QD and V_b is the total applied potential difference over the DBTJ (bias voltage). Knowledge of the bias voltage distribution is important in order to obtain quantitative information about the energy levels of the QDs. The η parameter differs for different QD material and also inappreciably depends on QD radius, tip-QD distance and tip radius.[79]

A tunnelling current in such a junction implies tunnelling across two barriers, the tip-QD and QD-substrate barrier, respectively. This involves two tunnelling rates which are denoted as Γ_{in} (into the QD) and Γ_{out} (out of QD). The ratio Γ_{in}/Γ_{out} determines the number of additional charge carriers in the QD at a given bias voltage. Depending on tunnelling rates there are two possible tunnelling regimes: shell tunnelling and shell-filling.[80] The shell-tunnelling regime appears when $\Gamma_{in} \ll \Gamma_{out}$. Here, a single electron tunnels from tip to the QD and leaves the QD before a second electrons arrives. There is no more than one added electron at a time, thus no repulsion between tunnelling electrons is present. Hence, the peaks in tunnelling spectrum of QD in the shell-tunnelling regime directly reflect the density of states of the QD. In contrast when $\Gamma_{in} \gg \Gamma_{out}$ the shell-filling regime is observed, in which electrons accumulate in QD. It can be obtained by bringing the tip closer to the QD. The number of added electrons depends on the bias voltage. The degeneracy of the energy levels is lifted due to Coulomb interactions between the charges, therefore the tunnelling spectrum of QD in shell-filling regime shows additional resonances.

Scanning tunnelling microscopy and spectroscopy can provide essential information over the electronic structure of the nanocrystal, where in principle all the energy levels can be observed. In chapter 5 of this thesis, a STM and STS study of PbSe/CdSe HNCs will be presented.

1.7 Outline of this Thesis

This thesis focuses on the structural characterization and the opto-electronic properties of PbSe/CdSe core/shell QDs and on the structural and morphological evolution of PbSe/CdSe core/shell QDs upon thermal annealing under vacuum.

Chapter 2 describes the synthesis, structural characterization and room-temperature optical properties of PbSe/CdSe core/shell QDs for different core and shell thickness. Electron and hole scavengers are used in order to study the carrier localization regimes. The experiments show that addition of electron scavenger leads to complete quenching of the PbSe/CdSe photoluminescence, while a hole scavenger does not. This confirms that

electron wavefunction reaches the surface and the hole wave function is well confined to the core.

Chapter 3 deals with low-temperature optical investigations of PbSe/CdSe C/S QDs with the core sizes smaller than 4 nm. The photoluminescence spectra show two peaks, which are shown to reflect intrinsic exciton transitions in each quantum dot. The energy separation between the two peaks increases as the core size is reduced. Most likely, the energy separation between the peaks is due to inter-valley coupling between the L- points of PbSe.

In Chapter 4, the structural and morphological evolution of PbSe/CdSe core/shell QDs upon unnealing under vacuum is investigated. It is shown that before annealing the PbSe core has an octahedral morphology with several (111) facets, and the CdSe shell has a zincblende crystal structure. Thermal annealing under vacuum at temperatures between 150°C and 200°C induces a structural and morphological reconstruction in which the PbSe core and the CdSe shell are reorganized into two hemispheres joined by a common (111) Se plane. Thermal annealing leads to considerable changes in the absorption and photoluminescence properties of the colloidal suspensions.

Chapter 5 of this thesis focuses on low temperature scanning tunneling microscopy (STM) and spectroscopy (STS) investigation of PbSe/CdSe bi-hemisphere HNC which were created during annealing of PbSe/CdSe core/shell QDs in the STM ultra high vacuum chamber. Depending on the orientation of the PbSe/CdSe bi-hemispheres in the double barrier tunneling junction many different and non-trivial spectra can be observed.

References

1. Feynman, R.P., *There's plenty of room at the bottom [data storage]*. Microelectromechanical Systems, Journal of, 1992. **1**(1): p. 60-66.
2. Murray, C.B., D.J. Norris, and M.G. Bawendi, *Synthesis and characterization of nearly monodisperse CdE (E = sulfur, selenium, tellurium) semiconductor nanocrystallites.* Journal of the American Chemical Society, 1993. **115**(19): p. 8706-8715.
3. Henglein, A., *Small-particle research: physicochemical properties of extremely small colloidal metal and semiconductor particles.* Chemical Reviews, 1989. **89**(8): p. 1861-1873.
4. Weller, H., *Colloidal Semiconductor Q-Particles: Chemistry in the Transition Region Between Solid State and Molecules.* Angewandte Chemie International Edition in English, 1993. **32**(1): p. 41-53.
5. Rogach, A.L., *Semiconductor Nanocrystal Quantum Dots. Synthesis, Assembly, Spectroscopy and Applications*. 2008: SpringerWienNewYork.
6. Brus, L.E., *Electron--electron and electron-hole interactions in small semiconductor crystallites: The size dependence of the lowest excited electronic state.* The Journal of Chemical Physics, 1984. **80**(9): p. 4403-4409.

7. Bawendi, M.G., M.L. Steigerwald, and L.E. Brus, *The Quantum Mechanics of Larger Semiconductor Clusters ("Quantum Dots").* Annual Review of Physical Chemistry, 1990. **41**(1): p. 477-496.
8. Efros, A.L., A.L. Efros, *Interband absorption of light in a semiconductor sphere.* Soviet Physics Semiconductor-USSR, 1982. **16**: p. 772-775.
9. Ekimov, A.I. and A.A. Onushchenko, *Quantum-size effect in optical spectra of semiconductor microcrystals.* Semiconductors, 1982. **16**: p. 1209-1214.
10. Klimov, V.I., *Nanocrystal Quantum Dots. From fundamental photophysics to multicolor lasing.* Los Alamos Science, 2003. **28**: p. 214-220.
11. Liljeroth, P., P.A.Z. van Emmichoven, S.G. Hickey, H. Weller, B. Grandidier, G. Allan, and D. Vanmaekelbergh, *Density of States Measured by Scanning-Tunneling Spectroscopy Sheds New Light on the Optical Transitions in PbSe Nanocrystals.* Physical Review Letters, 2005. **95**(8): p. 086801.
12. Gaponenko, S.V., *Introduction to Nanophotonics*. 2010: Cambridge University Press. 465.
13. Cho, A.Y. and J.R. Arthur, *Molecular beam epitaxy.* Progress in Solid State Chemistry, 1975. **10, Part 3**(0): p. 157-191.
14. Hawkins, D.T., *Chemical Vapor Deposition, A Bibliography*. 1981, New York: Plenum.
15. de Mello Donegá, C., P. Liljeroth, and D. Vanmaekelbergh, *Physicochemical Evaluation of the Hot-Injection Method, a Synthesis Route for Monodisperse Nanocrystals.* Small, 2005. **1**(12): p. 1152-1162.
16. Cozzoli, P.D., T. Pellegrino, and L. Manna, *Synthesis, properties and perspectives of hybrid nanocrystal structures.* Chemical Society Reviews, 2006. **35**(11): p. 1195-1208.
17. de Mello Donegá, C., *Synthesis and properties of colloidal heteronanocrystals.* Chemical Society Reviews, 2011. **40**: p. 1512.
18. Yin, Y. and A.P. Alivisatos, *Colloidal nanocrystal synthesis and the organic-inorganic interface.* Nature, 2005. **437**(7059): p. 664-670.
19. Murray, C.B., C.R. Kagan, and M.G. Bawendi, *Synthesis and Characterization of Monodisperse Nanocrystals and Close-Packed Nanocrystal Assemblies.* Annual Review of Materials Science, 2000. **30**(1): p. 545-610.
20. Grodzińska, D., J. Van Rijssel, M. Van Huis, A. Meijerink, C. de Mello Donegá, and D. Vanmaekelbergh, *Two-fold emission from the S-shell of PbSe(core)/CdSe(shell) quantum dots.* Small, 2011. (see also Chapter 3 of this thesis)
21. Gaponenko, S.V., *Optical Properties of Semiconductor Nanocrystals*. Cambrige U.K. 1998: Cambridge University Press.
22. Koole, R., *Fundamentals and Applications of Semiconductor Nanocrystals. A study on the synthesis, optical properties, and interactions of quantum dots*. 2008, Ph.D. Thesis, Utrecht University: Utrecht.
23. Aerts, M., C.S. Suchand Sandeep, Y. Gao, T.J. Savenije, J.M. Schins, A.J. Houtepen, S. Kinge, and L.D.A. Siebbeles, *Free Charges Produced by Carrier Multiplication in Strongly Coupled PbSe Quantum Dot Films.* Nano Letters, 2011. **11**(10): p. 4485-4489.
24. Talgorn, E., Y. Gao, M. Aerts, L.T. Kunneman, J.M. Schins, T.J. Savenije, A. van HuisMarijn, S.J. van der ZantHerre, A.J. Houtepen, and D.A. SiebbelesLaurens, *Unity quantum yield of photogenerated charges and band-like transport in quantum-dot solids.* Nat Nano, 2011. **6**(11): p. 733-739.
25. An, J.M., A. Franceschetti, S.V. Dudiy, and A. Zunger, *The Peculiar Electronic Structure of PbSe Quantum Dots.* Nano Letters, 2006. **6**(12): p. 2728-2735.
26. Kang, I. and F.W. Wise, *Electronic structure and optical properties of PbS and PbSe quantum dots.* J. Opt. Soc. Am. B, 1997. **14**(7): p. 1632-1646.

27. Ellingson, R.J., M.C. Beard, J.C. Johnson, P. Yu, O.I. Micic, A.J. Nozik, A. Shabaev, and A.L. Efros, *Highly Efficient Multiple Exciton Generation in Colloidal PbSe and PbS Quantum Dots.* Nano Letters, 2005. **5**(5): p. 865-871.
28. Allan, G. and C. Delerue, *Confinement effects in PbSe quantum wells and nanocrystals.* Physical Review B, 2004. **70**(24): p. 245321.
29. Koole, R., G. Allan, C. Delerue, A. Meijerink, D. Vanmaekelbergh, and Arjan J. Houtepen, *Optical Investigation of Quantum Confinement in PbSe Nanocrystals at Different Points in the Brillouin Zone.* Small, 2008. **4**(1): p. 127-133.
30. Delerue, C. and M. Lannoo, *Nanostructures. Theory and Modeling*. 2004: Springer. 304.
31. Houtepen, A.J., *Charge injection and transport in quantum confined and disordered systems*. 2007, Ph.D. Thesis, Utrecht University: Utrecht. p. 26.
32. Klimov, V.I., C.J. Schwarz, D.W. McBranch, C.A. Leatherdale, and M.G. Bawendi, *Ultrafast dynamics of inter- and intraband transitions in semiconductor nanocrystals: Implications for quantum-dot lasers.* Physical Review B, 1999. **60**(4): p. R2177-R2180.
33. Bransden, B.H. and C.J. Joachain, *Quantum Mechanics*. 2 ed. 2000: Pearson. 803.
34. de Mello Donegá, C., *Formation of nanoscale spatially indirect excitons: Evolution of the type-II optical character of CdTe/CdSe heteronanocrystals.* Physical Review B, 2010. **81**(16): p. 165303.
35. de Mello Donegá, C. and R. Koole, *Size Dependence of the Spontaneous Emission Rate and Absorption Cross Section of CdSe and CdTe Quantum Dots.* The Journal of Physical Chemistry C, 2009. **113**(16): p. 6511-6520.
36. Klimov, V.I., S.A. Ivanov, J. Nanda, M. Achermann, I. Bezel, J.A. McGuire, and A. Piryatinski, *Single-exciton optical gain in semiconductor nanocrystals.* Nature, 2007. **447**(7143): p. 441-446.
37. J.R. Lakowicz, *Principles of Fluorescence Spectroscopy*. 3 ed. 2006: Springer. 954.
38. Olkhovets, A., R.C. Hsu, A. Lipovskii, and F.W. Wise, *Size-Dependent Temperature Variation of the Energy Gap in Lead-Salt Quantum Dots.* Physical Review Letters, 1998. **81**(16): p. 3539.
39. Fernee, M.J., P. Jensen, and H. Rubinsztein-Dunlop, *Origin of the large homogeneous line widths obtained from strongly quantum confined PbS nanocrystals at room temperature.* Journal of Physical Chemistry C, 2007. **111**(13): p. 4984-4989.
40. Springholz, G. and G. Bauer, *Molecular beam epitaxy of IV-VI semiconductor hetero- and nano-structures.* physica status solidi (b), 2007. **244**(8): p. 2752-2767.
41. Bhattacharya, P., S. Ghosh, and A.D. Stiff-Roberts, *Qunatum Dot Opto-Electronic Devices.* Annual Review of Materials Research, 2004. **34**(1): p. 1-40.
42. Kim, H., M. Achermann, L.P. Balet, J.A. Hollingsworth, and V.I. Klimov, *Synthesis and Characterization of Co/CdSe Core/Shell Nanocomposites: Bifunctional Magnetic-Optical Nanocrystals.* Journal of the American Chemical Society, 2004. **127**(2): p. 544-546.
43. Shi, W., H. Zeng, Y. Sahoo, T.Y. Ohulchanskyy, Y. Ding, Z.L. Wang, M. Swihart, and P.N. Prasad, *A General Approach to Binary and Ternary Hybrid Nanocrystals.* Nano Letters, 2006. **6**(4): p. 875-881.
44. Chin, P.T.K., C. de Mello Donegá, S.S. van Bavel, S.C.J. Meskers, N.A.J.M. Sommerdijk, and R.A.J. Janssen, *Highly Luminescent CdTe/CdSe Colloidal Heteronanocrystals with Temperature-Dependent Emission Color.* Journal of the American Chemical Society, 2007. **129**(48): p. 14880-14886.
45. Pietryga, J.M., D.J. Werder, D.J. Williams, J.L. Casson, R.D. Schaller, and V.I. Klimov, *Utilizing the Lability of Lead Selenide to Produce Heterostructured Nanocrystals with Bright, Stable Infrared Emission.* Journal of the American Chemical Society, 2008. **130**(14): p. 4879-4885.

46. Xie, R., K. Chen, X. Chen, and X. Peng, *InAs/InP/ZnSe core/shell/shell quantum dots as near-infrared emitters: Bright, narrow-band, non-cadmium containing, and biocompatible.* Nano Research, 2008. **1**(6): p. 457-464.
47. Lee, J.-S., M.I. Bodnarchuk, E.V. Shevchenko, and D.V. Talapin, *"Magnet-in-the-Semiconductor" FePt-PbS and FePt-PbSe Nanostructures: Magnetic Properties, Charge Transport, and Magnetoresistance.* Journal of the American Chemical Society, 2010. **132**(18): p. 6382-6391.
48. Skajaa, T., Y. Zhao, D.J. van den Heuvel, H.C. Gerritsen, D.P. Cormode, R. Koole, M.M. van Schooneveld, J.A. Post, E.A. Fisher, Z.A. Fayad, C. de Mello Donega, A. Meijerink, and W.J.M. Mulder, *Quantum Dot and Cy5.5 Labeled Nanoparticles to Investigate Lipoprotein Biointeractions via Förster Resonance Energy Transfer.* Nano Letters, 2010. **10**(12): p. 5131-5138.
49. Fu, A., W. Gu, B. Boussert, K. Koski, D. Gerion, L. Manna, M. Le Gros, C.A. Larabell, and A.P. Alivisatos, *Semiconductor Quantum Rods as Single Molecule Fluorescent Biological Labels.* Nano Letters, 2007. **7**(1): p. 179-182.
50. Houtepen, A.J., R. Koole, D. Vanmaekelbergh, J. Meeldijk, and S.G. Hickey, *The Hidden Role of Acetate in the PbSe Nanocrystal Synthesis.* Journal of the American Chemical Society, 2006. **128**(21): p. 6792-6793.
51. Kanaras, A.G., C. SÃ¶nnichsen, H. Liu, and A.P. Alivisatos, *Controlled Synthesis of Hyperbranched Inorganic Nanocrystals with Rich Three-Dimensional Structures.* Nano Letters, 2005. **5**(11): p. 2164-2167.
52. Ma, C., Y. Ding, D. Moore, X. Wang, and Z.L. Wang, *Single-Crystal CdSe Nanosaws.* Journal of the American Chemical Society, 2003. **126**(3): p. 708-709.
53. Hines, M.A. and P. Guyot-Sionnest, *Synthesis and Characterization of Strongly Luminescing ZnS-Capped CdSe Nanocrystals.* The Journal of Physical Chemistry, 1996. **100**(2): p. 468-471.
54. Sashchiuk, A., L. Langof, R. Chaim, and E. Lifshitz, *Synthesis and characterization of PbSe and PbSe/PbS core-shell colloidal nanocrystals.* Journal of Crystal Growth, 2002. **240**(3-4): p. 431-438.
55. Pan, D., Q. Wang, S. Jiang, X. Ji, and L. An, *Synthesis of Extremely Small CdSe and Highly Luminescent CdSe/CdS Core-Shell Nanocrystals via a Novel Two-Phase Thermal Approach.* Advanced Materials, 2005. **17**(2): p. 176-179.
56. Haubold, S., M. Haase, A. Kornowski, and H. Weller, *Strongly Luminescent InP/ZnS Core–Shell Nanoparticles.* ChemPhysChem, 2001. **2**(5): p. 331-334.
57. Brumer, M., A. Kigel, L. Amirav, A. Sashchiuk, O. Solomesch, N. Tessler, and E. Lifshitz, *PbSe/PbS and PbSe/PbSexS1–x Core/Shell Nanocrystals.* Advanced Functional Materials, 2005. **15**(7): p. 1111-1116.
58. Lifshitz, E., M. Brumer, A. Kigel, A. Sashchiuk, M. Bashouti, M. Sirota, E. Galun, Z. Burshtein, A.Q. Le Quang, I. Ledoux-Rak, and J. Zyss, *Air-Stable PbSe/PbS and PbSe/PbSexS1-x Core-Shell Nanocrystal Quantum Dots and Their Applications* The Journal of Physical Chemistry B, 2006. **110**(50): p. 25356-25365.
59. Li, J.J., Y.A. Wang, W. Guo, J.C. Keay, T.D. Mishima, M.B. Johnson, and X. Peng, *Large-Scale Synthesis of Nearly Monodisperse CdSe/CdS Core/Shell Nanocrystals Using Air-Stable Reagents via Successive Ion Layer Adsorption and Reaction.* Journal of the American Chemical Society, 2003. **125**(41): p. 12567-12575.
60. Ivanov, S.A., A. Piryatinski, J. Nanda, S. Tretiak, K.R. Zavadil, W.O. Wallace, D. Werder, and V.I. Klimov, *Type-II Core/Shell CdS/ZnSe Nanocrystals: Synthesis, Electronic Structures, and Spectroscopic Properties.* Journal of the American Chemical Society, 2007. **129**(38): p. 11708-11719.

61. Chen, C.-Y., C.-T. Cheng, J.-K. Yu, S.-C. Pu, Y.-M. Cheng, P.-T. Chou, Y.-H. Chou, and H.-T. Chiu, *Spectroscopy and Femtosecond Dynamics of Type-II CdSe/ZnTe Core-Shell Semiconductor Synthesized via the CdO Precursor.* The Journal of Physical Chemistry B, 2004. **108**(30): p. 10687-10691.
62. Xie, R., X. Zhong, and T. Basché, *Synthesis, Characterization, and Spectroscopy of Type-II Core/Shell Semiconductor Nanocrystals with ZnTe Cores.* Advanced Materials, 2005. **17**(22): p. 2741-2745.
63. Groeneveld, E., S. van Berkum, M.M. van Schooneveld, A. Gloter, J.D. Meeldijk, D.J. van den Heuvel, H.C. Gerritsen, and C. de Mello Donega, *Highly Luminescent (Zn,Cd)Te/CdSe Colloidal Heteronanowires with Tunable Electron-Hole Overlap.* Nano Letters, 2012. **12**(2): p. 749-757.
64. Schrier, J., D.O. Demchenko, Wang, and A.P. Alivisatos, *Optical Properties of ZnO/ZnS and ZnO/ZnTe Heterostructures for Photovoltaic Applications.* Nano Letters, 2007. **7**(8): p. 2377-2382.
65. Jian Xu, Dehu Cui, Ting Zhu, Gary Paradee, Ziqi Liang, Qing Wang, S. Xu, and a.A.Y. Wang, *Synthesis and surface modification of PbSe/PbS core–shell nanocrystals for potential device applications.* Nanotechnology, 2006. **17**: p. 5428.
66. Tolbert, S.H. and A.P. Alivisatos, *The wurtzite to rock salt structural transformation in CdSe nanocrystals under high pressure.* The Journal of Chemical Physics, 1995. **102**(11): p. 4642-4656.
67. Zahn, D., Y. Grin, and S. Leoni, *Mechanism of the pressure-induced wurtzite to rocksalt transition of CdSe.* Physical Review B, 2005. **72**(6): p. 064110.
68. Saito, H., K. Nishi, and S. Sugou, *Shape transition of InAs quantum dots by growth at high temperature.* Applied Physics Letters, 1999. **74**(9): p. 1224-1226.
69. Yang, J. and J.Y. Ying, *Diffusion of Gold from the Inner Core to the Surface of Ag2S Nanocrystals.* Journal of the American Chemical Society, 2010. **132**(7): p. 2114-2115.
70. Kwon, K.-W. and M. Shim, *g-Fe_2O_3/II-VI Sulfide Nanocrystal Heterojunctions.* Journal of the American Chemical Society, 2005. **127**(29): p. 10269-10275.
71. van Huis, M.A., L.T. Kunneman, K. Overgaag, Q. Xu, G. Pandraud, H.W. Zandbergen, and D.l. Vanmaekelbergh, *Low-Temperature Nanocrystal Unification through Rotations and Relaxations Probed by in Situ Transmission Electron Microscopy.* Nano Letters, 2008. **8**(11): p. 3959-3963.
72. Zhong, X., M. Han, Z. Dong, T.J. White, and W. Knoll, *Composition-Tunable ZnxCd1-xSe Nanocrystals with High Luminescence and Stability.* Journal of the American Chemical Society, 2003. **125**(28): p. 8589-8594.
73. Binnig, G. and H. Rohrer, *Scanning tunneling microscopy - from birth to adolescence.* Reviews of Modern Physics, 1987. **59**(3): p. 615-625.
74. Czajka, R., *(In Polish): Zastosowanie skaningowej mikroskopii i spektroskopii tunelowej do badania właściwości fizycznych układów mezoskopowych*. 1997, Poznań: Politechnika Poznańska.
75. Hasek, J., ed. *Diffraction Methods in Materials Science*. 1993, Nova Science Publishers: New York.
76. Ball, D.W., *Physical chemistry*. 2003: Brooks/Cole-Thomson Learning. 817.
77. Sun, Z., *Atomic and Elactronic Structure of Quantum Dots Measured with Scanning Probe Techniques*. 2012, Ph.D Thesis,Utrecht University: Utrecht. p. 102.
78. Overgaag, K., P. Liljeroth, B. Grandidier, and D.l. Vanmaekelbergh, *Scanning Tunneling Spectroscopy of Individual PbSe Quantum Dots and Molecular Aggregates Stabilized in an Inert Nanocrystal Matrix.* ACS Nano, 2008. **2**(3): p. 600-606.
79. Overgaag, K., *Ph.D thesis. Electronic coupling in self-assembled nanocrystal arrays. A scunning tunneling microscopy study*. 2008, Utrecht University: Utrecht. p. 118.

80. Liljeroth, P., L. Jdira, K. Overgaag, B. Grandidier, S. Speller, and D. Vanmaekelbergh, *Can scanning tunnelling spectroscopy measure the density of states of semiconductor quantum dots?* Physical Chemistry Chemical Physics, 2006. **8**(33).

2

Synthesis, Structural Characterization and Optical Investigation of Colloidal PbSe/CdSe Core/Shell Quantum Dots

This chapter presents the synthesis of PbSe/CdSe core/shell quantum dots and their room temperature optical properties for different core diameters and shell thicknesses. Atomic structure of PbSe/CdSe core/shell QDs is also investigated by high-resolution transmission electron microscopy and indicates that the PbSe core has octahedral like shape with eight Se(111) interfacial planes shared with the CdSe shell. Detailed analysis of the absorption and luminescence of PbSe/CdSe core/shell QDs shows that the absorption oscillator strength of the first exciton transition agrees with that of plain PbSe QDs of comparable sizes. In contrast, the oscillator strength of the emitting transition is reduced by at least 75%, compared to PbSe QDs. Moreover, the addition of an electron scavenger quenches the PbSe/CdSe QD emission, while a hole scavenger does not. This implies that the electron wave function reaches the QD surface, while the hole is confined to the PbSe core.

2.1 Introduction

The study of colloidal heteronanocrystals is of large interest in current nanoscience. Heteronanocrystals of two different II-VI compounds have been recently studied, *e.g.,* CdTe/CdSe,[1-4] CdSe/ZnS,[5-7] CdSe/CdS,[8-11] ZnSe/CdSe,[12] CdSe/ZnTe,[4] CdSe/ZnSe[13] core/shell systems. The optical properties of such systems can be roughly classified in three categories. In the first category (*viz.,* type-I), the luminescence energy and the radiative lifetime of the core/shell system remain essentially unaltered with respect to the single component nanocrystal. In such systems, the shell forms a passivating barrier for the core wave functions reducing the non-radiative recombination at the surface and increasing the (photo)chemical stability. The second category of systems (*viz.*, type-II) is characterized by an enhanced Stokes shift between the luminescence and the lowest energy absorption peak, increased linewidths and an increase of the radiative decay rate. The third category (*viz.*, type-$I^{1/2}$) is characterized by decrease of the luminescence energy and increased radiative lifetime with respect to the single component nanocrystal, without an increase of the Stokes shift. The type I situation is often described by a model where after photoexcitation both electron and hole wavefunctions are localized in the narrower band-gap semiconductor. The Type II situation is rationalized by considering a spatially indirect exciton in which the electron and hole wave functions are centered in different parts of the heteronanocrystal, leading to a reduced overlap. In the Type $I^{1/2}$ situation, one carrier is localized in one side of heterojunction, while the second one is delocalized over the whole heteronanocrystal.

In this chapter we present an experimental study of the atomic structure and optical properties of colloidal heteronanocrystals composed of a PbSe core (a IV-VI compound) and a CdSe shell (a II-VI compound). Nanocrystals of lead chalcogenides (*e.g.,* PbSe, PbS,) have been studied extensively, due to their emission in the near-IR range.[14] Many recent studies have focused on the opto-electronic properties of PbSe colloidal semiconductor nanocrystals, which are remarkably different from bulk semiconductors. The small effective masses of the carriers ($m^*_e = m_h^* = 0.1$)[15], and hence large exciton Bohr radius (46 nm)[16], results in strong quantum confinement for relatively large nanocrystals (*viz.,* $\leq$ 92 nm). CdSe has a smaller bulk exciton Bohr radius than PbSe (4.9 nm).[17] The effective mass of the charge carriers at the bottom of the conduction band and the top of the valence band are $m_e^* = 0.13$ and $m_h^* = 0.45$.[18] CdSe nanocrystals are since long the workhorses of colloidal nanoscience. Their synthesis, electronic structure, and optical properties have been studied extensively. CdSe nanocrystals hold promise for applications as biological labels,[19, 20] as active laser material, [21] and in solar cells.[22, 23]

Heterointerfaces between II-VI and IV-VI semiconductors have been grown in the past by molecular beam epitaxy[24] and colloidal synthesis.[16, 25, 26] The PbSe/CdSe heterojunction is of considerable interest. CdSe crystallizes in wurtzite structure and has a

low refractive index (2.6[18]), while PbSe has a rocksalt crystal structure and a high refractive index (4.7[27]). Previous studies have shown that these compounds do not intermix (lattice type mismatch).[28] Further, lattice mismatch is very small (< 1%). Therefore, heterostructures consisting of PbSe and CdSe possess an atomically sharp heterointerface, consisting of a Se(111) plane.[28, 29] PbSe/CdSe core/shell nanocrystals are also of high interest for opto-electronics. The HOMO-LUMO gap of PbSe nanocrystals (NCs) is between 0.3 and roughly 1.5 eV, depending on the NC size. The bulk optical gap of CdSe is 1.6 eV, and can increase to 2.5 eV in the case of small CdSe nanocrystals. We anticipate that PbSe/CdSe core/shell systems may feature both localized and de-localized excitons, depending on the core and shell dimensions.

2.2 Experimental Section

The synthesis of PbSe NCs was performed in a Schlenk-line following the method developed by Houtepen *et al*.[30] All stock solutions were prepared inside a nitrogen-purged glovebox. First, a stock solution (S1) of 1.95 g lead acetate trihydrate (PbAc, Aldrich, 99.999%), 6 ml diphenyl ether (DPE, Aldrich), 4.5 ml oleic acid (OA, Aldrich, 90%) and 24 ml trioctyl phosphine (TOP, Fluka, 90%) was prepared. The lead oleate precursor was prepared by drying and degassing of stock solution (S1) in a Schlenk-line under vacuum ($<10^{-3}$ mbar) for > 1 hour at 100°C. Next, the precursor solution was allowed to cool to room temperature. A stock solution (S2) of 0.465 g selenium (Se powder, Alfa Aesar, 99.999%) and 6 ml TOP was prepared at 60°C in a glovebox and cooled to room temperature. 10 ml of dry DPE was heated to 200 °C. Next, a room temperature mixture of 11.5 ml S1 and 1.7 ml S2 was rapidly injected at 190 °C. The growth temperature and time were 140 °C and 1.5 minutes, respectively. The growth was quenched by rapidly injecting a mixture of 20 ml butanol and 10 ml methanol. The nanocrystals were separated from the crude reaction mixture by centrifugation at 2,500 rpm for 5 min and subsequently redissolved in toluene.

PbSe/CdSe core/shell heteronanocrystals were prepared from PbSe colloidal nanocrystals using the method of Pb^{2+}/Cd^{2+} ion exchange in solution.[27] The synthesis of the PbSe/CdSe core/shell NCs was performed inside a nitrogen-purged glove box. The synthesis was carried out by using an adaptation of method reported by Pietryga *et al*.[27] Cadmium oleate solution was prepared as follows (in a Schlenk line): 6.22 g cadmium acetate (Aldrich, 99.99%), 18 ml oleic acid and 44 ml 1-octadecene (ODE, Acros Organics) were heated and degassed under vacuum ($<10^{-3}$ mbar) for few hours at 200°C. The clear solution was cooled to ~100 °C under nitrogen. Next ,in a glovebox, 7 ml of toluene was heated to 100 °C, then 1 ml of room temperature solution of PbSe nanocrystals in toluene (conc. 1.13×10^{-5} mol/µl)

was added. Subsequently, 2.1 ml of cadmium oleate stock solution was slowly added via a syringe at 100 °C. Aliquots (ca. 0.5 ml) of the reaction mixture were taken out after 5, 10, 30, 60, 120, 240 and 360 minutes and cooled by mixing with hexane. All samples were cleaned by addition of methanol and acetone, centrifugation, and re-dissolution in tetrachloroethylene (TCE). The cleaning procedure was repeated twice.

The optical absorption measurements were performed using a Perkin-Elmer Lambda 950 UV/VIS/IR absorption spectrometer. Emission and excitation spectra were recorded on a Edinburgh Instruments FLS920 spectrofluorometer. A 450W Xe lamp and 100 W halogen lamp were used as light sources. The apparatus was equipped with an excitation double monochromator blazed at 500 nm. The sample emission was dispersed with a monochromator blazed at 1200 nm and detected by a liquid N_2 cooled Hamamatsu R5509-72 PMT.

Photoluminescence decay time measurements were performed by using a tunable dye laser (Lambda Physik LPD3000) as the excitation source and the spectrofluorometer dscribed above to select and detect the emission. The dye Coumarin 102 (tunable between 460-510 nm), was used and the wavelength of 500 nm was selected. The dye laser is pumped by a Lambda Physik LPX100 excimer (XeCl) laser, (20 ns pulse width and 10 Hz repetition rate). Decay curves were obtained using a Tektronix 2430 digital oscilloscope (150 MHz, 100 MSa/s- Simultaneous Maximum Sampling Rate/ch, 2ch) interfaced with a PC.

The resulting heteronanocrystals were investigated by high-resolution transmission electron microscopy (HR-TEM) and high-angle annular dark field scanning transmission electron microscopy (HAADF-STEM), using an aberration-corrected Titan microscope operating at 300 kV. The measurements were performed both at TU Delft and EMAT University of Antwerp (by Dr M. van Huis).

2.3 Results and Discussion

2.3.1 Structural Characterization

A selection of PbSe/CdSe core/shell quantum dots (QDs) investigated in this work is shown in Fig. 2.1. The diameter of the parent PbSe nanocrystals was 3.7± 0.3 nm. During the synthesis Pb atoms are exchanged by Cd atoms, which leads to ingrowth of a CdSe shell and simultaneous shrinking of the PbSe core. Figure 2.1 shows that the overall size and shape of the nanocrystals remains constant during the ion exchange process. The core/shell structure, however cannot be clearly visualized using low resolution TEM.

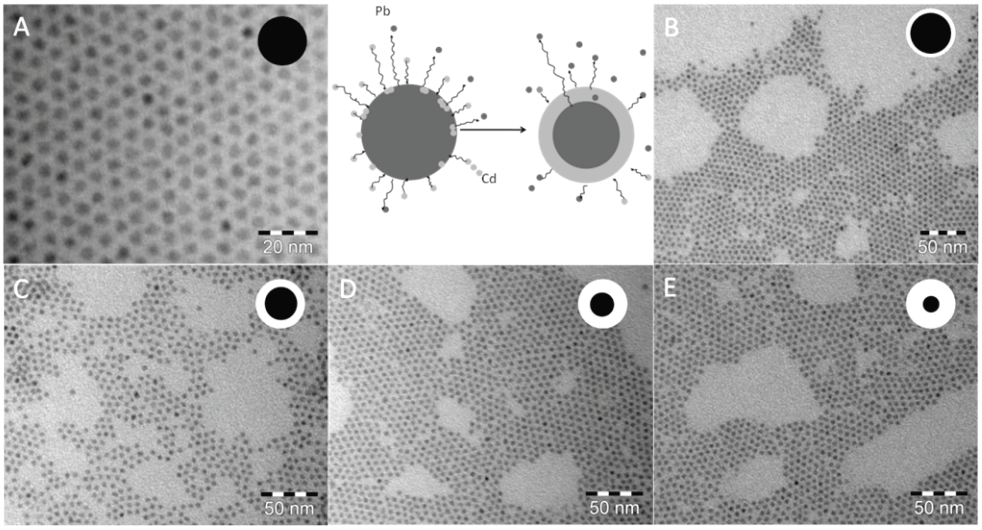

Fig. 2.1. TEM images of samples collected during the formation of PbSe/CdSe core/shell nanocrystals by Pb/Cd ion exchange starting from PbSe nanocrystals. (A) presents the parent PbSe cores (3.7 ± 0.3 nm in diameter), (B) to (E) show samples extracted from the reaction mixture at: (B) 5 min, (C) 30 min, (D) 120 min, (E) 240 min after the start of the cation-exchange process. The cation-exchange process is schematically depicted in the upper central panel.

The atomic structure of the core-shell system was further investigated by high-resolution transmission electron microscopy (HR-TEM) and HAADF-STEM. Figure 2.2 shows a clear distinction between the PbSe core and the CdSe shell lattices with atomic resolution. Several different nanocrystals presented in Fig. 2.2 show that the CdSe shell has non-uniform thickness, even for HNCs from the same batch (Fig. 2.2A). The PbSe core has an octahedral like shape. The high resolution images are presented for two different groups of HNCs (Fig. 2.2A-C with 7.6 nm of total diameter, and Fig. 2.2D-G with 5.6 nm of total diameter). Depending on the orientation of the HNC on the TEM-grid, different HNC projections can be observed. The [011] projection (Fig. 2.2B,D-G) shows a diamond shaped core with PbSe (111) edges as presented schematically in Fig. 2.2I. In this projection the CdSe shell can be clearly distinguished (crystallographic orientation of CdSe, Cd-colums) and shows a non- uniform thickness. The [001] projection (Fig. 2.2C,J) yields an approximately square view of the core with PbSe (011) edges. The shell structure, however, is less visible in this projection. The results indicate that the PbSe core has an octahedral morphology (Fig. 2.2H) with eight Se {111} interfacial planes shared with the CdSe shell.

The CdSe shell has a zinc-blende crystal structure. According to results obtained with MBE-grown PbSe/CdSe hetero-interfaces, the lattice mismatch between the {111} Se surfaces of both crystals is less than 1%[27, 31] which leads to a nearly perfect heteroepitaxial interface. The HR-TEM and HAADF-STEM pictures show that the ion-exchange process leads to the partial replacement of the PbSe lattice by the CdSe lattice, *i.e.*, "ingrowth of a CdSe shell" while the overall shape and size of the nanocrystals is preserved (see Figure 2.1).

A closer view on the atomic structure of PbSe/CdSe core/shell QDs is shown in HAADF-STEM and HR-TEM images (Fig. 2.3). The QD is imaged along the [110] axis of PbSe and CdSe and single atomic columns can be clearly distinguished. The positions of Pb, Cd and Se columns are indicated by red, green and yellow dots, respectively (Fig. 2.3.A-B).

Two clear PbSe/CdSe interfaces sharing a common Se {111} layer (marked by rectangles 1 and 2) are shown in Fig. 2.3B. The other two Se {111} interfaces were not clearly visible in this reconstruction. The analysis of Pb, Cd and Se positions indicates that the two marked interfaces are considerably different. The bottom interface (rectangle 2) shows that Pb and Cd sublattices are shifted with respect to each other. This lateral shift is a natural consequence of different crystal structures. While Pb and Cd sublattices are shifted, the Se sublattice remains coherent across the interface 2. A considerably different situation can be observed in the top interface (rectangle 1). Here, lateral shift of the Se sublattice is observed, while the Pb/Cd cation sublattice is coherent across the interface. The different nature of these two interfaces arises from the fact that Se atoms at the top interfacial layer follow the rock salt PbSe structure, whereas the Se atoms at the bottom interfacial layer follow the zincblende CdSe structure. These two different interfaces have been recently studied in detail for PbSe/CdSe dot-in-rod nanostructures.[32, 33] The heteronanocrystal interfaces are not ideally perfect and lattice defects are possible. Moreover, HAADF-STEM reconstruction can reflect additional atoms coming from crystallographic layer laying behind. Therefore, along the [110] zone axis some double Se atoms are visible (Fig. 2.3A,B). Not all four Se{111} interfaces can be clearly distinguished atom by atom due to lattice defects and the presence of additional atoms projected from parallel layers. Figure 2.3C shows the HR-TEM picture of a 7.6 nm PbSe/CdSe core/shell QD where contour of four Se {111} interfaces is visible and Pb, Se and Cd atomic layers are indicated.

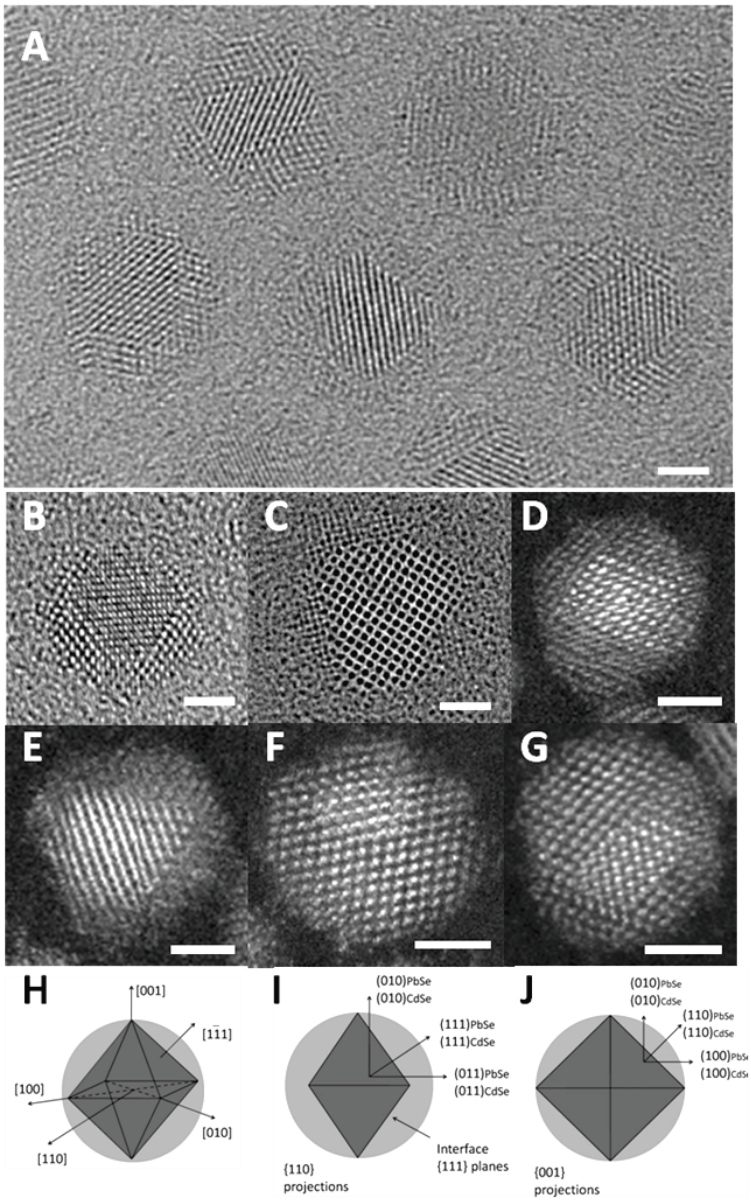

Fig. 2.2. HR-TEM (A-C) and HAADF-STEM (D-G) images of PbSe/CdSe core/shell QDs: (A) overview of a few QDs in different projections, (B,D-G) projections along the [110] axis of PbSe, (C) projection along the [001] axis of PbSe. (H-J) models of the PbSe/CdSe core/shell QDS showing: (H) the octahedral shape of the PbSe core, (I) projections along the [011] axis and (J) [001] axis. The scale bar corresponds to 2 nm.

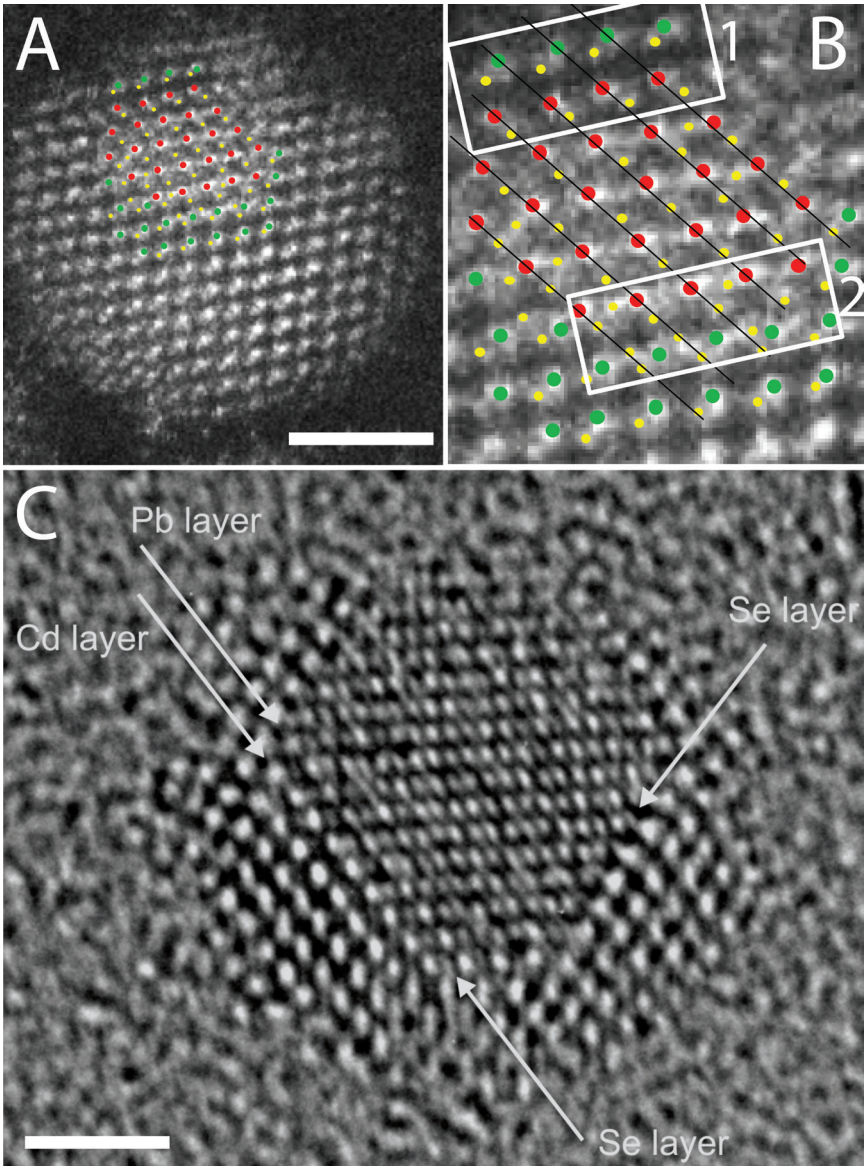

Fig. 2.3 (A) HAADF-STEM image of a 5.6 nm diameter PbSe/CdSe core/shell QD, where Pb, Cd, and Se columns are indicated by red, green, and yellow dots, respectively. (B) zoom in of image A with atomic structure of PbSe/CdSe interface indicated by rectangles 1 and 2. (C) HR-TEM image of a 7.6 nm diameter PbSe/CdSe core/shell QD with visible Pb, Cd, and Se layers. The scale bar corresponds to 2 nm.

2.3.2 Absorption, Luminescence and Excitation Spectra

The absorption spectra of parent PbSe QDs and PbSe/CdSe core/shell QDs are shown in Fig. 2.4. The parent PbSe NCs (black squares) clearly show the first absorption peak, corresponding to the $1S_h - 1S_e$ transition, and two other transitions at higher energies ($1P_h - 1P_e$ and $1D_h - 1D_e$). The corresponding optical transitions have been discussed extensively in the literature.[34-37] The full width at half maximum (FWHM) of the lowest exciton peak is between 40 meV and 70 meV, depending on the size and the monodispersity of the PbSe nanocrystal suspension, (70, 54, 40 and 64 meV, for 3.7 nm, 5.6 nm, 7.5 nm and 7.6 nm diameter, respectively). The width of the lowest exciton peak is due to inhomogeneous and homogeneous broadening. The first absorption peak is at 0.9 eV, 0.74 eV, 0.62 eV, and 0.61 eV for PbSe QDs of 3.7 nm, 5.6 nm, 7.5 nm and 7.6 nm in diameter, respectively.

The absorption spectra of PbSe/CdSe core/shell systems show a considerable shift to higher energies with increasing cation-exchange time. This can be ascribed to shrinkage of the PbSe core due to the progressive ingrowth of the CdSe shell. It can be seen that the shift of the absorption peak with increasing ion exchange time is more pronounced at earlier times. This suggests that the process of ion exchange is faster at the early stages of exchange reaction and progressively slows down with increasing thickness of the CdSe shell. Note that even after 21 hours of ion exchange, starting from PbSe nanocrystals of 5.6 nm in diameter (light blue squares in Fig. 2.4B), the first absorption peak is still in the near infrared range, indicating that there is a remaining PbSe core. The same observation applies to all of the presented PbSe/CdSe core/shell QDs investigated here, for which absorption in near infrared spectral range is clearly observed, implying that the lowest excitonic states are localized in the PbSe core.

The shift of the absorption transitions to higher energies observed upon increasing of the exchange time is ascribed to the decreasing size of the remaining PbSe core. The PbSe core size of PbSe/CdSe core/shell QDs was estimated from the first absorption peak position, using sizing curves published in literature.[38] As discussed in the previous section, the PbSe cores are not spherical but have an octahedral shape. However, for simplicity, the calculation of the volume ratio V_{sh}/V_{QD} (CdSe shell volume/total QD volume), presented in this chapter, is based on the approximation that both the core and the core/shell QDs are spherical.

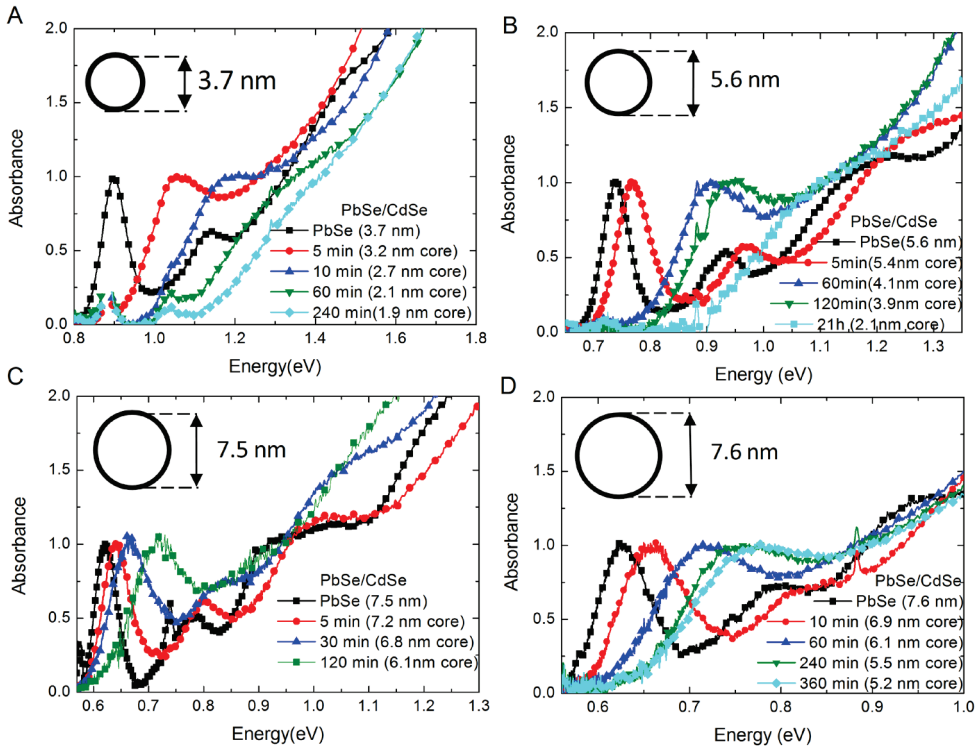

Fig. 2.4 Evolution of the absorption spectra of PbSe/CdSe core/shell nanocrystals at different stages of the ion-exchange process, *i.e.,* ingrowth of a CdSe shell. The panels present data for four different suspensions with core/shell nanocrystals of different diameter: (A) 3.7 nm, (B) 5.6 nm, (C) 7.5 nm, (D)7.6 nm. The cartoons indicate the diameter of the parent PbSe QDs.

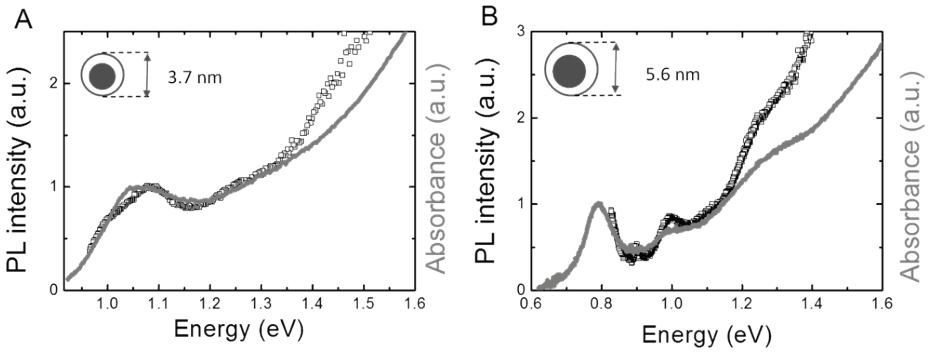

Fig. 2.5 RT Excitation (open black squares) and absorption (grey line) spectra of PbSe/CdSe core/shell QDs with total diameter of: (A) 3.7 nm (5 min of exchange time), (B) 5.6 nm (10 min of exchange time). The emission energy for excitation measurements was taken at 0.95 eV and 0.78 eV , for figure (A) and (B), respectively.

Besides the shift of all the absorption transitions to higher energies, it can also be observed that the peaks become broader with increasing ion-exchange time. We believe that the increased broadening of the absorption peaks has two origins. First, the inhomogeneity in the PbSe core size increases by progressive ingrowth of the CdSe shell. Second, the PbSe core size shrinks, which implies that the intervalley coupling becomes stronger (see Chapter 3). The small and sharp peaks around 0.9 eV are due to absorption by oleic acid.

The broadening of the lowest energy exciton transition with decreasing PbSe core diameter can also be observed in the room temperature photoluminescence excitation (PLE) spectra. Figure 2.5 combines PLE and absorption spectra of two PbSe/CdSe core/shell QD samples with different total diameter: 3.7 nm and 5.6 nm, respectively. The PLE spectra (open squares) are in good agreement with the absorption spectra (grey line). Moreover, due to the higher spectral resolution observed in PLE spectrum, the highest energy excitation peaks of larger QDs (5.6 nm, Fig. 2.5B) can be clearly seen at 1 eV and 1.25 eV. The PLE spectra of core/shell QDs with smaller diameter (3.7 nm, Fig. 2.5A) shows that the broad peak of lowest exciton state consist of two peaks, at 1 eV and 1.08 eV, respectively.

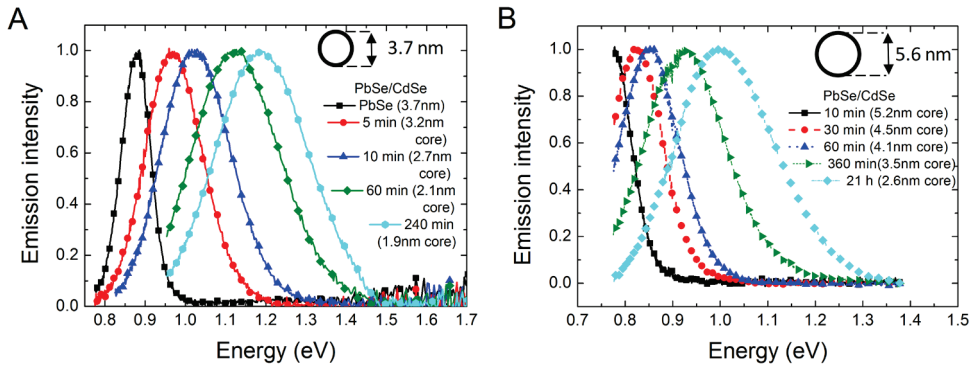

Fig. 2.6 Evolution of the photoluminescence spectra for PbSe(core)/CdSe(shell) nanocrystals of two different diameters with increasing thickness of the CdSe shell. (A): PbSe(core)/CdSe(shell) nanocrystals of 3.7 nm in diameter after: 0, 5, 10, 60, 240 minutes of ion exchange. (B): PbSe(core)/CdSe(shell) nanocrystals of 5.6 nm in diameter measured after: 10, 30 ,60, 360, 1260 minutes of ion exchange. The cut-off at low energy is due to the limited photodetector range.

The photoluminescence (PL) spectra of PbSe/CdSe core/shell are shown in Fig. 2.6. Similarly to the first peak in the absorption spectra, the emission peak shifts to higher energies and becomes broader with increasing exchange time. The maximum peak shift with increasing CdSe shell thickness is about 330 meV for core/shell QDs with a total diameter of 3.7 nm (Fig. 2.6A), and 200 meV for core/shell QDs with a total diameter of 5.6 nm (Fig. 2.6B, exclusive 21 h sample).

2.3.3 Absorption Oscillator Strength

The first exciton transition is characterized by its energy and its oscillator strength $f_{ba,abs}$. To obtain the absorption oscillator strength, the spectrum of the absorbance (A) needs to be converted into the spectrum of the molar extinction coefficient ε. For this, the QD concentration c and the cuvette length L are needed (Beer's law: $\varepsilon = {}^{A}/_{cL}$). Hence, under the assumption that the concentration of PbSe QDs before exchange, which can be estimated from their absorption spectrum,[38] does not change during shell growth, the spectrum of ε can be readily obtained from the absorbance spectrum of a PbSe/CdSe QD suspension. Having the ε spectrum for PbSe/CdSe QDs with different shell-volume-to-

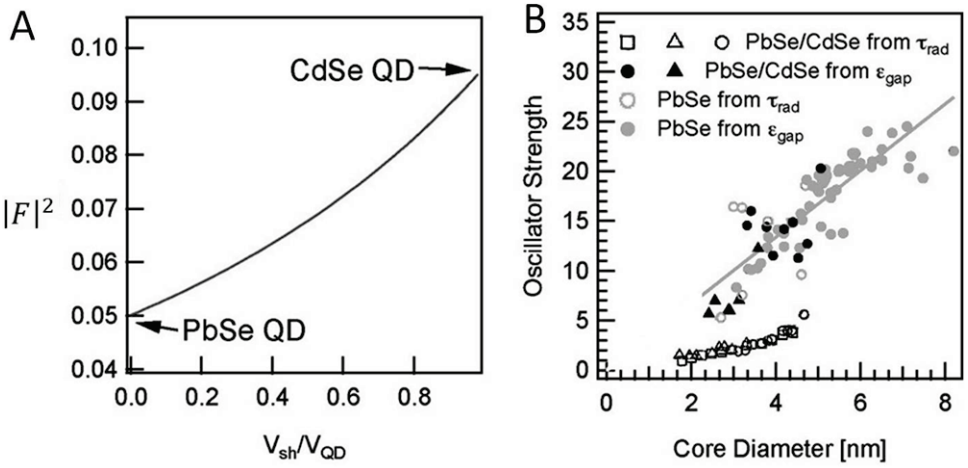

Fig. 2.7 (A) Local field factor at the band edge for PbSe/CdSe QDs as a function of the ratio V_{sh}/V_{QD}. (B) Absorption oscillator strength $f_{ba,abs}$ for PbSe QDs (full grey markers) and PbSe/CdSe QDs (full black markers) and emission oscillator strength $f_{ba,em}$ for PbSe QDs[39, 40] (empty grey markers) and PbSe/CdSe QDs (empty black markers) as a function of the core diameter. Shown are the values for PbSe/CdSe with a total diameter of (black squares) 6.1 nm, (black dots) 5.8 nm, and (black triangles) 4.6 nm. Modified from reference.[41]

total-QD-volume ratios (V_{sh}/V_{QD}), $f_{ba,abs}$ can be calculated from the energy-integrated molar extinction coefficient ε_{gap} of the first exciton transition, in analogy with calculations for PbSe[38] and PbS[42] QDs:

$$f_{ba,abs} = \frac{2\varepsilon_0 c m_e n_s}{\pi N_A \hbar e} \frac{1}{|F|^2} \ln(10)\, \varepsilon_{gap} \tag{2.1}$$

where ε_0 is the vacuum permittivity, c is the speed of light, $m_e$is the electron mass, n_s is the solvent refractive index (1.53 for tetrachloroetylene C_2Cl_4), NA is Avogadro's constant, $\hbar$ is Planck's constant, e is the unit charge, and F is the local field factor. Neeves *et al.* [43] provide the following expression for $|F|^2$ in the case of a core/shell particle:

$$|F|^2 = \left| \frac{9\varepsilon_{sh}\varepsilon_s}{\varepsilon_{sh}\varepsilon_a + 2\varepsilon_s\varepsilon_b} \right|^2 \tag{2.2}$$

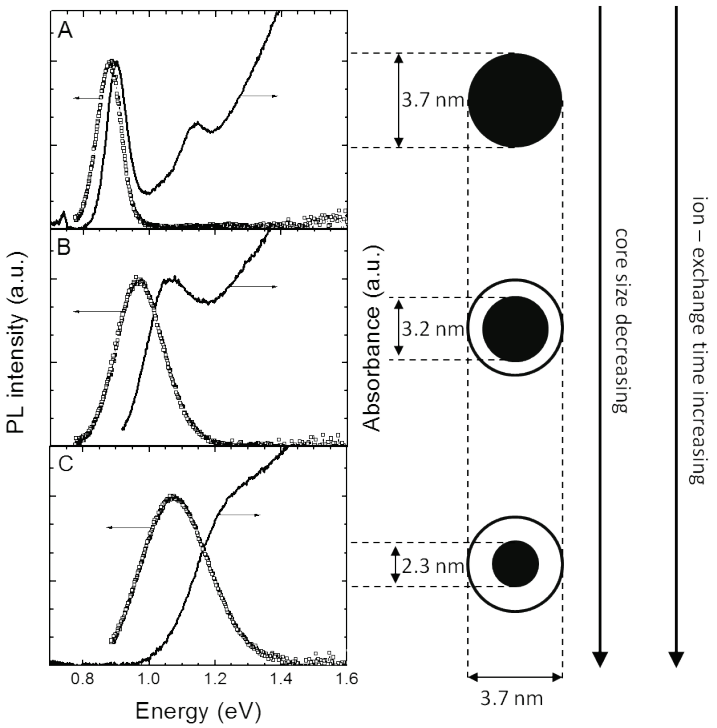

Fig. 2.8 Absorption and PL spectra of: (A) PbSe QDs; (B) PbSe/CdSe core/shell QDs after 5 min of ion-exchange time; (C) PbSe/CdSe core/shell QDs after 30 min of exchange. The total diameter of NCs is 3.7 nm.

with $$\varepsilon_a = \varepsilon_c\left(3 - 2\frac{V_{sh}}{V_{QD}}\right) + 2\varepsilon_{sh}\frac{V_{sh}}{V_{QD}}$$

$$\varepsilon_b = \varepsilon_c\frac{V_{sh}}{V_{QD}} + \varepsilon_{sh}\left(3 - \frac{V_{sh}}{V_{QD}}\right)$$

Using $\varepsilon_c = 25.7$ [44] and $\varepsilon_{sh} = 8.3$ [45] de Geyter *et al.* [41] found that $|F|^2$ gradually increases from the value for PbSe QDs to the value for CdSe QDs with increasing shell thickness (see Figure 2.7A). Due to the significant broadening of the first exciton peak at long reaction times, ε_{gap} is obtained by fitting the experimental ε absorption spectrum to a series of Gaussian functions with a polynomial background function and taking the area

under the lowest energy Gaussian function. The combination of $|F|^2$ with the values for ε_{gap} enables us to calculate $f_{ba,abs}$ of PbSe/CdSe QDs. Figure 2.7B shows that the dependence of $f_{ba,abs}$ on the diameter of the cores for PbSe/CdSe QDs is similar to that for the parent PbSe QDs. This correspondence confirms that the nature of the first absorption feature remains largely unchanged when adding a shell of CdSe.

Next to the absorption spectra, Fig. 2.8 shows the PL spectra for the parent PbSe QDs and two different suspensions of PbSe/CdSe QDs with total diameter of 3.7 nm. The parent PbSe QDs are characterized by a narrow absorption and emission peak width (FWHM of ~70 meV) and a small Stokes-shift (20 meV). With increasing ingrowth of the CdSe shell, both the first absorption and photoluminescence peak become broader, and the non-resonant Stokes-shift increases, reaching a value of 100, 175 and 250 meV for samples taken after 5, 30, 120 min of ion-exchange time, respectively. The results for the sample after 120 min of ion-exchange time are not shown in Fig. 2.8.

2.3.4 Photoluminescence Decay Curves and Emission Oscillator Strength

Figure 2.9 presents the photoluminescence decay curves for PbSe/CdSe NCs of 3.7 nm in diameter with an increasing shell thickness. The decay transients were acquired while monitoring the maximum of the PL peak. The decay curve of the parent PbSe QDs can be described by a single exponential function and it is considerably faster than that of the PbSe/CdSe QDs. From a single exponential fit to the decay curves of 3.7 nm PbSe QDs we obtain an experimental lifetime $\tau_0 = 1.18$ µs. This result agrees with the values reported by Kigel *et al.*[40] for 3.2 nm PbSe QDs dissolved in chloroform (*viz.*, 1.18 µs). In case of PbSe/CdSe core/shell nanocrystals, the decay curves can be fitted by a bi-exponential function, with a fast and a slow decay component. In general, the luminescence decay slows down for PbSe/CdSe core/shell nanocrystals with increasing thickness of the CdSe shell. A difference in the decay curves is already noticeable after 5 min of ion-exchange time. We remark that the lifetimes are in the µs range (comparable to those of PbSe nanocrystals), hence a factor thousand longer than for pure CdSe nanocrystals. After 120 minutes of ion-exchange time, the lifetime of the PbSe/CdSe core-shell heteronanocrystals does not increase anymore (Fig. 2.9A). The fast and the slow decay times for different samples are presented in Fig. 2.9B. It can be seen that the fast and slow components for PbSe/CdSe differ by about a factor of 4 from each other.

The increasing lifetimes of PbSe/CdSe QDs suggests a reduction of the oscillator strength. To obtain the emission oscillator strength for PbSe/CdSe core/shell QDs the radiative

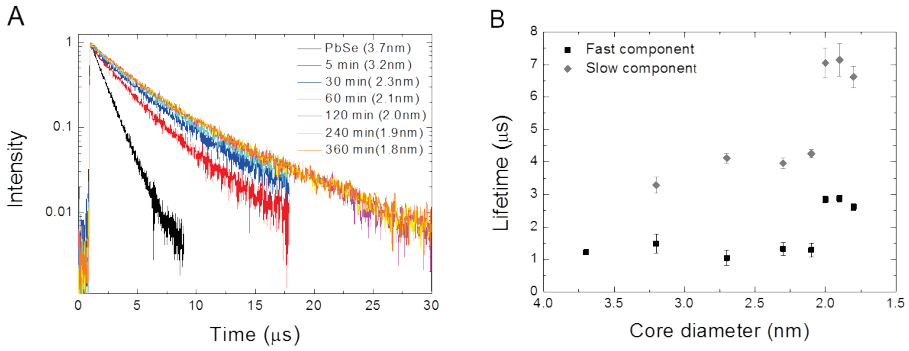

Fig. 2.9 (A) Photoluminescence decay curves of colloidal PbSe/CdSe QDs (3.7 nm) at room temperature for increasing shell thickness, (B) the evolution of the fast (black squares) and slow (grey diamonds) decay times obtained from a bi-exponential fit.

lifetime τ_{rad} has to be known. The experimentally measured lifetime τ_0 is related to the radiative lifetime as follows:

$$\tau_0 = (\tau_{rad}^{-1} + \tau_{nrad}^{-1})^{-1} = \tau_{rad} QY \tag{2.3}$$

Due to the lack of efficient and reliable infrared reference dyes, the quantum yield (QY) of PbSe and PbSe/CdSe QDs is hard to determine. However, we can compare the total emission intensity of oleic acid capped PbSe/CdSe QDs with the total emission intensity of oleic acid capped PbSe QDs,[46] making sure to normalize them relative to the absorbance at the excitation wavelength and keeping all settings of the spectrofluorometer the same. This enables a relative comparison of the QY of different samples, without knowing its exact value. Knowing the relative QY de Geyter *et al.* [41] rescaled the values of τ_0, to compare the lifetimes of different QD suspensions. The slow component of the bi-exponential fit of the PL decay curves was used for rescaling. Seven PbSe/CdSe QD samples with parent PbSe QD diameters of 6.1 nm, 5.8 nm and 4.6 nm were used, and each sample was probed at different wavelengths (Fig. 2.10).

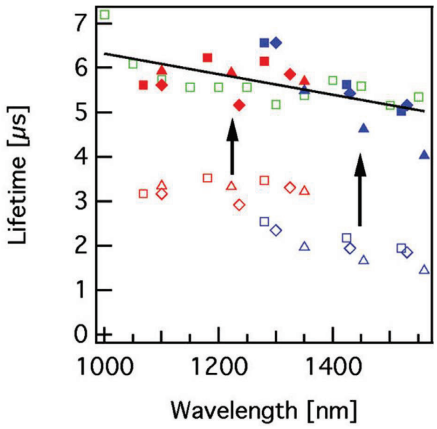

Fig. 2.10 Lifetime for seven samples of PbSe/CdSe QDs. Each sample is probed at different wavelengths (markers with equal color and symbol). Green squares have a parent PbSe QD diameter of 6.1 nm, blue markers have a parent PbSe QD diameter of 5.8 nm, and red markers have a parent QD diameter of 4.6 nm. Open symbols give the decay constant for the slow component obtained from a biexponential fit to experimental decay curves. Closed symbols give the fitted values rescaled according to the QY of each individual sample, taking the sample with open green squares as the standard. Reproduced from reference.[41]

The lifetimes differ significantly for different samples, ranging from 1.5 to 7 µs. The fact that PbSe/CdSe QDs from different suspensions, yet with comparable core diameters and shell thicknesses, yield strongly different lifetimes suggests that the experimental lifetime τ_0 depends on the QY of each sample. In Figure 2.10 the arrows illustrate the rescaling of the lifetime of each of the open red and open blue markers to the QY of the sample with open green squares which is taken as a standard. We note that these rescaled values, between 4 and 7 µs, are a lower limit of τ_{rad}. From Fig. 2.10, one can see that the lifetime decreases with increasing core diameter. Kigel et al.[40] measured a similar decreasing trend with the size of PbSe QD. For all wavelengths, the values are at least 4-6 times higher for PbSe/CdSe QDs than for PbSe QDs.

From the lower limit of the radiative lifetime obtained above for PbSe/CdSe QDs and literature values for PbSe QDs,[39, 40] we can calculate an upper limit of the oscillator strength $f_{ba,PbSe/CdSe,em}$ and $f_{ba,PbSe,em}$ of the emitting transition:

$$f_{ba,em} = \frac{2\pi\varepsilon_0 c^3 m_e}{e^2} \frac{g}{n_s |F|^2 \omega^2} \tau_{rad}^{-1} \tag{2.4}$$

where g is degeneracy of the state, and ω is the frequency of the transition.

The absorption oscillator strength is the sum of the transition strengths of all exciton states f_k,

$$f_{ba,abs} = \sum_{k=1}^{g} f_k \tag{2.5}$$

while the emission oscillator strength is a Boltzmann weighted average of the transition strength of each exciton state taking into account possible splitting between the states:[47]

$$f_{ba,em} = g \frac{\sum_{k=1}^{g} f_k \, e^{-\Delta E_k / kT}}{\sum_{k=1}^{g} e^{-\Delta E_k / kT}} \tag{2.6}$$

Effectively, this yields the average transition strength of the states that contribute to the emission. Since emission comes from radiative decay of a single exciton, which occupies only one of all possible ground exciton states, and absorption involves all exciton states, we include in eq (2.6) the total number of exciton states g = 64 to obtain a total emission oscillator strength. This is equivalent to compressing the fine structure to one single emitting state with degeneracy g and oscillator strength $f_{ba,em}$.

The resulting values for $f_{ba,PbSe/CdSe,em}$ and $f_{ba,PbSe,em}$ are represented by the open markers in red and blue, respectively, in Fig. 2.7B. The values for $f_{ba,PbSe,em}$ are similar to the values obtained from the absorption spectrum $f_{ba,PbSe,abs}$. In contrast, the emission oscillator strengths $f_{ba,PbSe/CdSe,em}$ for PbSe/CdSe core/shell QDs are at least 75% smaller than the values for PbSe QDs.

2.3.5 Probing the Carrier Localization Regimes

The quantitative analysis of the absorption and luminescence data yields contradictory outcomes. While the energy and the absorption oscillator strength of the band gap transition in PbSe/CdSe core/shell QDs are indicative of a type-I localization regime, the sensitivity of the emission QY and the increase in exciton lifetime associated with a decrease in emission oscillator strength suggest that one of the carriers is delocalized over the entire QD (type-$I^{1/2}$) or even localized in the CdSe shell (type-II). To probe the localization regime, we added hexanethiol, a well-known hole scavenger for CdSe[48] and PbSe[49, 50] and methyl viologen (MV^{2+}), an electron scavenger,[51, 52] to PbSe/CdSe QD suspensions and analyzed their effect on the photoluminescence.

Adding hexanethiol (150 μM) to a PbSe/CdSe core/shell QDs suspension does not substantially quench the photoluminescence (see Fig. 2.11). The small decrease observed in the emission intensity is probably due to slight clustering of particles. The maximum of the PL peak is slightly redshifted (by 0.02eV) indicating that hexanethiol binds to the NC surface.[53] In contrast, the addition of hexanethiol to a PbSe QD sample resulted in significant quenching of the PL (not shown). Methyl viologen dichloride was dissolved in isopropyl alcohol (IPA) and the MV^{2+}/IPA mixture was added in a 1:33 (v/v) ratio to obtain a 150 μM MV^{2+} concentration. As a reference, we added the same amount of pure IPA to an identical QD sample, which resulted in a 50% drop of the QY. Adding the MV^{2+} mixture however immediately quenches the PL signal to values below the detection limit (Fig. 2.12). The same result was obtained for a PbSe QD reference sample. This shows that PbSe/CdSe QDs emit from a state in which the electron wave function reaches the surface and the hole wave function is well confined to the core. This confirms that PbSe/CdSe core/shell QDs are in the Type-$I^{1/2}$ localization regime. The delocalization of the electron will reduce the wave function overlap to some extent. However, these measurements are not sufficient to conclude that this reduction in overlap fully accounts for the reduction in emission oscillator strength. In addition, they do not explain why the absorption oscillator strength remains essentially unchanged.

To define the localization regimes in PbSe/CdSe core/shell QDs, effective mass modeling, was carried out by de Geyter *et al.* [41] The modeling was based on the bulk band alignment and effective masses of PbSe and CdSe.[54-56] According to literature [57] bulk PbSe and CdSe have a type-I band alignment with a valence band offset of 0.78 eV and conduction band offset of 0.70 eV. Using the effective masses of PbSe and CdSe the wave function of a PbSe/CdSe QD with a core radius of 1.5 nm and a shell thickness of 1 nm was modeled. [41] Due to the difference in effective mass between electron and hole in CdSe, it was found that the electron wave function spreads throughout the entire QD, while the hole wave function is confined to the PbSe core. The overlap integral was found to have a value between 1 (for large band offsets) and 0.8 (when the band offset equals zero).[41] Since the overlap integral is directly proportional to the oscillator strength, this confirms the experimental result that $f_{ba,PbSe/CdSe,abs}$ does not significantly differ from $f_{ba,PbSe,abs}$.

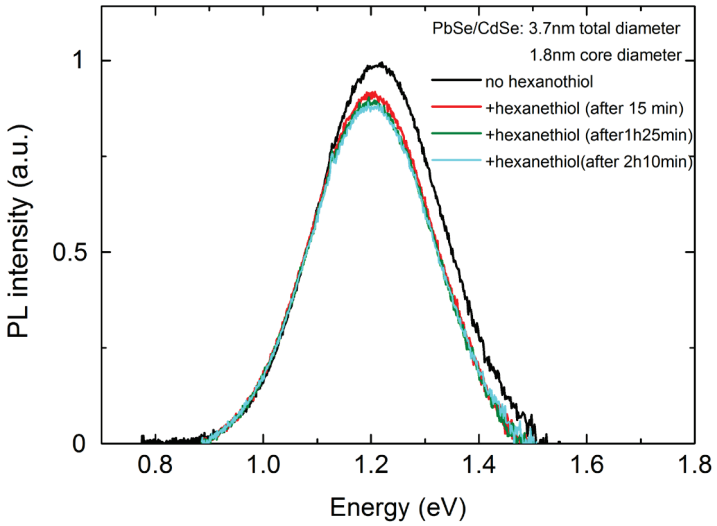

Fig. 2.11 Photoluminescence spectra of PbSe/CdSe core/shell QDs before and after adding hexanethiol.

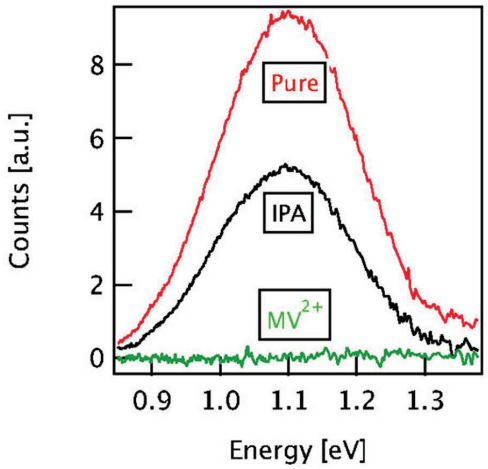

Fig. 2.12 Photoluminescence spectra of PbSe/CdSe core/shell QDs before and after adding IPA and MV^{2+}/IPA. Reproduced from reference. [41]

Even though there is only a small reduction in overlap, the electron wave function does have a nonzero value at the QD outer surface, while the hole wave function is negligible at the QD outer surface. This is confirmed by the PL quenching experiments, which show that the electron is transferred to the electron acceptor at the surface, while the hole does not transfer to the hole acceptor.

The effective mass model cannot explain why $f_{ba,PbSe/CdSe,em}$ is reduced. The fact that the QY of PbSe/CdSe QDs is comparable to and often higher than that of PbSe QDs and the clear dependence of $f_{ba,PbSe/CdSe,em}$ on the QD diameter indicate that this is most likely an intrinsic PbSe/CdSe QD property, and not an artifact due to surface state mediated radiative recombination. Therefore, it suggests that the fine structure of PbSe/CdSe QDs, is more complex. Looking at eq 2.5 and eq 2.6, $f_{ba,abs}$ and $f_{ba,em}$ will only differ significantly when (a) the energy splitting is much larger than the thermal energy kT and (b) the emitting states have a much lower oscillator strength than the absorbing states. Therefore, the band edge emission in PbSe/CdSe QDs comes from states that are fundamentally different from the bright absorbing states.

2.3.6 Stokes Shift

A splitting of the band edge in a lower energy dark and higher energy bright state due to the exchange interaction was predicted for PbSe QDs by An et al.[47] This so-called exchange splitting however is only between 0 and 20 meV. Hence, at room-temperature these states are both populated due to thermal excitation, resulting in similar values for $f_{ba,PbSe,abs}$ and $f_{ba,PbSe,em}$. According to An et al.,[47] the exchange splitting, together with the intervalley splitting, explains the nonresonant Stokes shift in PbSe QDs. Figure 2.13 shows the non resonant Stokes shift of PbSe QDs (light grey squares) and PbSe/CdSe QDs (red dots) as a function of the absorption energy or core size. Our values for PbSe QDs extrapolate well to the theoretical values reported for small QDs. [37, 47, 58]

Like the band gap energy, the PbSe/CdSe QD Stokes shift depends only on the core size, but it exceeds that for PbSe QDs by 50-100 meV. For small cores, it reaches a value of 200 meV. Since the total volume and total size dispersion remain constant for these QDs throughout the exchange procedure,[27] we expect an increase in the Stokes shift due to nonuniform excitation of maximum 10 meV for the most broadened sample. The large Stokes shift is therefore not an artifact of size broadening, but due to an intrinsic physical effect. Increased splitting in the fine structure according to Boltzmann statistics result in an increased Stokes shift. Hence, it confirms that the band edge emission results mostly from lower energy states with reduced oscillator strength as compared to the higher energy

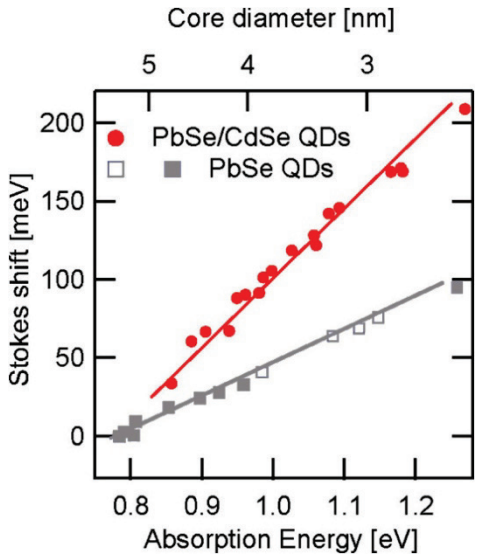

Fig. 2.13 Stokes shift for PbSe QDs (full and open light grey squares)[40] and PbSe/CdSe core/shell QDs (red circles) as a function of absorption energy. Reproduced from reference.[41]

absorbing states. This fine structure cannot be understood without extensive modeling. The nature of the interface, both in the real and in the reciprocal lattice (the band edge states are around the L-point for PbSe and the Γ-point for CdSe) probably has a strong influence on the electronic properties of these heterostructures. The $1S_e1S_h$ excitons fine-structure will be discussed in more detail in Chapter 3.

2.4 Conclusion

In this chapter the synthesis of PbSe/CdSe core/shell QDs was presented. The ion-exchange process leads to the ingrowth of a CdSe shell of increasing thickness with the simultaneous shrinking of the remaining PbSe core. The ion-exchange proceeds very fast at the beginning and seems to slow down with increasing exchange time. HR-TEM and HAADF-STEM studies show that the PbSe core has an octahedral like shape with eight Se(111) interfacial planes shared with the CdSe shell. The CdSe shell is observed to have non-uniform thickness. Decreasing of the PbSe core diameter leads to shift of the absorption and emission peak positions to higher energies. Moreover, the absorption and emission peaks

become broader. This peak broadening can be due to inhomogeneity of size and shape of the QDs and to increasing of the spatially indirect character of the exciton. The exciton lifetime increases considerably during the ion-exchange process. This suggests that the overlap between electron and hole wavefunctions decreases with increasing CdSe shell thickness and decreasing PbSe core diameter. We show that both the energy and the oscillator strength of the first absorption peak in PbSe/CdSe quantum dots follow the same trend with core diameter as those of PbSe QDs. On the other hand, PL lifetime measurements yield an oscillator strength in emission that is reduced by at least 75%, compared to the PbSe/CdSe oscillator strength from absorption and the PbSe QD oscillator strength in absorption and emission. Moreover, the addition of an electron scavenger leads to a complete quenching of the PbSe/CdSe QD PL, while a hole scavenger does not. These results can be rationalized by an effective mass model that depicts a PbSe/CdSe QD as a quantum confined heterostructure at the boundary between a type-I and a quasi-type-II (type $I^{1/2}$) localization regime. They show that the absorbing states essentially remain unchanged by the addition of a CdSe shell. However, this model does not explain the reduction of the oscillator strength of the band gap emission. In combination with the significantly increased Stokes shift, we conclude that the band gap emission in PbSe/CdSe QDs comes from fundamentally different states with lower oscillator strength that are energetically well separated from the absorbing states at room temperature. Moreover, these emitting states are different than the emitting states in PbSe QDs.

References

1. de Mello Donegá, C., *Formation of nanoscale spatially indirect excitons: Evolution of the type-II optical character of CdTe/CdSe heteronanocrystals.* Physical Review B, 2010. **81**(16): p. 165303.
2. Chin, P.T.K., de Mello Donegá, C., van Bavel, S.S., Meskers, S.C.J., Sommerdijk, N.A.J.M., and Janssen, R.A.J., *Highly Luminescent CdTe/CdSe Colloidal Heteronanocrystals with Temperature-Dependent Emission Color.* Journal of the American Chemical Society, 2007. **129**(48): p. 14880-14886.
3. Li, J.J., Tsay, J.M., Michalet, X. and Weiss, S. , *Wavefunction engineering: From quantum wells to near-infrared type II colloidal quantum dots synthesized by layer-by-layer colloidal epitaxy.* Chemical Physics, 2005(318): p. 82-90.
4. Kim, S., Fisher, B., Eisler, H.-J., and Bawendi, M., *Type-II Quantum Dots: CdTe/CdSe(Core/Shell) and CdSe/ZnTe(Core/Shell) Heterostructures.* Journal of the American Chemical Society, 2003. **125**(38): p. 11466-11467.
5. van Sark, W.G.J.H.M., Frederix, P.L.T.M., van den Heuvel, D.J., Bol, A.A., van Lingen, J.N.J., de Mello Donegá, C., Gerritsen, H.C., and Meijerink, A., *Time-Resolved Fluorescence Spectroscopy Study on the Photophysical Behavior of Quantum Dots.* Journal of Fluorescence, 2002. **12**(1): p. 69-76.
6. van Sark, W.G.J.H.M., Frederix, P.L.T.M., Van den Heuvel, D.J., Gerritsen, H.C., Bol, A.A., van Lingen, J.N.J., de Mello Donega, C., and Meijerink, A., *Photooxidation and*

Photobleaching of Single CdSe/ZnS Quantum Dots Probed by Room-Temperature Time-Resolved Spectroscopy. The Journal of Physical Chemistry B, 2001. **105**(35): p. 8281-8284.

7. Talapin, D.V., Rogach, A.L., Kornowski, A., Haase, M., and Weller, H., *Highly Luminescent Monodisperse CdSe and CdSe/ZnS Nanocrystals Synthesized in a Hexadecylamine-Trioctylphosphine Oxide-Trioctylphospine Mixture.* Nano Letters, 2001. **1**(4): p. 207-211.
8. Pan, D., Wang, Q., Jiang, S., Ji, X., and An, L., *Synthesis of Extremely Small CdSe and Highly Luminescent CdSe/CdS Core-Shell Nanocrystals via a Novel Two-Phase Thermal Approach.* Advanced Materials, 2005. **17**(2): p. 176-179.
9. Li, J. and Wang, L.-W., *First principle study of core/shell structure quantum dots.* Applied Physics Letters, 2004. **84**(18): p. 3648-3650.
10. Li, J.J., Wang, Y.A., Guo, W., Keay, J.C., Mishima, T.D., Johnson, M.B., and Peng, X., *Large-Scale Synthesis of Nearly Monodisperse CdSe/CdS Core/Shell Nanocrystals Using Air-Stable Reagents via Successive Ion Layer Adsorption and Reaction.* Journal of the American Chemical Society, 2003. **125**(41): p. 12567-12575.
11. Peng, X., Schlamp, M.C., Kadavanich, A.V., and Alivisatos, A.P., *Epitaxial Growth of Highly Luminescent CdSe/CdS Core/Shell Nanocrystals with Photostability and Electronic Accessibility.* Journal of the American Chemical Society, 1997. **119**(30): p. 7019-7029.
12. Zhong, X., Xie, R., Zhang, Y., Basche, T., and Knoll, W., *High-Quality Violet- to Red-Emitting ZnSe/CdSe Core/Shell Nanocrystals.* Chemistry of Materials, 2005. **17**(16): p. 4038-4042.
13. Reiss, P., Bleuse, J., and Pron, A., *Highly Luminescent CdSe/ZnSe Core/Shell Nanocrystals of Low Size Dispersion.* Nano Letters, 2002. **2**(7): p. 781-784.
14. Wise, F.W., *Lead Salt Quantum Dots: the Limit of Strong Quantum Confinement.* Accounts of Chemical Research, 2000. **33**(11): p. 773-780.
15. Sashchiuk, A., Amirav, L., Bashouti, M., Krueger, M., Sivan, U., and Lifshitz, E., *PbSe Nanocrystal Assemblies: Synthesis and Structural, Optical, and Electrical Characterization.* Nano Letters, 2003. **4**(1): p. 159-165.
16. Murray, C.B., Sun, S.H., Gaschler, W.,Doyle, H., Batley, T.A., and Kagan, C.R., *Colloidal synthesis of nanocrystal superlattices.* IBM J. Res. Dev., 2001. **45**(1): p. 47-56.
17. Gaponenko, S.V., *Optical Properties of Semiconductor Nanocrystals*. Cambrige U.K. 1998: Cambridge University Press.
18. Oda, O., *Compound Semiconductor Bulk Materials and Characterizations* 2007: World Scientific Publishing Co. Pte. Ltd. 371.
19. Fu, A., Gu, W., Boussert, B., Koski, K., Gerion, D., Manna, L., Le Gros, M., Larabell, C.A., and Alivisatos, A.P., *Semiconductor Quantum Rods as Single Molecule Fluorescent Biological Labels.* Nano Letters, 2007. **7**(1): p. 179-182.
20. Bruchez, M., Jr., Moronne, M., Gin, P., Weiss, S., and Alivisatos, A.P., *Semiconductor Nanocrystals as Fluorescent Biological Labels.* Science, 1998. **281**(5385): p. 2013-2016.
21. Chan, Y., Caruge, J.-M., Snee, P.T., and Bawendi, M.G., *Multiexcitonic two-state lasing in a CdSe nanocrystal laser.* Applied Physics Letters, 2004. **85**(13): p. 2460-2462.
22. Sholin, V., Breeze, A.J., Anderson, I.E., Sahoo, Y., Reddy, D., and Carter, S.A., *All-inorganic CdSe/PbSe nanoparticle solar cells.* Solar Energy Materials and Solar Cells, 2008. **92**(12): p. 1706-1711.
23. Lee, Y.-L., Huang, B.-M., and Chien, H.-T., *Highly Efficient CdSe-Sensitized TiO2 Photoelectrode for Quantum-Dot-Sensitized Solar Cell Applications.* Chemistry of Materials, 2008. **20**(22): p. 6903-6905.
24. Springholz, G. and Bauer, G., *Molecular beam epitaxy of IV-VI semiconductor hetero- and nano-structures.* physica status solidi (b), 2007. **244**(8): p. 2752-2767.

25. Cozzoli, P.D., Pellegrino, T., and Manna, L., *Synthesis, properties and perspectives of hybrid nanocrystal structures.* Chemical Society Reviews, 2006. **35**(11): p. 1195-1208.
26. Yin, Y. and Alivisatos, A.P., *Colloidal nanocrystal synthesis and the organic-inorganic interface.* Nature, 2005. **437**(7059): p. 664-670.
27. Pietryga, J.M., Werder, D.J., Williams, D.J., Casson, J.L., Schaller, R.D., and Klimov, V.I., *Utilizing the Lability of Lead Selenide to Produce Heterostructured Nanocrystals with Bright, Stable Infrared Emission.* Journal of the American Chemical Society, 2008. **130**(14): p. 4879-4885.
28. Lambert, K., Geyter, B.D., Moreels, I., and Hens, Z., *PbTe|CdTe Core|Shell Particles by Cation Exchange, a HR-TEM study.* Chemistry of Materials, 2009. **21**(5): p. 778-780.
29. Heiss, W., Kaufmann, E., Böberl, M., Schwarzl, T., Springholz, G., Hesser, G., Schäffler, F., Koike, K., Harada, H., Yano, M., Leitsmann, R., Ramos, L.E., and Bechstedt, F., *Highly luminescent nanocrystal quantum dots fabricated by lattice-type mismatched epitaxy.* Physica E: Low-dimensional Systems and Nanostructures, 2006. **35**(2): p. 241-245.
30. Houtepen, A.J., Koole, R., Vanmaekelbergh, D., Meeldijk, J., and Hickey, S.G., *The Hidden Role of Acetate in the PbSe Nanocrystal Synthesis.* Journal of the American Chemical Society, 2006. **128**(21): p. 6792-6793.
31. Beaunier, L., Cachet, H., Cortès, R., and Froment, M., *Electrodeposition of PbSe epitaxial films on (111) InP.* Electrochemistry Communications, 2000. **2**(7): p. 508-510.
32. Bals, S., Casavola, M., van Huis, M.A., Van Aert, S., Batenburg, K.J., Van Tendeloo, G., and Vanmaekelbergh, D., *Three-Dimensional Atomic Imaging of Colloidal Core/Shell Nanocrystals.* Nano Letters, 2011. **11**(8): p. 3420-3424.
33. Casavola, M., van Huis, M.A., Bals, S., Lambert, K., Hens, Z., and Vanmaekelbergh, D., *Anisotropic Cation Exchange in PbSe/CdSe Core/Shell Nanocrystals of Different Geometry.* Chemistry of Materials, 2012. **24**(2): p. 294-302.
34. Liljeroth, P., van Emmichoven, P.A.Z., Hickey, S.G., Weller, H., Grandidier, B., Allan, G., and Vanmaekelbergh, D., *Density of States Measured by Scanning-Tunneling Spectroscopy Sheds New Light on the Optical Transitions in PbSe Nanocrystals.* Physical Review Letters, 2005. **95**(8): p. 086801.
35. Kang, I. and Wise, F.W., *Electronic structure and optical properties of PbS and PbSe quantum dots.* J. Opt. Soc. Am. B, 1997. **14**(7): p. 1632-1646.
36. Du, H., Chen, C., Krishnan, R., Krauss, T.D., Harbold, J.M., Wise, F.W., Thomas, M.G., and Silcox, J., *Optical Properties of Colloidal PbSe Nanocrystals.* Nano Letters, 2002. **2**(11): p. 1321-1324.
37. Franceschetti, A., *Structural and electronic properties of PbSe nanocrystals from first principles.* Physical Review B, 2008. **78**(7): p. 6.
38. Moreels, I., Lambert, K., De Muynck, D., Vanhaecke, F., Poelman, D., Martins, J.C., Allan, G., and Hens, Z., *Composition and Size-Dependent Extinction Coefficient of Colloidal PbSe Quantum Dots.* Chemistry of Materials, 2007. **19**(25): p. 6101-6106.
39. Schaller, R.D., Crooker, S.A., Bussian, D.A., Pietryga, J.M., Joo, J., and Klimov, V.I., *Revealing the Exciton Fine Structure of PbSe Nanocrystal Quantum Dots Using Optical Spectroscopy in High Magnetic Fields.* Physical Review Letters, 2010. **105**(6): p. 067403.
40. Kigel, A., Brumer, M., Maikov, G.I., Sashchiuk, A., and Lifshitz, E., *Thermally Activated Photoluminescence in Lead Selenide Colloidal Quantum Dots.* Small, 2009. **5**(14): p. 1675-1681.
41. De Geyter, B., Justo, Y., Moreels, I., Lambert, K., Smet, P.F., Van Thourhout, D., Houtepen, A.J., Grodzińska, D., de Mello Donega, C., Meijerink, A., Vanmaekelbergh, D., and Hens, Z., *The Different Nature of Band Edge Absorption and Emission in Colloidal PbSe/CdSe Core/Shell Quantum Dots.* ACS Nano, 2011. **5**(1): p. 58-66.

42. Moreels, I., Lambert, K., Smeets, D., De Muynck, D., Nollet, T., Martins, J.C., Vanhaecke, F., Vantomme, A., Delerue, C., Allan, G., and Hens, Z., *Size-Dependent Optical Properties of Colloidal PbS Quantum Dots.* ACS Nano, 2009. **3**(10): p. 3023-3030.
43. Neeves, A.E. and Birnboim, M.H., *Composite Structures for the Enhancement of Nonlinear-Optical Susceptibility.* Journal of the Optical Society of America B-Optical Physics, 1989. **6**(4): p. 787-796.
44. Suzuki, N., Sawai, K., and Adachi, S., *Optical properties of PbSe.* Journal of Applied Physics, 1995. **77**(3): p. 1249-1255.
45. Ninomiya, S. and Adachi, S., *Optical properties of cubic and hexagonal CdSe.* Journal of Applied Physics, 1995. **78**(7): p. 4681-4689.
46. Moreels, I., Fritzinger, B., Martins, J.C., and Hens, Z., *Surface Chemistry of Colloidal PbSe Nanocrystals.* Journal of the American Chemical Society, 2008. **130**(45): p. 15081-15086.
47. An, J.M., Franceschetti, A., and Zunger, A., *The Excitonic Exchange Splitting and Radiative Lifetime in PbSe Quantum Dots.* Nano Letters, 2007. **7**(7): p. 2129-2135.
48. Wuister, S.F., de Mello Donega, C., and Meijerink, A., *Influence of Thiol Capping on the Exciton Luminescence and Decay Kinetics of CdTe and CdSe Quantum Dots.* The Journal of Physical Chemistry B, 2004. **108**(45): p. 17393-17397.
49. Wang, C., Kwon, K.-W., Odlyzko, M.L., Lee, B.H., and Shim, M., *PbSe Nanocrystal/TiOx Heterostructured Films: A Simple Route to Nanoscale Heterointerfaces and Photocatalysis.* The Journal of Physical Chemistry C, 2007. **111**(31): p. 11734-11741.
50. Luther, J.M., Law, M., Song, Q., Perkins, C.L., Beard, M.C., and Nozik, A.J., *Structural, Optical, and Electrical Properties of Self-Assembled Films of PbSe Nanocrystals Treated with 1,2-Ethanedithiol.* ACS Nano, 2008. **2**(2): p. 271-280.
51. Burda, C., Green, T.C., Link, S., and El-Sayed, M.A., *Electron Shuttling Across the Interface of CdSe Nanoparticles Monitored by Femtosecond Laser Spectroscopy.* The Journal of Physical Chemistry B, 1999. **103**(11): p. 1783-1788.
52. Matylitsky, V.V., Dworak, L., Breus, V.V., Baschei□, T., and Wachtveitl, J., *Ultrafast Charge Separation in Multiexcited CdSe Quantum Dots Mediated by Adsorbed Electron Acceptors.* Journal of the American Chemical Society, 2009. **131**(7): p. 2424-2425.
53. Koole, R., Luigjes, B., Tachiya, M., Pool, R., Vlugt, T.J.H., de Mello Donega, C., Meijerink, A., and Vanmaekelbergh, D., *Differences in Cross-Link Chemistry between Rigid and Flexible Dithiol Molecules Revealed by Optical Studies of CdTe Quantum Dots.* The Journal of Physical Chemistry C, 2007. **111**(30): p. 11208-11215.
54. Martinez, G., Schlüter, M., and Cohen, M.L., *Electronic structure of PbSe and PbTe. Band structures, densities of states, and effective masses.* Physical Review B, 1975. **11**(2): p. 651.
55. Dalven, R., *Calculation of effective masses in cubic CdS and CdSe.* physica status solidi (b), 1971. **48**(1): p. K23-K26.
56. Dimmock, J.O. and Wheeler, R.G., *Exciton Structure and Zeeman Effects in Cadmium Selenide.* Journal of Applied Physics, 1961. **32**(10): p. 2271-2277.
57. Michaelson, H.B., *Relation Between an Atomic Electronegativity Scale and the Work Function.* IBM J. Res. Dev., 1978. **22**: p. 72-80.
58. Leitsmann, R. and Bechstedt, F., *Characteristic Energies and Shifts in Optical Spectra of Colloidal IV-VI Semiconductor Nanocrystals.* ACS Nano, 2009. **3**(11): p. 3505-3512.

3

Two-Fold Emission from the S-Shell of Colloidal PbSe/CdSe Core/Shell Quantum Dots

In this chapter the optical properties of PbSe/CdSe core/shell quantum dots with core sizes smaller than 4 nm in the 5–300 K range are reported. The photoluminescence spectra show two peaks, which become increasingly separated in energy as the core diameter is reduced below 4 nm. It is shown that these peaks are due to intrinsic exciton transitions in each quantum dot, rather than emission from different quantum dot sub-ensembles. Most likely, the energy separation between the peaks is due to inter-valley coupling between the L-points of PbSe. The temperature dependence of the relative intensities of the peaks implies that the two emitting states are not in thermal equilibrium and that dark exciton states must play an important role.

3.1 Introduction

Nanocrystalline quantum dots (QDs) of Pb-chalcogenides have attracted increasing interest in recent years since these systems hold promise for optoelectronic applications in the near- and mid-IR (photodetectors, LEDs, photonic switches, and photovoltaic cells).[1-3] Two routes have been developed for the fabrication of Pb-chalcogenide nanocrystals (NCs): vapour-phase epitaxial deposition methods, which result in QDs embedded in a solid matrix, and wet chemical synthesis, which yields colloidal suspensions of organically capped NCs. For instance, PbTe QDs embedded in a coherent CdTe matrix have been grown by molecular beam epitaxy and annealing.[4] Colloidal PbTe QDs are also available, and recently well-defined PbTe/CdTe core/shell colloidal QD systems have been reported.[5] Colloidal core/shell QDs and hetero-NCs with other geometries are of particular interest, since the ability to join different materials in one particle opens up new possibilities for property engineering.[6] Furthermore, superlattices consisting of self-assembled colloidal PbSe NCs hold promise for photovoltaic applications and photon detection in the near-IR, as well as for transistor type devices.[2, 7-10]

The effective masses of the electron and hole in Lead chalcogenides are small, leading to large exciton Bohr radii (*e.g.*, 46 nm for PbSe).[10, 11] This results in strong quantum confinement for relatively large NCs, making it possible to tune the optical properties of Pb-chalcogenide NCs over a wide spectral range by controlling their size. For example, the band gap of PbSe QDs can be tuned from the bulk value (0.3 eV) up to about 1.5 eV by decreasing the NC diameter in the 100 to 2 nm range.[12] The electronic (fine) structure of Pb-chalcogenide QDs is complex, and there are still several unresolved issues. These materials crystallize in the rock-salt structure and have an electronic band structure that differs considerably from that of typical II-VI compounds. The maximum of the valence band and the minimum of the conduction band are both situated at the L-point in the Brillouin zone (Figure 3.1). Since there are four L-points *per* fcc Brillouin zone, the fundamental band gap is eight-fold degenerate if spin degeneracy is included. This yields a 64-fold degenerate lowest exciton state ($1S_h - 1S_e$). This degeneracy is partially lifted by a number of effects (*viz*., intraband and inter-valley couplings and electron-hole exchange), leading to an exciton fine structure that is not yet completely investigated. In the case of PbSe QDs, tight binding,[13] pseudo-potential,[14] and first principle calculations[15, 16] have been used to reveal the impact of valence-to-conduction band coupling and coupling between the 4 L-points (*i.e.*, inter-valley coupling) on the electronic structure in the strong quantum confinement regime. Electron-hole exchange is also important, and, in combination with the coupling effects, leads to an intricate exciton fine structure consisting of a number of bright and dark states. These effects depend critically on the size and shape of the PbSe NC, and possibly also on the surface termination, which makes it difficult to

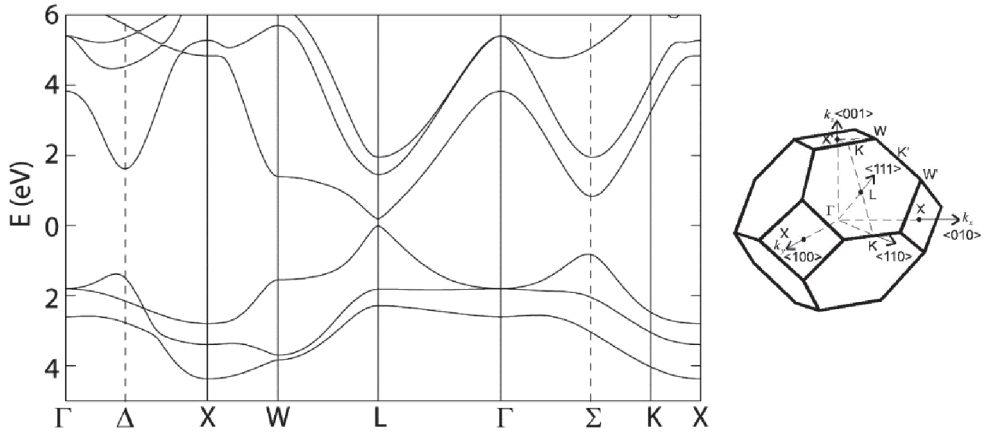

Fig. 3.1 Band structure (left) of bulk PbSe. The zero of energy is located at the top of the valence band.[13] The first Brillouin zone for a fcc lattice is also shown (right).

obtain a comprehensive experimental and theoretical picture of the exciton fine structure in PbSe NCs, and in Pb-chalcogenide NCs in general. Further experimental investigations of the electronic (fine) structure of well-defined PbSe QDs is therefore highly desirable, particularly for diameters below 4 nm.

Here, we report a comprehensive study of the (time-resolved) photoluminescence (PL) of small (< 4 nm) PbSe NCs in a PbSe/CdSe core/shell colloidal QD system over a broad temperature range (5 – 300 K). The samples investigated in this work consist of diluted colloidal suspensions (10^{-7} mol/L), and therefore Förster energy transfer and other forms of interaction between the QDs can be neglected. We have used a recently reported Pb for Cd ion-exchange reaction to convert small PbSe NCs (~4 nm diameter) into PbSe/CdSe core/shell hetero-NCs.[17] Three different batches of parent PbSe NCs, with average diameters of 3.7, 4.0 and 4.2 nm, were used. The overall size and shape of the NC remain unchanged upon ion-exchange, hence the duration of the ion-exchange reaction defines the thickness of the CdSe shell and the size of the remaining PbSe core. This allows the study of increasingly smaller PbSe NCs that are chemically and photochemically stable and have a well-defined PbSe/CdSe interface. The PbSe rock-salt and the CdSe wurtzite or zinc-blende lattices do not alloy but have a commensurate Se sub-lattice. Therefore, the PbSe/CdSe hetero-interface consists of Se {111} planes that are nearly strain free.[18] The PL of the PbSe/CdSe core/shell colloidal QDs investigated in this work is strong and decreases gradually in intensity from 5 K to room temperature. Strikingly, the PL spectra consist of two peaks, with a separation that increases with decreasing volume of the PbSe

cores. A similar behaviour is observed for PbSe colloidal QDs. These two emission peaks are ascribed to two bright exciton fine-structure states in the 64-manifold of the $1S_h - 1S_e$ state of PbSe QDs. These two emitting states are also reflected in the excitation spectra. The splitting between the states is most likely due to inter-valley coupling and electron-hole exchange. Intriguingly, the two states are not in thermal equilibrium.

3.2 Experimental Section

The colloidal PbSe/CdSe core/shell QDs investigated in this work were synthesized in two steps. First, oleic acid capped PbSe NCs were grown following the method developed by Houtepen and co-workers.[19] Subsequently, the PbSe QDs were converted into PbSe/CdSe core/shell hetero-NCs by using a Pb for Cd ion-exchange method.[17, 20] The syntheses were carried out under inert atmosphere conditions. Three different batches of PbSe QDs, with average diameters of 3.7, 4.0 and 4.2 nm (10% size dispersion), were used as parent NCs. The diameter of the parent PbSe QDs was determined by transmission electron microscopy, while the core diameter of PbSe/CdSe core/shell QDs was estimated from the spectral position of the lowest energy absorption peak using an empirical sizing curve,[12] under the assumption that this transition involves states that are primarily localized in the PbSe core. The validity of this assumption has been demonstrated by recent studies correlating the optically estimated core size with those determined by TEM analysis.[21] High-resolution Transmission Electron Microscopy measurements were performed using an aberration-corrected Titan microscope operating at 300 kV. Absorption spectra were measured using a Perkin-Elmer Lambda 950 UV/VIS/IR absorption spectrophotometer. PL spectra and PL excitation spectra were recorded using an Edinburgh Instruments FLS920 spectrofluorometer. For the PL excitation spectra a Halogen lamp was used as the excitation source. PL decay time measurements were performed by using an excimer laser pumped tunable dye laser (Lambda Physik LPX 100 and LPD3000) as the pulsed excitation source (20 ns pulses at 10 Hz repetition rate) and the spectrofluorometer described above to detect the emission. The dye Coumarin 102 was used and the wavelength of 500 nm was selected. Decay curves were obtained using a Tektronix 2430 digital oscilloscope (500 MHz), interfaced with a PC.

3.3. Results and Discussion

3.3.1 General characterization and room temperature optical spectra

Low resolution transmission electron microscopy (TEM) images of PbSe QDs before (Fig. 3.2A) and after (Fig. 3.2C) the Pb for Cd ion-exchange reaction are shown in Figure 3.2. A schematic representation of the cation-exchange process is also presented (Fig. 3.2B). Prior to ion-exchange the parent PbSe QDs have a multifaceted nearly spherical shape with a diameter of 3.7 nm (10% standard deviation). Batches of PbSe QDs with 4.0 nm and 4.2 nm diameter were also used as parent NCs and lead to similar results. The ion-exchange reaction leads to the formation of PbSe/CdSe core/shell QDs in which the PbSe cores progressively shrink as the CdSe shell grows. As a result, the PbSe core diameter decreases with increasing ion-exchange time. The total diameter and shape of the QDs remain the same, while the core develops a faceted octahedral like shape (see Figure 3.3D-F for illustrative high-resolution TEM images), indicating that the ion-exchange proceeds faster at the {111} surfaces of PbSe (truncated corners in Fig. 3.2B). The PbSe/CdSe heterointerface consists predominantly of Se{111} planes and appears to be atomically sharp, as expected on the basis of the very small lattice mismatch (~1%),[17] and negligible inter-diffusion between rock-salt (RS) PbSe and zinc blende (ZB) CdSe. The immiscibility of the two materials results from the different coordination numbers of the atoms in the two types of crystal structure (4-fold in ZB, 6-fold in RS).[6] The small size and octahedral-like shape of the PbSe cores make it difficult to reliably estimate the core dimensions from TEM images. Therefore, the core "diameter" of PbSe/CdSe core/shell QDs was estimated from the spectral position of the lowest energy optical absorption transition using an empirical sizing curve,[12] under the assumption that this transition involves states that are primarily localized in the PbSe core. The validity of this assumption has been demonstrated by recent studies correlating the optically estimated core size with those determined by TEM analysis.[21]

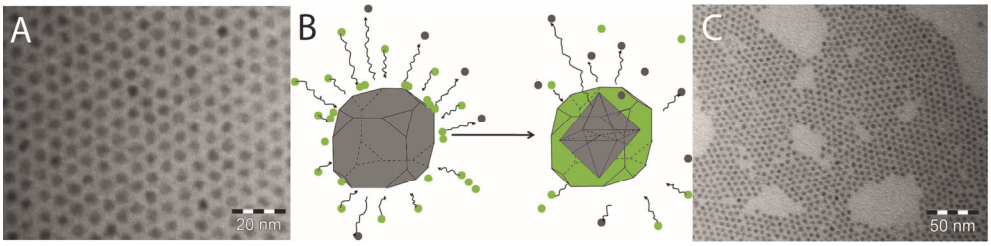

Fig. 3.2 TEM images of (A) the parent PbSe QDs (3.7 nm in diameter) and (C) PbSe/CdSe core/shell QDs obtained after 120 min of ion-exchange time (3.7 nm in total diameter). (B) Schematic diagram of the ion-exchange process (green and grey dots represent Cd and Pb atoms, respectively).

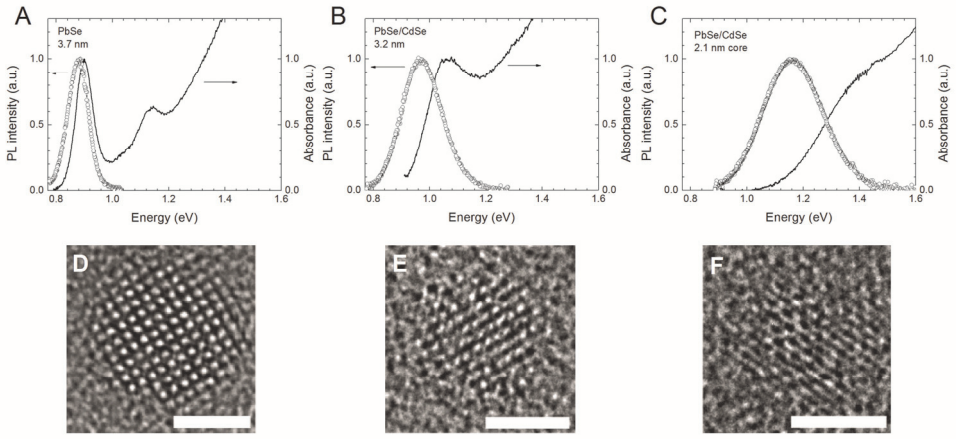

Fig. 3.3. Room temperature absorption (black line) and photoluminescence spectra (circles) of (A) PbSe NCs (3.7 nm in diameter), (B) PbSe/CdSe core/shell quantum dots of 3.7 nm with a core of 3.2 nm (C) PbSe/CdSe core/shell quantum dots of 4.2 nm with a core of 2.1 nm (different PbSe NC parent batch). The total diameter of the parent PbSe NCs is preserved during the ion-exchange. HR-TEM images of the 3.7 nm PbSe NC (D), and of the PbSe/CdSe core/shell quantum dots obtained after 5 min (E) and 60 min (F) of ion-exchange. The scale bars correspond to 2 nm.

Figure 3.3A-C presents the room-temperature absorption and PL spectra of PbSe QDs (diameter 3.7 nm), and of the PbSe/CdSe core/shell QDs obtained with PbSe core diameters of 3.2 and 2.1 nm. Illustrative HR-TEM images of these hetero-NCs are presented in Fig. 3.3 D-F. The absorption spectra of the parent PbSe NCs show two sharp absorption peaks, assigned to the $1S_h - 1S_e$ and $1P_h - 1P_e$ transitions, respectively, in agreement with previous reports.[22, 23] The $1S_h - 1S_e$ emission peak is located at 0.88 eV, slightly red shifted with respect to the corresponding absorption peak and has a FWHM of 100 meV. As discussed above, the in-growth of a CdSe shell by Pb for Cd exchange leads to a reduction of the PbSe core size (Fig. 3.3D-F), and markedly changes the optical properties. The lowest-energy absorption and the emission peaks shift to higher energies and become broader with increasing duration of Pb/Cd ion-exchange. At room temperature, the maximum of the emission peak shifts from 0.88 eV (3.7 nm PbSe QD), to 0.95 eV (3.2 nm PbSe core) and to 1.10 eV (2.1 nm PbSe core). Similar results have been reported in the original work by Pietryga *et al*.[17] and in recent work by De Geyter *et al*.[21] The blue-shift of the absorption and emission spectra can be ascribed to the decreasing size of the remaining PbSe core in the PbSe/CdSe core/shell hetero-NC, under the understanding that the exciton remains confined in the PbSe core (*i.e*., Type-I localization regime). Resonant scanning tunneling microscopy on single PbSe/CdSe core/shell QDs and optical spectroscopic investigations indicate that these hetero-NCs can best be described as a Type-I system, in which the s-electron wave function is centered in the PbSe core, albeit partially extending into the CdSe shell (Type $I^{1/2}$ system), and the hole wave function is completely confined into the core.[21, 24] It will be shown below that the broadening of the PL spectrum at room temperature reflects mainly intrinsic electronic effects taking place in small PbSe QDs.

3.3.2 Temperature dependent photoluminescence spectra

Figure 3.4 presents the PL spectra of PbSe/CdSe core/shell QDs with decreasing PbSe core diameter, measured at 5 K. It is clear that the broad PL spectra consist of two peaks. The spectra (in energy scale) were fit to a sum of multiple Gaussian bands, using the minimum number of Gaussians needed to accurately describe the spectra. In all cases the best fit was obtained with a convolution of only two peaks, and was an unique solution in terms of the position, width and total area of the Gaussians needed to accurately describe the spectra. Moreover, the spectra of different samples emitting at the same energies gave essentially the same results. The lowest and highest energy peaks will be denoted hereafter as P_1 and P_2, respectively. The intensity of each transition [$I(P_1)$ and $I(P_2)$] is given by the area under the peaks. Figure 3.4 shows that the relative intensities of the two PL peaks differ from case to case, but are reproducible for different samples emitting in the same

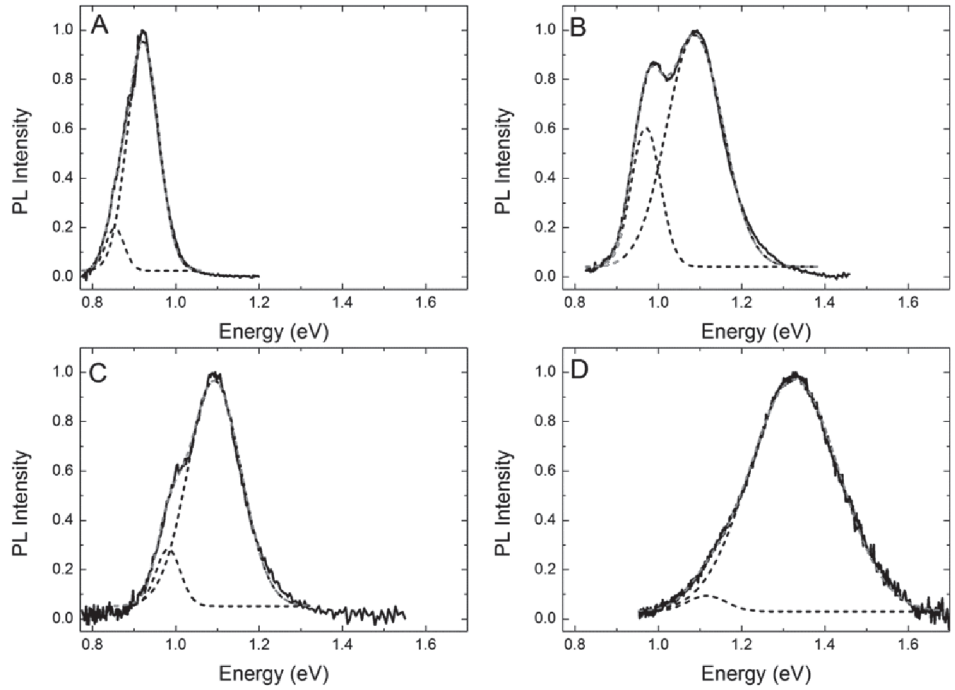

Fig. 3.4 Low temperature (5 K) photoluminescence spectra of PbSe/CdSe core/shell QDs with varying core diameters. The PL spectra are fitted to a convolution of two Gaussian peaks (dashed curves). (A) 3.2 nm PbSe core, total diameter 3.7 nm; (B) 2.1 nm PbSe core, total diameter 3.7 nm; (C) 2.1 nm PbSe core, total diameter 4.2 nm; (D) 1.1 nm PbSe core, total diameter 3.5 nm.

spectral range. The peak at lower energy is usually of lower intensity, however samples emitting at about 1 eV show a reversed behavior (Fig. 3.5).

Figure 3.6. gives an overview of the FWHM of the two contributions to the emission peak as a function of the temperature. Both peaks are temperature independent in the 5-100 K range for all samples. Very probably, the peak width at low temperatures reflects the distribution in the volume of the PbSe cores in the sample (*i.e.,* inhomogeneous broadening). Above ~100 K the width of the peaks slowly increases. This can be attributed to additional thermal broadening due to increase in the homogeneous linewidths.

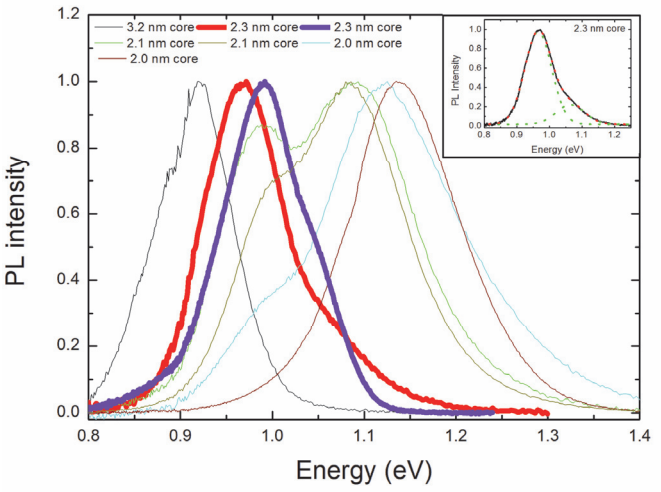

Fig. 3.5 Survey of low temperature (5 K) photoluminescence spectra of PbSe/CdSe core/shell QDs with different core diameters showing the trend of the double peaks as a function of the average emission energy. Only the samples emitting at ~1 eV show a higher intensity for the peak at lower energies. Inset shows the PL spectrum and a multi-gaussian fit for the sample with 2.3 nm diameter core (red thick curve in the main figure).

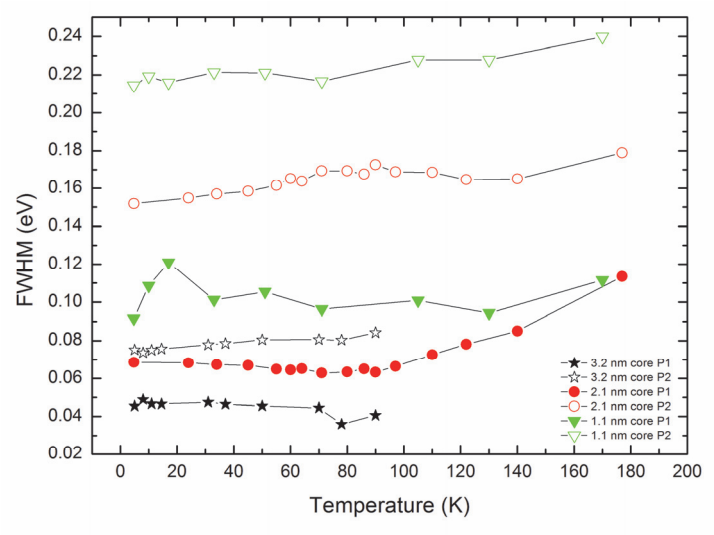

Fig. 3.6 Overview of the FWHM of the two peaks of the emission spectra versus the temperature for PbSe/CdSe core/shell QDs with a total diameter of 3.7 nm and core diameters of 3.2, 2.1 and 1.1 nm.

The observation of two PL peaks at low temperatures and under low excitation densities is unusual and striking. Below, we show that the two peaks are not due to two different types of QDs in the sample, but reflect two intrinsic emitting states of each PbSe/CdSe core/shell QD. The evidence that the two peaks are due to two different intrinsic states in each of the PbSe/CdSe core/shell quantum dots is two-fold. First, if the two peaks were due to emission from different QDs in the sample (*i.e.*, two different sub-ensembles), this would imply a bimodal distribution in the size of the PbSe QDs, or of the PbSe cores in the PbSe/CdSe core/shell QDs. However, TEM studies (see, *e.g.*, Figures 3.2 and 3.3) have never provided evidence for a bimodal size distribution. Moreover, the double emission peaks were reproducibly observed in PbSe/CdSe core/shell QD samples obtained from different syntheses and different batches of parent PbSe NCs (*e.g.*, Fig. 3.4C) and were also observed by Harbold and Wise[25] and by us in the PL spectra of plain PbSe QDs. It is unlikely that different synthesis by different groups would lead to very similar bimodal size distributions. Second, further evidence is obtained by analyzing the PLE spectra.

Figure 3.7 presents the PL excitation spectra obtained while monitoring emission at different spectral positions in the region of the double peaks. When monitoring at high energy (1.15 eV, P_2), it is evident that the lowest energy excitation peak can be fitted with just one Gaussian, reflecting the contribution of one state. In contrast, when monitoring the excitation spectrum of the low energy peak (0.97 eV, P_1+P_2), two Gaussians are needed to obtain a proper fitting of the lowest energy feature in the excitation spectrum. From this it is evident that the low-energy photoluminescence peak (P_1) partly arises from excitation into the high-energy peak (P_2). Since the nanocrystal suspension is sufficiently diluted (10^{-7} mol/L), energy transfer between QDs in the suspension cannot occur, especially at low temperatures when the sample is frozen solid. The above shows that the two peaks observed in the photoluminescence spectra originate from two intrinsic emitting states belonging to the 64-manifold of the $1S_e - 1S_h$ exciton state of PbSe. It is evident that both the PL excitation and the luminescence spectra reflect the same two states. Further, the energy separation between the emission and the lowest energy excitation (absorption) peaks is remarkably large, *viz.,* 220 and 280 meV for the low and high energy peaks, respectively.

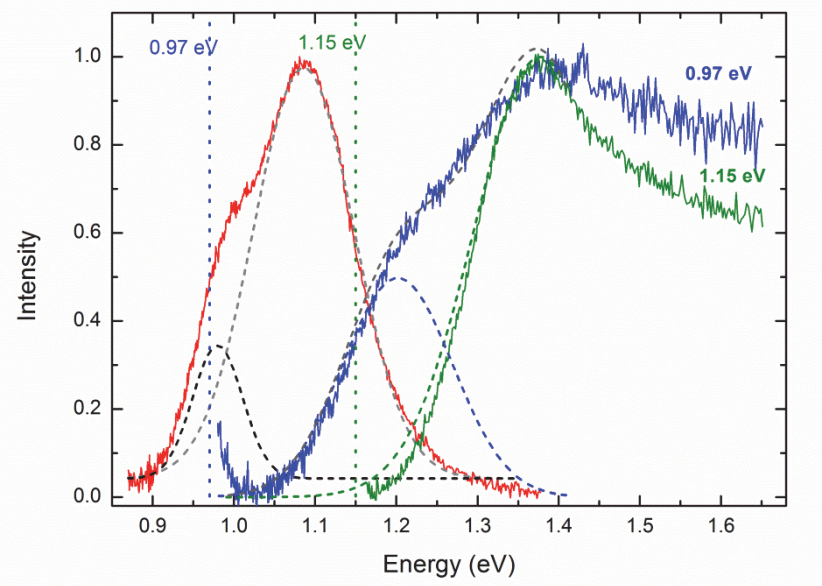

Fig. 3.7. Photoluminescence (PL, red solid line) and PL excitation spectra (blue and green lines) of PbSe/CdSe core/shell QDs with 2.1 nm diameter core (total diameter: 4.2 nm). Excitation spectra were taken while monitoring the different PL energies indicated by the dotted lines (0.97 eV, blue PLE spectrum, and 1.15 eV, green PLE spectrum). The first part of the excitation spectrum at high energy was fitted with a single Gaussian (dashed lines). This Gaussian was used as a hard parameter to fit the two Gaussians in the excitation spectrum of the low energy side (0.97 eV).

Figure 3.8 presents the PL spectra acquired in the 5 – 300 K temperature range for a PbSe/CdSe core/shell QD sample with a 2.1 nm diameter core. An additional example for QDs with a 2.3 nm core is presented in Fig. 3.9. The PL spectra can be well described by a convolution of two Gaussian peaks (*i.e.*, P_1 and P_2) at all temperatures. Furthermore, the relative intensities of the two peaks change considerably with increasing temperature. The temperature dependence of the width of the peaks is shown in Fig. 3.6. Figure 3.8D shows the temperature dependence of the total PL intensity [$I(P_1)+I(P_2)$] and of the relative intensity of the lower energy peak ($I(P_1)/[I(P_1)+I(P_2)]$). It can be seen that $I(P_1)/[I(P_1)+I(P_2)]$ decreases to a minimum from 5 to 90 K, and then increases again upon further increase in the temperature. The total PL intensity decreases gradually with increasing temperature. Although the high energy peak P_2 becomes more dominant at higher temperatures for all

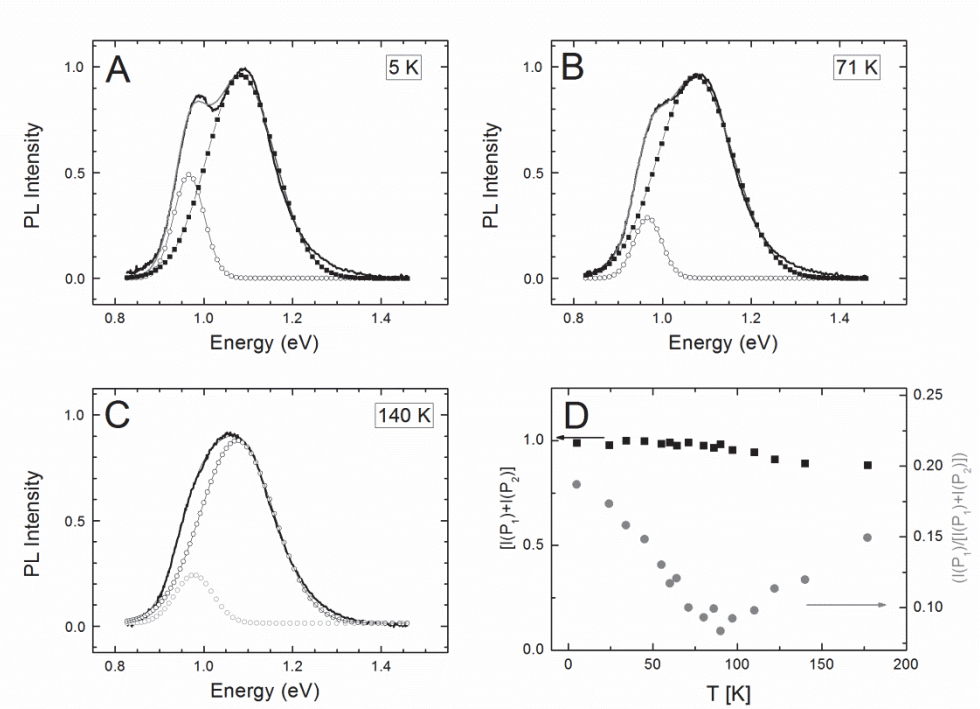

Fig.3.8 (A-C) Temperature dependent photoluminescence spectra of PbSe/CdSe core/shell QDs (60 min. of Pb/Cd ion exchange, 3.7 nm total diameter, 2.1 nm core diameter) acquired at the temperatures indicated. The spectra are fitted to a convolution of two Gaussian peaks (dotted curves). (D) Total PL intensity (squares), and ratio of the lower-energy peak intensity to the total intensity (circles) as a function of the temperature.

samples investigated, there is no evidence that the two intrinsic exciton states are thermally coupled, since the higher energy state P_2 remains prominent at 5 K. In case of thermal equilibrium the population of the higher energy state should be negligible at 5 K. Fig. 3.9 shows temperature dependent evolution of the two peak intensities of QDs sample with 2.3 nm core. It can be clearly seen that this sample show the opposite behavior, where at low temperature peak P_1 is more intense then P_2. Further temperature increase shows that the intensities of two peaks change with respect to each other and at room temperature peak P_2 becomes more dominant. The nature of this reverse behavior is still unknown.

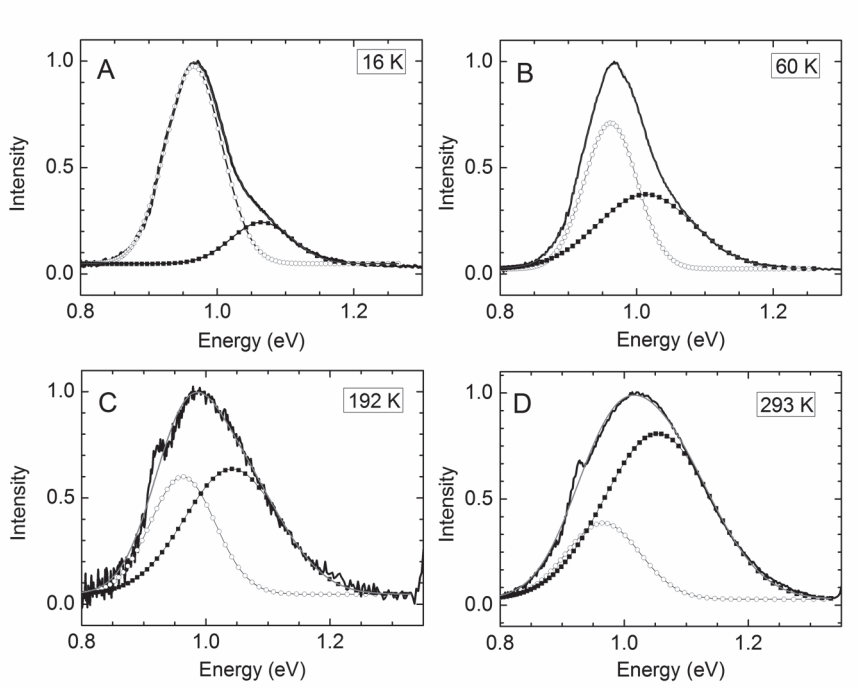

Fig. 3.9 Temperature dependent photoluminescence spectra of PbSe/CdSe core/shell QDs (30 min. of Pb/Cd ion exchange, 3.7 nm total diameter, 2.3 nm PbSe core diameter) acquired at the temperatures indicated. The spectra are fitted to a convolution of two Gaussian peaks (dotted curves).

The energies of the maxima of both emission peaks, $E(P_1)$ and $E(P_2)$, of the PbSe/CdSe core/shell QDs investigated in this work are plotted as a function of temperature in Figure 3.10B. It can be seen that the peak positions are nearly independent of the temperature. Further, both peaks shift to higher energies with decreasing volume of the PbSe core. In addition, the energy separation $E(P_2)$-$E(P_1)$ increases considerably with decreasing core size, from 70 meV for a 3.2 nm core to 210 meV for a 1.1 nm core (Figure 3.10C). A similar trend has been observed by Harbold and Wise[25] for PbSe QDs in QD solid films and by us for colloidal PbSe QDs in diluted suspensions (10^{-7} mol/L). The PL energy splitting values observed for PbSe QDs are also included in Fig. 3.10C. Interestingly, the PbSe/CdSe core/shell QDs, the parent PbSe QDs in solution and the PbSe QDs in QD solids all follow the same size-dependent trend. These observations provide another strong indication that the two PL peaks are not due to two different sub-ensembles of QDs in the

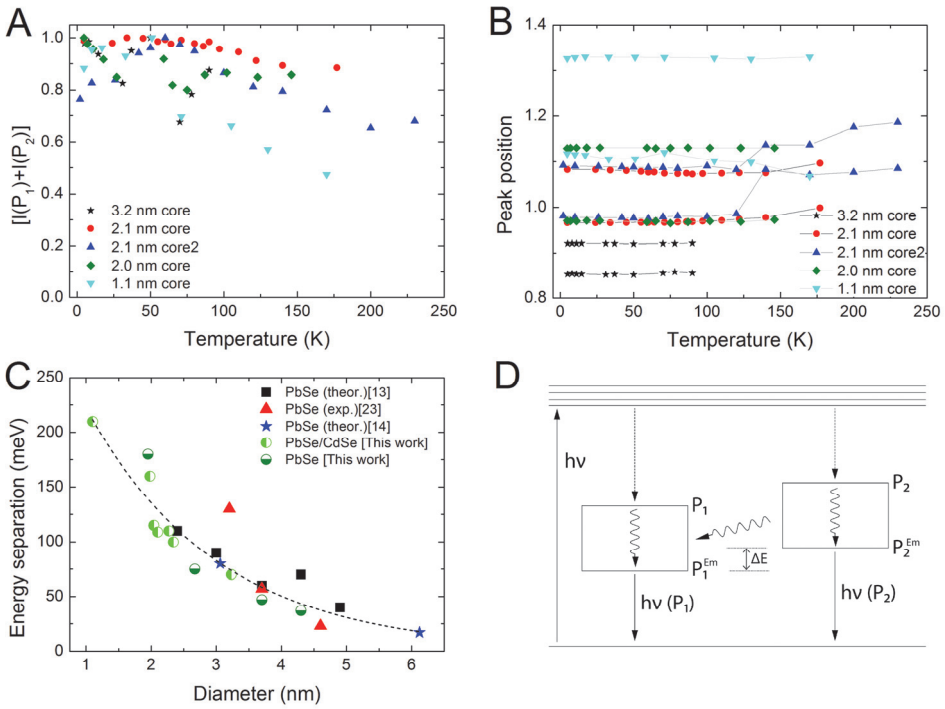

Fig.3.10 (A) Total emission intensity [I(P_1)+I(P_2)] of PbSe/CdSe core/shell QD samples with various sizes as a function of temperature. (B) Temperature dependence of the positions of the lower and higher energy PL peaks of PbSe/CdSe core/shell QDs (C) Energy separation between the higher and lower energy PL peaks as a function of the diameter of the PbSe core. Experimental data for PbSe QDs, obtained in this work and from ref.[25], are also included. The values from ref.[25] were obtained for PbSe QD solids, while our data concerns diluted suspensions of colloidal PbSe QDs. The theoretically predicted intervalley coupling splitting in the $1S_e - 1S_h$ exciton fine structure of PbSe QDs is also included for comparison using the values calculated by An et al.[14] and Allan and Delerue.[13] The dashed line represents a guide to the eye. (D) Schematic representation of the two states. The lower line represents the ground state while the top lines represent higher energy levels. The boxes (P_1 and P_2) represent (parts) of the 64-fold 1st excited state ($1S_e - 1S_h$). ΔE is the energy difference between the two emitting states.

samples, but rather reflect an intrinsic property of PbSe QDs. The origin of the energy separation between the two peaks will be discussed below.

3.3.3 Photoluminescence decay rates

Figure 3.11A presents room temperature PL decay curves of a series of PbSe/CdSe core/shell QD samples with decreasing core size, obtained from 3.7 nm diameter PbSe QDs. The decay curve of the parent PbSe QDs is also shown. The decay transients were acquired while monitoring the maximum of the PL peak, which corresponds to a wavelength in between the two PL peaks mentioned above. It can be clearly seen that the PL decay rates decrease with decreasing volume of the PbSe core. The slightly non-exponential decay curves can be accurately fitted with log-normal distribution functions [26] (Figure 3.11B). The results show that the average lifetime increases with decreasing volume of the PbSe cores with a concomitant broadening in the distribution of decay rates. It is reasonable to assume that the inhomogeneity of the PbSe/CdSe QDs in the sample (*i.e.,* distribution of core volumes) is the main cause of the slightly multi-exponential character of the observed decay curves. It is of interest to distinguish the decay dynamics of the two radiative transitions by monitoring narrow spectral regions pertaining to the two peaks. Figure 3.11C presents the PL decay curves measured at $E(P_1)$ (0.99 eV) and at $E(P_2)$ (1.07 eV) for the PbSe/CdSe core/shell QD sample with 2.1 nm diameter core at 5 K. The decay curves can be fitted with a log-normal distribution function, yielding slightly faster average decay rates for P_2 (*viz.,* 9.3×10^4 and 6.3×10^4 s^{-1}, for P_1 and P_2, respectively). If we assume that the contribution of non-radiative recombination can be neglected, it can be concluded that the radiative decay rates of both intrinsic transitions differ by a factor of ~1.5, where a factor of 2 is expected based on the difference in emission energies. This shows that the transition dipole moments for the two transitions are similar.

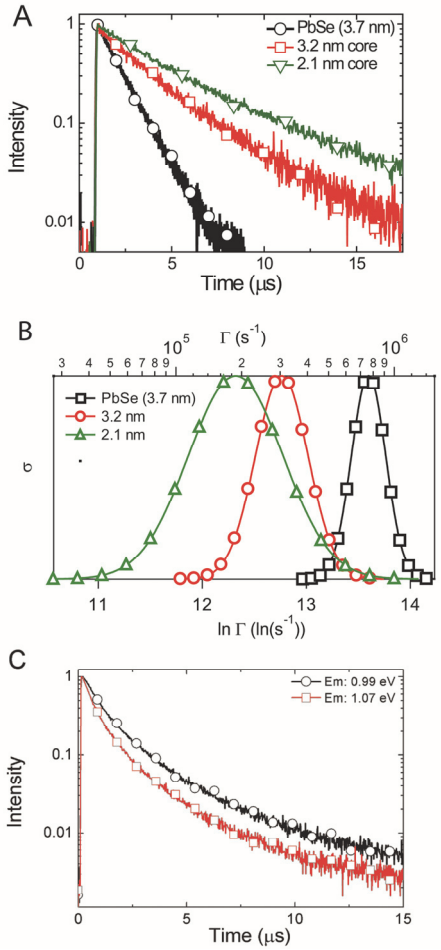

Fig. 3.11 (A) Room temperature photoluminescence decay curves of PbSe/CdSe core/shell QDs obtained from 3.7 nm diameter PbSe QDs by Pb/Cd ion exchange. The total diameter is preserved, while the PbSe core diameter decreases with increasing reaction time (*viz*., 5 min: 3.2 nm; 60 min: 2.1 nm). The PL decay curve of the parent PbSe QD is also shown for comparison. The monitored wavelengths correspond to the maximum of the PL peak in all cases. (B) Decay rate distributions obtained by fitting the decay curves to log-normal distribution functions, where Γ is the decay rate and σ gives the relative probability of a given decay rate to occur (for clarity, the maxima of σ have been normalized to one). (C) PL decay curves of PbSe/CdSe QDs with a 2.1 nm core (total diameter: 3.7 nm) measured at 5 K. The decay transients were obtained for two different emission energies (0.99 eV and 1.07 eV), corresponding to the peak positions of the lower- and higher-energy emission, respectively.

3.3.4 Exciton fine structure in the PL spectra of PbSe NCs

The results above show that PbSe and PbSe/CdSe core/shell QDs have two emitting states in the 64-manifold of the $1S_e - 1S_h$ exciton state. It could be argued that the lower energy peak P_1 is due to radiative recombination via surface- or interfacial states. However, it should be realized that PbSe QDs of sizes similar to the PbSe cores investigated here also show a two-fold PL peak, with very similar separations between the two peaks, both in diluted colloidal suspensions and QD solids (Figure 3.10C). It is extremely unlikely that widely different interfaces (*viz.*, the oleic acid capped PbSe QD surface in solution and in a QD solid, and the PbSe/CdSe hetero-interface) would show exactly the same type of localized states. Moreover, trap-related radiative recombination was excluded by Harbold and Wise[25] as the origin for the double PL peak observed in their work on PbSe QD solids, since the PL spectra maintained their shape when the excitation densities were varied over many orders of magnitude. The absence of trap-saturation formed an argument to assign both PL peaks to intrinsic exciton states of small PbSe QDs.[25] The absence of optically active surface traps is in line with the results of tight-binding[13] and first-principle calculations[15] for PbSe QDs. Moreover, the PL excitation spectra (see, *e.g.,* Fig. 3.7) clearly show the existence of two intrinsic states; the peak intensities indicate that the higher energy state has a somewhat stronger absorption (emission) strength then the lower-energy peak. This is in line with the PL decay curves, showing a higher decay rate for the emission at higher energy. Hence, excitation and emission in PbSe and PbSe/CdSe core/shell QDs can be schematically represented as shown in Figure 3.10D.

The intricate electronic structure of PbSe QDs has received much attention. It has been theoretically found that the 64-fold degeneracy of the $1S_h - 1S_e$ exciton is partially lifted by inter-valley coupling and anisotropy, and valence band-conduction band coupling. An et al. have discussed in detail the effects of inter-valley coupling and electron-hole exchange on the allowed exciton transitions.[14] For PbSe QDs of 3.06 nm diameter they find that inter-valley coupling leads to two allowed transitions, separated by 80 meV. This is in good agreement with the energy separation observed between the two PL peaks of the PbSe/CdSe core/shell (3.2 nm core) QD sample investigated here (Fig. 3.10C). Delerue and Allan found that inter-valley coupling splits the electron and hole energy levels into groups.[13] The energy separation between these groups increases when the PbSe NC size is reduced below 4 nm.[13] The exciton states themselves were not discussed. Harbold and Wise[25] compared the energy separation between the double-peaks observed in the low temperature PL spectra of PbSe QDs (3 – 4.6 nm diameter range) with the maximum inter-valley splitting calculated from the energy level splitting reported by Allan and Delerue[13] and found a fair agreement. In Fig. 3.10C, we plot the energy separation between the two

PL peaks [$E(P_2)$ - $E(P_1)$] versus the PbSe core size of PbSe/CdSe core/shell QDs and the diameter of PbSe colloidal QDs investigated in the present work. The data obtained by Harbold and Wise[25] is also included. It is clear that there is a good agreement between the energy separation, the intervalley-splitting calculated by An et al.[14], and the maximum splitting derived from the energy levels calculated by Delerue and Allan.[13] This suggests the inter-valley coupling as the most likely origin of the two-fold exciton emission observed in PbSe and PbSe/CdSe core/shell QDs.

The observation of two exciton emissions separated by 70-210 meV over a broad temperature range is quite remarkable, since it implies the kinetic isolation of the two emitting states and the absence of thermalization between them. In case of thermal equilibrium, only luminescence from the lower exciton state would be observed in the low temperature range, *i.e.,* $k_BT << [E(P_2) - E(P_1)]$. Hence, it is likely that after the absorption of a non-resonant photon, there is a comparable probability that the higher exciton state relaxes into one of the two emitting fine-structure $1S_h - 1S_e$ exciton states (figure 3.10D, P_1 and P_2). The excitation spectra show that the higher energy state can relax into the lower one, but the temperature dependence of both peaks excludes thermal equilibration. We note that the coexistence of emission from two different states without thermalization is a common occurrence in organic molecules (*viz.*, singlet and triplet states) and has also been reported for s^2-ions where emission from two minima in the Jahn-Teller split excited sp state occurs,[27, 28] but is unusual for semiconductor NCs at low excitation densities. Nevertheless, the observation of two coexisting emission transitions has been recently reported for CdTe/CdSe hetero-NCs, and was ascribed to two exciton emitting states with different degrees of spatial localization.[29] In the case of PbSe and PbSe/CdSe core/shell QDs the two emitting states should be ascribed to fine-structure exciton states originating from the partial lifting of the 64-fold degeneracy of the $1S_h - 1S_e$ exciton by inter-valley coupling and electron-hole exchange interactions. It is also striking that both states show a large shift (>200 meV) between the lowest energy absorption and the emission (see figure 3.10D). Each state shows strong relaxation effects, and moreover the higher-energy state can also relax into the lower-energy state. In contrast to what was reported by Harbold and Wise,[25] up-conversion has not been observed in the present work under laser excitation.

The results presented here show that there is an intriguing dependence of the relative intensities of the two PL peaks on the temperature. For example, Figure 3.8 shows that in the 5 to 90 K temperature range, the high energy peak gains intensity with increasing temperature while the low energy peak becomes weaker and the total PL intensity remains (nearly) constant. A minimum in $I(P_1)/[I(P_1) + I(P_2)]$ is reached at 90 K, and upon further temperature increase, the low-energy peak regains intensity while the high-energy peak becomes weaker. Very probably this reflects thermal communication with dark states of the

64-fold $1S_e - 1S_h$ manifold. It is beyond the scope of the present work to obtain a quantitative understanding of this intriguing behaviour.

3.4 Conclusions

In summary, we report the occurrence of two radiative transitions in colloidal PbSe and PbSe/CdSe core/shell quantum dots. We present strong evidence that the two emitting states can be attributed to two bright excitons originating from the $1S_h - 1S_e$ manifold of PbSe QDs. Very likely the energy separation between the two states is caused by inter-valley coupling and electron-hole exchange. The evolution of the two luminescence peaks with the temperature is non-trivial and implies an intricate communication between bright and dark states. The understanding of this unusual temperature-dependence will require new theoretical efforts.

References

1. Groiss, H., E. Kaufmann, G. Springholz, T. Schwarzl, G. Hesser, F. Schaffler, W. Heiss, K. Koike, T. Itakura, T. Hotei, M. Yano, and T. Wojtowicz, *Size control and midinfrared emission of epitaxial PbTe/CdTe quantum dot precipitates grown by molecular beam epitaxy.* Applied Physics Letters, 2007. **91**(22): p. 222106.
2. Konstantatos, G., I. Howard, A. Fischer, S. Hoogland, J. Clifford, E. Klem, L. Levina, and E.H. Sargent, *Ultrasensitive solution-cast quantum dot photodetectors.* Nature, 2006. **442**(7099): p. 180-183.
3. Rauch, T., M. Boberl, S.F. Tedde, J. Furst, M.V. Kovalenko, G. Hesser, U. Lemmer, W. Heiss, and O. Hayden, *Near-infrared imaging with quantum-dot-sensitized organic photodiodes.* Nat Photon, 2009. **3**(6): p. 332-336.
4. Heiss, W., H. Groiss, E. Kaufmann, G. Hesser, M. Boberl, G. Springholz, F. Schaffler, K. Koike, H. Harada, and M. Yano, *Centrosymmetric PbTe/CdTe quantum dots coherently embedded by epitaxial precipitation.* Applied Physics Letters, 2006. **88**(19): p. 192109.
5. Lambert, K., B.D. Geyter, I. Moreels, and Z. Hens, *PbTe|CdTe Core|Shell Particles by Cation Exchange, a HR-TEM study.* Chemistry of Materials, 2009. **21**(5): p. 778-780.
6. de Mello Donegá, C., *Synthesis and properties of colloidal heteronanocrystals.* Chemical Society Reviews, 2011. **40**: p. 1512.
7. Law, M., M.C. Beard, S. Choi, J.M. Luther, M.C. Hanna, and A.J. Nozik, *Determining the Internal Quantum Efficiency of PbSe Nanocrystal Solar Cells with the Aid of an Optical Model.* Nano Letters, 2008. **8**(11): p. 3904-3910.
8. Sukhovatkin, V., S. Hinds, L. Brzozowski, and E.H. Sargent, *Colloidal Quantum-Dot Photodetectors Exploiting Multiexciton Generation.* Science, 2009. **324**(5934): p. 1542-1544.

9. Trinh, M.T., A.J. Houtepen, J.M. Schins, T. Hanrath, J. Piris, W. Knulst, A.P.L.M. Goossens, and L.D.A. Siebbeles, *In Spite of Recent Doubts Carrier Multiplication Does Occur in PbSe Nanocrystals.* Nano Letters, 2008. **8**(6): p. 1713-1718.
10. Sashchiuk, A., L. Amirav, M. Bashouti, M. Krueger, U. Sivan, and E. Lifshitz, *PbSe Nanocrystal Assemblies: Synthesis and Structural, Optical, and Electrical Characterization.* Nano Letters, 2004. **4**(1): p. 159-165.
11. Wise, F.W., *Lead Salt Quantum Dots: the Limit of Strong Quantum Confinement.* Accounts of Chemical Research, 2000. **33**(11): p. 773-780.
12. Moreels, I., K. Lambert, D. De Muynck, F. Vanhaecke, D. Poelman, J.C. Martins, G. Allan, and Z. Hens, *Composition and Size-Dependent Extinction Coefficient of Colloidal PbSe Quantum Dots.* Chemistry of Materials, 2007. **19**(25): p. 6101-6106.
13. Allan, G. and C. Delerue, *Confinement effects in PbSe quantum wells and nanocrystals.* Physical Review B, 2004. **70**(24): p. 245321.
14. An, J.M., A. Franceschetti, and A. Zunger, *The Excitonic Exchange Splitting and Radiative Lifetime in PbSe Quantum Dots.* Nano Letters, 2007. **7**(7): p. 2129-2135.
15. Franceschetti, A., *Structural and electronic properties of PbSe nanocrystals from first principles.* Physical Review B, 2008. **78**(7): p. 6.
16. Leitsmann, R., L.E. Ramos, and F. Bechstedt, *Structural properties of PbTe/CdTe interfaces from first principles.* Physical Review B, 2006. **74**(8): p. 085309.
17. Pietryga, J.M., D.J. Werder, D.J. Williams, J.L. Casson, R.D. Schaller, and V.I. Klimov, *Utilizing the Lability of Lead Selenide to Produce Heterostructured Nanocrystals with Bright, Stable Infrared Emission.* Journal of the American Chemical Society, 2008. **130**(14): p. 4879-4885.
18. Heiss, W., H. Groiss, E. Kaufmann, G. Hesser, M. Boberl, G. Springholz, F. Schaffler, R. Leitsmann, F. Bechstedt, K. Koike, H. Harada, and M. Yano, *Quantum dots with coherent interfaces between rocksalt-PbTe and zincblende-CdTe.* Journal of Applied Physics, 2007. **101**(8): p. 081723.
19. Houtepen, A.J., R. Koole, D. Vanmaekelbergh, J. Meeldijk, and S.G. Hickey, *The Hidden Role of Acetate in the PbSe Nanocrystal Synthesis.* Journal of the American Chemical Society, 2006. **128**(21): p. 6792-6793.
20. Grodzinska, D., F. Pietra, M.A. van Huis, D. Vanmaekelbergh, and C. de Mello Donega, *Thermally induced atomic reconstruction of PbSe/CdSe core/shell quantum dots into PbSe/CdSe bi-hemisphere hetero-nanocrystals.* Journal of Materials Chemistry, 2011. **21**(31): p. 11556-11565.
21. De Geyter, B., Y. Justo, I. Moreels, K. Lambert, P.F. Smet, D. Van Thourhout, A.J. Houtepen, D. Grodzinska, C. de Mello Donega, A. Meijerink, D. Vanmaekelbergh, and Z. Hens, *The Different Nature of Band Edge Absorption and Emission in Colloidal PbSe/CdSe Core/Shell Quantum Dots.* ACS Nano, 2011. **5**(1): p. 58-66.
22. Koole, R., G. Allan, C. Delerue, A. Meijerink, D. Vanmaekelbergh, and Arjan J. Houtepen, *Optical Investigation of Quantum Confinement in PbSe Nanocrystals at Different Points in the Brillouin Zone.* Small, 2008. **4**(1): p. 127-133.
23. Liljeroth, P., P.A.Z. van Emmichoven, S.G. Hickey, H. Weller, B. Grandidier, G. Allan, and D. Vanmaekelbergh, *Density of States Measured by Scanning-Tunneling Spectroscopy Sheds New Light on the Optical Transitions in PbSe Nanocrystals.* Physical Review Letters, 2005. **95**(8): p. 086801.
24. Swart, I., Z. Sun, D.l. Vanmaekelbergh, and P. Liljeroth, *Hole-Induced Electron Transport through Core-Shell Quantum Dots: A Direct Measurement of the Electron-Hole Interaction.* Nano Letters, 2010. **10**(5): p. 1931-1935.
25. Harbold, J.M. and F.W. Wise, *Photoluminescence spectroscopy of PbSe nanocrystals.* Physical Review B, 2007. **76**(12): p. 125304.

26. van Driel, A.F., I.S. Nikolaev, P. Vergeer, P. Lodahl, D. Vanmaekelbergh, and W.L. Vos, *Statistical analysis of time-resolved emission from ensembles of semiconductor quantum dots: Interpretation of exponential decay models.* Physical Review B, 2007. **75**(3): p. 035329.
27. Jacobs, P.W.M., *Alkali halide crystals containing impurity ions with the ns2 ground-state electronic configuration+.* Journal of Physics and Chemistry of Solids, 1991. **52**(1): p. 35-67.
28. Oomen, E.W.J.L., W.M.A. Smit, and G. Blasse, *Jahn-Teller effect in the Sb3+ emission in zircon-structured phosphates.* Chemical Physics Letters, 1984. **112**(6): p. 547-550.
29. de Mello Donegá, C., *Formation of nanoscale spatially indirect excitons: Evolution of the type-II optical character of CdTe/CdSe heteronanocrystals.* Physical Review B, 2010. **81**(16): p. 165303.

4

Thermally Induced Atomic Reconstruction of PbSe/CdSe Core/Shell Quantum Dots into PbSe/CdSe Bi-hemisphere Heteronanocrystals

The properties of heteronanocrystals(HNCs) depend strongly on the mutual arrangement of the nanoscale components. In this chapter we have investigated the structural and morphological evolution of colloidal PbSe/CdSe core/shell quantum dots upon annealing under vacuum. Prior to annealing the PbSe core has an approximately octahedral morphology with eight {111} facets, and the CdSe shell has zinc-blende crystal structure. Thermal annealing under vacuum at temperatures between 150 °C and 200 °C induces a structural and morphological reconstruction of the HNCs whereby the PbSe core and the CdSe shell are reorganized into two hemispheres joined by a common {111} Se plane. This thermally induced reconstruction leads to considerable changes in the optical properties of the colloidal PbSe/CdSe HNCs.

4.1 Introduction

Lead chalcogenide (*e.g.*, PbSe, PbS) nanocrystals (NCs) have attracted increasing attention over the past decade due to their optical properties in the near- and mid-infrared spectral range.[1, 2] The small effective masses of the carriers, and hence large exciton Bohr radii of these materials (*e.g.*, 46 nm for PbSe),[1, 2] result in strong quantum confinement for relatively large NCs, making it possible to tune the optical properties of Pb-chalcogenide NCs over a wide spectral range by controlling their size. For example, the band gap of PbSe NCs (or quantum dots, QDs) can be tuned from the bulk value (0.3 eV) up to about 1.5 eV by decreasing the NC diameter in the 100 to 2 nm range.[3] PbSe QDs are thus promising materials for optoelectronic applications in the near- and mid-IR (*e.g.*, photodetectors, LEDs, photonic switches, and photovoltaic cells).[1, 2, 4-6]

The full realization of the potential of PbSe and other Pb-chalcogenide QDs has been severely hampered by their inherent photochemical instability under ambient conditions. Overcoating of a QD by a wider band gap semiconductor material, yielding a core/shell hetero-nanocrystal (HNC) with a Type-I band alignment, has been successfully used as a strategy to enhance the photoluminescence (PL) quantum yields (QYs) and to improve the stability of a variety of colloidal QDs.[7] The recent development of a cation-exchange method to make core/shell HNCs of Pb-chalcogenides (*e.g.*, PbSe/CdSe,[8] and PbTe/CdTe[9]) has made it possible to greatly enhance the PL efficiency and the air stability of PbSe QDs.[10] The ability to make HNCs also opens up new opportunities for property engineering, since it enables the creation of spatially indirect excitons by joining materials with staggered (*i.e.*, Type-II) band alignments.[7, 11] It should be noted that the growth of heteronanostructures by colloidal chemistry methods[7, 12, 13] offers a cost effective alternative to classic solid-state technology based on chemical vapour deposition (CVD) or molecular beam epitaxy (MBE).[14]

PbSe/CdSe HNCs are of considerable interest, not only for their higher PL QYs and stability with respect to plain PbSe QDs, but also because they are anticipated to possess a number of novel optoelectronic properties. CdSe crystallizes in the wurtzite (WZ) or zinc-blende (ZB) structure and has a low refractive index (2.6),[15] while PbSe has a rock-salt (RS) crystal structure and a high refractive index (4.7).[8] Moreover, the effective masses of the carriers in the two materials are quite different (*viz.*, m_e*= 0.047, m_h*= 0.040 for PbSe;[16] and m_e*= 0.12, m_h*= 0.8 for CdSe[17]). The difference in the coordination numbers of the atoms in the two types of crystal structure (4-fold in ZB or WZ, 6-fold in RS) precludes interdiffusion and makes CdSe ZB and PbSe RS nearly immiscible.[7] In combination with a very small lattice mismatch (~1%),[8] this may lead to an atomically sharp PbSe/CdSe heterointerface, consisting of a Se {111} plane.[9, 18] Recent investigations by resonant scanning tunnelling spectroscopy and optical spectroscopy indicate that

spherical PbSe/CdSe core/shell QDs can best be described as a type-I system, in which the hole wave function is completely confined into the PbSe core, while the s-electron wave function is centred in the core, albeit partially extending into the shell.[19, 20] It is well established that the properties of HNCs are dictated not only by their composition, but also by their shape and the mutual arrangement of the HNC components.[7, 12] Therefore, the development of methodologies to control the shape and architecture of PbSe/CdSe HNCs is of great interest, but has been so far difficult to achieve.

There are a number of synthesis strategies to make shape-controlled colloidal HNCs.[7] Thermally induced recrystallization or reconstruction of HNCs has recently emerged as a promising technique to obtain heterodimer HNCs from concentric core/shell HNCs (*e.g.*, γ-Fe_2O_3-CdS, Au-Ag_2S).[7, 12] Several studies have focused on thermal reconstruction of embedded NCs grown by MBE (*e.g.,* InAs/GaAs,[21] PbTe/CdTe[22]). Little is known, however, about post-growth thermal reconstruction of colloidal NCs and HNCs. In this work, we have studied the thermal stability of colloidal PbSe/CdSe core/shell HNCs both in vacuum and dispersed in a solvent. We observe that PbSe/CdSe core/shell HNCs are more stable than plain PbSe NCs with respect to thermally induced ripening and coalescence, since the overall NC shape and size are preserved. However, upon thermal annealing under high vacuum these HNCs undergo a remarkable process of internal atomic reconstruction, through which the PbSe/CdSe concentric core/shell QDs are converted into PbSe/CdSe bi-hemisphere dimer HNCs. Furthermore, we present our efforts to perform this remarkable reconstruction under technological relevant conditions, by annealing the PbSe/CdSe HNCs directly in colloidal suspension and under moderate vacuum in a rotary evaporator. The role of the annealing temperature and pressure, and the influence of the PbSe/CdSe volume ratio and of capping molecules in the HNC reconstruction are also discussed. Finally, the optical properties of PbSe/CdSe HNCs prior to and after thermal annealing are presented. These results open up the exciting possibility of using controlled thermal annealing to produce larger amounts of colloidal PbSe/CdSe bi-hemisphere HNCs, which are anticipated to possess intriguing optoelectronic properties due to the formation of dipolar spatially indirect excitons.

4.2 Experimental Section

4.2.1 Synthesis and characterization

The colloidal PbSe/CdSe core/shell HNCs investigated in this work were synthesized in two steps. First, oleic acid capped PbSe QDs were grown following the method developed by Houtepen *et al.*[23] Subsequently, the PbSe NCs were converted into PbSe/CdSe

core/shell HNCs by a Pb^{2+} for Cd^{2+} ion-exchange reaction, carried out at 100 °C with cadmium oleate as the Cd source and using toluene/1-octadecene mixture (4:1 volume ratio) as solvent.[8] The overall size and shape of the NC remains unchanged upon ion-exchange, hence the duration of the reaction defines the thickness of the CdSe shell and the size of the remaining PbSe core. The syntheses were carried out under inert atmosphere conditions. To remove reaction by-products (Pb-oleate, excess Cd-oleate, etc.) the PbSe/CdSe HNCs were purified twice by precipitation with methanol/acetone and redissolution in tetrachloroethylene (TCE). High-resolution transmission electron microscopy (HR-TEM) was performed using an aberration-corrected Titan microscope operating at 300 kV. Scanning transmission electron microscopy (STEM) was performed using a Tecnai microscope operating at 200 kV. Absorption spectra were measured using a Perkin-Elmer Lambda 950 UV/VIS/IR absorption spectrophotometer. Photoluminescence (PL) and PL excitation spectra were recorded using an Edinburgh Instruments FLS920 spectrofluorometer.

4.2.2 Thermal annealing

The effects of thermal annealing on PbSe/CdSe core/shell HNCs were investigated in several ways, both under vacuum and in solution:

(A) *in situ* heating at 200 °C under a pressure of 10^{-7} mbar in a high-resolution TEM, using low-drift MEMS micro-heaters for high-resolution imaging at elevated temperature.[24] The HNCs were deposited on the SiN heating chip by drop-casting suspensions in tetrachloroethylene (TCE).

(B) *in situ* heating at 150 °C under a pressure of 10^{-11} mbar in an Omicron scanning tunneling microscope (STM). The HNCs were deposited on a SiN TEM grid by drop-casting suspensions in toluene.

(C) heating at 160 °C under a pressure of 10^{-6} mbar in a rotary evaporator (rotavap), operating in the static mode, or at 175 °C in a Schlenk line. The HNCs were introduced as colloidal suspensions in TCE. After the thermal treatment the HNCs were redissolved in toluene and transferred to TEM grids by dip coating.

(D) heating at different temperatures (150 °C - 240 °C) under inert atmosphere conditions (glove box) in colloidal suspensions using a variety of solvents: 1-octadecene (ODE), diphenyl ether (DPE), Trioctylphosphineoxide (TOPO), Trioctylphosphine (TOP), and Hexadecylamine (HDA).

4.3 Results and discussion

Figure 4.1 shows HR-TEM images of PbSe/CdSe core/shell HNCs and model interpretation of their structures. The PbSe core has an approximately octahedral morphology (Fig. 4.1A) with eight Se(111) interfacial planes shared with the CdSe shell. The CdSe shell has a zinc-blende crystal structure. The lattice mismatch between the Se(111) planes of both crystals is less than 1%,[8, 18] which leads to a nearly perfect heteroepitaxial interface. The PbSe and CdSe parts of the HNC are in a cube-on-cube orientation relationship, *i.e.*, the two cubic crystal structures are mutually aligned along their main axes. Therefore, in Fig. 4.1C both materials are projected along the [011] crystallographic direction, and in Fig. 4.1E both are projected along the [001] direction. The [011] projection (Fig. 4.1B and C) shows a diamond shaped core with PbSe (111) edges, which are edge-on projections of the interfacial {111} planes, and the CdSe shell can be clearly distinguished. The [001] projection (Fig. 4.1D and E) shows an approximately square view of the core with PbSe (011) edges. The CdSe shell structure, however, is less visible in this projection, due to the different crystallographic orientation. The core/shell configuration is structurally metastable.

Upon *in-situ* annealing at 200 °C under vacuum (10^{-7} mbar) in the high-resolution TEM, the HNCs preserve their original nearly-spherical shape, but undergo a drastic atomic reconstruction whereby the total number of atoms stays constant. The CdSe shell material is displaced to one side of the HNC, and both CdSe and PbSe NCs reconstruct to form a heteronanocrystal consisting of two attached hemispheres with a single preferential PbSe{111}/CdSe{111} heterointerface (Figure 4.2), *i.e.*, a PbSe/CdSe bi-hemisphere HNC. The CdSe hemisphere has the cubic zinc-blende structure. Similar to the core/shell structure, also here the Se{111} atomic plane makes a nearly perfect heterointerface.

PbSe/CdSe bi-hemisphere HNCs were also observed after annealing the PbSe/CdSe core/shell HNCs at 150 °C under ultra high vacuum (10^{-11} mbar) in a STM (Figure 4.3). The particles were heated on a conductive SiN TEM grid that was directly transported to the HR-TEM for imaging. The PbSe and CdSe components of the bi-hemisphere HNCs can be clearly distinguished in Figures 4.3A and 4.3B. The presence of bi-hemisphere HNCs is also confirmed by the STEM image (Fig. 4.3C), where the brighter parts correspond to the PbSe hemispheres and the darker ones to the CdSe hemispheres. These results clearly show that the atomic reconstruction of PbSe/CdSe core/shell QDs into bi-hemisphere HNCs is induced by the thermal annealing, ruling out electron beam effects.

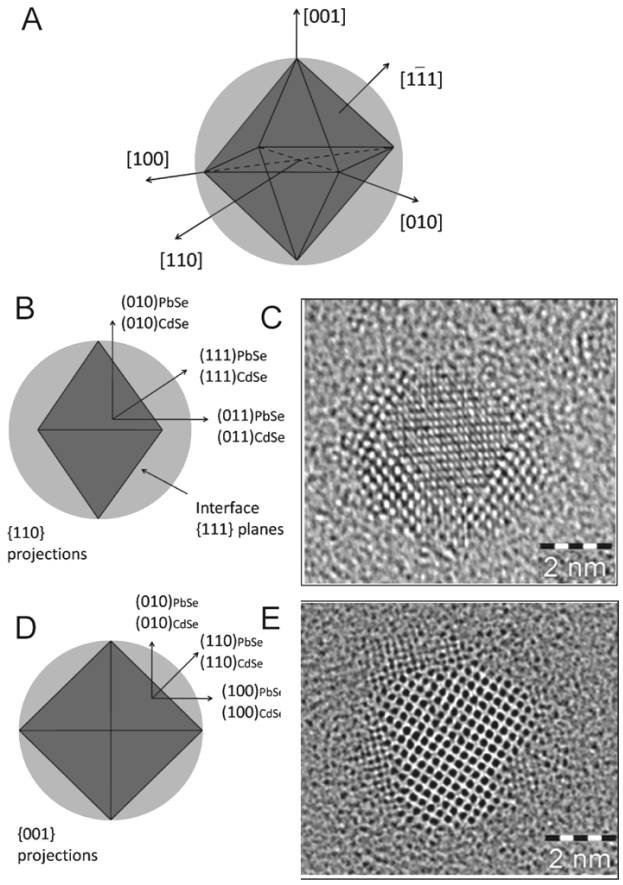

Fig. 4.1 Models of the PbSe/CdSe core/shell heteronanocrystal structure showing the octahedral shape of the PbSe core (A), and two projections along the [011] axis (B) and [001] axis (D). HR-TEM images of PbSe/CdSe core/shell QDs: projection along the [011] axis of PbSe (C); and projection along the [001] axis of PbSe (E).

The morphology and structure of colloidal NCs and HNCs are frequently not the equilibrium ones, because the growth is carried out under kinetically controlled conditions.[7] Moreover, surface and interfacial free energies account for a significant part of the total free energy of nanocrystals due to their large surface to volume ratio.[7] Consequently, the shape and structure of colloidal NCs and HNCs are often observed to evolve in response to changes in their environment. For example, thermal annealing of CdSe nanorods at 300 °C at low monomer concentration leads to a process of internal

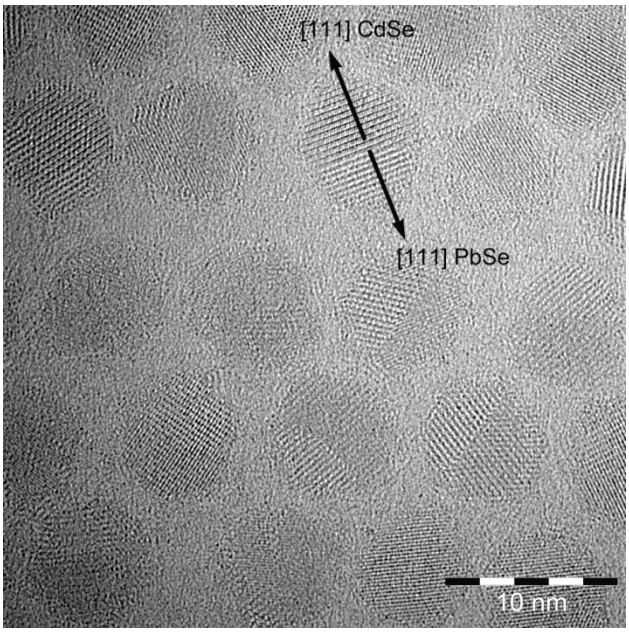

Fig. 4.2 HR-TEM image of PbSe/CdSe bi-hemisphere heteronanocrystals created after *in-situ* annealing of PbSe/CdSe core/shell QDs at 200 °C under vacuum (10^{-7} mbar).

ripening in which CdSe units migrate from high energy facets to low energy facets, leading to a progressive reduction in the aspect ratio, until a roughly isotropic shape is achieved.[7]

It has recently been shown that thermal annealing of organically capped PbSe QDs at 100 °C by *in situ* TEM leads to NC unification via oriented attachment,[25] through which PbSe NCs fuse into a wide variety of one- and two-dimensional nanostructures. The fusion of PbSe NCs is driven by reduction of surface and interfacial energies, since the unification process reduces the surface to volume ratio, while replacing the higher energy {111} polar facets by lower energy {100} non-polar PbSe facets.[25] Further, thermally activated interdiffusion has been observed to convert concentric CdSe/ZnSe core/shell QDs into gradient alloy (Cd,Zn)Se QDs.[26] Similarly, Se-Te interdiffusion across the heterojunction has been observed in linear CdTe/CdSe/CdTe heteronanorods upon thermal annealing at 300 °C, leading to interfacial alloying.[27] Thermally induced diffusion can also drive nanoscale phase separation and reconstruction of the different components of a HNC if the materials are immiscible. For instance, Gold has been observed to diffuse from the inner core of concentric core/shell Au/Ag_2S HNCs to the surface, yielding a hetero-dimer.[28] Conversely, inwards diffusion of Au from the surface to the core of a NC, yielding

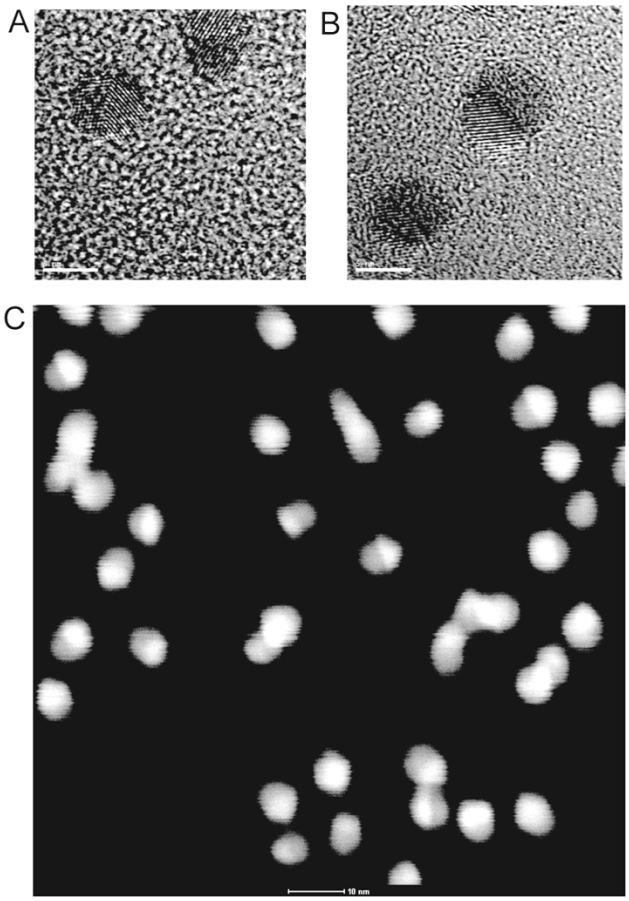

Fig. 4.3 (A,B) HR-TEM images of PbSe/CdSe bi-hemisphere HNCs obtained after annealing of PbSe/CdSe core/shell QDs at 150 °C under vacuum (10^{-11} mbar) in a STM. (C) STEM image of the bi-hemispheres. The brighter and darker parts correspond to PbSe and CdSe, respectively. The scale bars correspond to 5 and 10 nm for (A,B) and (C), respectively.

core/shell HNCs, has been reported for both Au/InAs[29] and Au/PbTe.[30] Thermally induced diffusion processes may also be driven by minimization of interfacial strain, converting concentric core/shell QDs into hetero-dimers.[7] For example, γ-Fe_2O_3-CdS and CdSe-FePt hetero-dimers are obtained by first growing an amorphous and isotropic Fe_2O_3 (or CdSe) shell over a CdS (or FePt) NC.[12, 31] Since the shell is amorphous the lattice mismatch between the two materials is circumvented. However, subsequent thermal

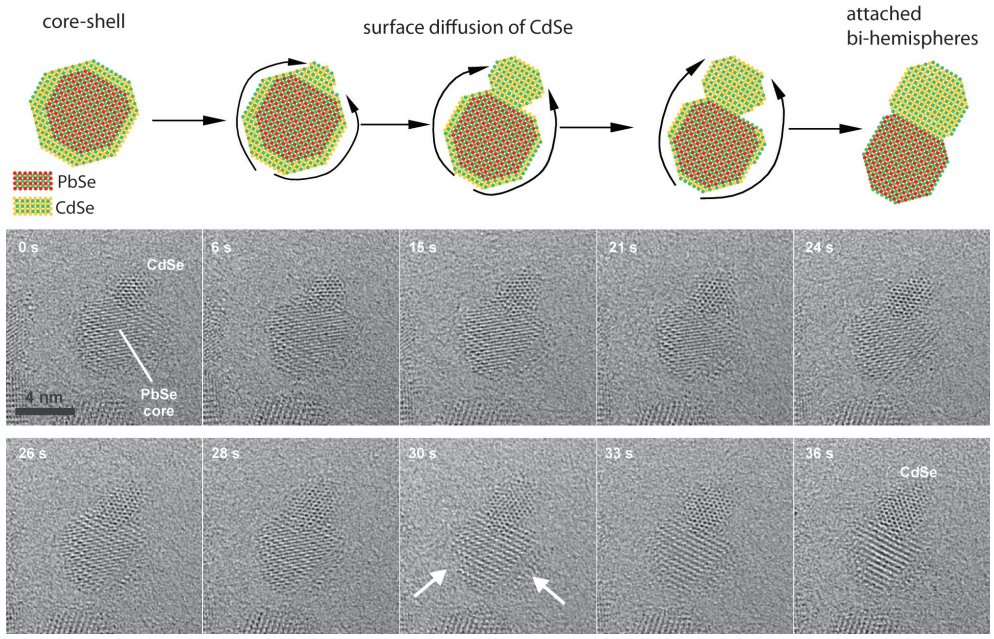

Fig. 4.4 Stills of a real-time *in-situ* HR-TEM recording [32] showing partially the transformation from core/shell to bi-hemisphere heteronanocrystal, at a constant temperature of 200 °C under vacuum (10^{-7} mbar). At the top-right of the PbSe/CdSe core/shell QD (0 s frame), there is a thicker part of the CdSe shell. During the following 36 s, this tiny CdSe nanocrystal grows at the expense of other parts of the CdSe shell. White arrows (at the 30 s frame) point to a few locations at the CdSe shell where the surface becomes discontinuous, while the shell becomes thinner. After 36 s, the top-right CdSe nanocrystal has considerably grown in volume, thereby approaching the hemisphere configuration. The mechanism of the thermally induced structural transformation from core/shell to bi-hemisphere heteronanocrystal is schematically depicted in the top panel.

annealing induces crystallization of the shell, which then retracts to one side of the core NC in order to minimize the interfacial strain induced by the large lattice mismatch between the two materials.[7, 12, 31]

In order to gain insight into the mechanism of the remarkable atomic reconstruction of PbSe/CdSe core/shell HNCs upon *in-situ* thermal annealing, the transformation was also followed in a real-time. Figure 4.4 exhibits some stills of a real time movie showing partly the progressive transformation into bi-hemisphere HNCs. The HNCs showed to be sensitive

to radiation after long exposures to the electron beam, therefore the complete transformation from core/shell to bi-hemisphere HNCs could not be imaged from beginning to end on one single HNC. To rule out the influence of the electron beam, unexposed areas were continuously searched. Nonetheless, the stills presented in Figure 4.4 followed a single HNC for a time sufficiently long to clearly capture the essence of the spectacular atomic reorganization leading to the formation of the bi-hemisphere HNCs. The mechanism of the thermally induced structural reconstruction of the PbSe/CdSe core/shell HNCs into bi-hemisphere HNCs is schematically depicted in Figure 4.4. The transformation starts with the growth of one of the eight CdSe patches that are attached to the {111} facets of the PbSe core. This larger CdSe NC (0s still in Fig. 4.4) continues to grow, while the other CdSe patches shrink. The stills in Figure 4.4 and the real-time movies [32, 33] show that surface diffusion of CdSe units leads to a substantial CdSe mass transfer from one side of the HNC to the other. This demonstrates that the CdSe component of the HNC is very mobile at the atomic scale, even at temperatures as low as 150 °C - 200 °C. It is clear that the consumption of CdSe units by the growing CdSe NC gives rise to a surface diffusion flow which transfers mass from the shrinking segments to the growing one. In response to the extensive structural reorganization of the CdSe part of the HNC, the PbSe core also undergoes a process of reconstruction and reshaping (Fig. 4.4). Due to the small lattice mismatch between PbSe and CdSe (*viz*., ~1%),[8] the Se{111} plane is expected to yield an atomically flat and nearly strain free PbSe/CdSe heterointerface,[9, 18] ruling out strain minimization as the driving force for the atomic reorganization and reconstruction of both the PbSe and the CdSe parts of the HNC. Most likely, the extensive reconstruction of the PbSe/CdSe HNCs is driven by reduction of surface and interfacial energies, since the {111} facets have a relatively high free energy for both rock-salt PbSe[25, 34] and zinc-blende CdSe,[35] being stabilized in colloidal NCs by interaction with coordinating organic ligands.[7, 34-36] In this sense, the bi-hemisphere configuration is energetically favoured, since it contains only a relatively small, single PbSe/CdSe heterointerface, while the core-shell configuration has a large total area of PbSe/CdSe interfaces (the sum of eight Se {111} hetero-interfaces). Moreover, in the core/shell HNCs the outer surface consists only of CdSe oleic acid (OA) capped facets, while after the structural transformation the outer surface consists of both PbSe and CdSe OA capped facets, which can be expected to further lower the total free energy of the HNC due to bond formation between the surface Pb and Cd atoms and the OA ligand molecules. Nevertheless, a complete understanding of this intriguing atomic reconstruction process requires detailed atomistic simulation studies that are beyond the scope of the present work.

To obtain a perfect bi-hemispherical HNC the volumes of PbSe and CdSe must be equal. Depending on the initial core/shell volume ratios, different shapes of HNCs can be formed after thermal annealing (Figure 4.5). The image presents dimer-like PbSe/CdSe HNCs obtained by *in situ* thermal annealing at 200 °C under vacuum (10^{-7} mbar) in the TEM. The

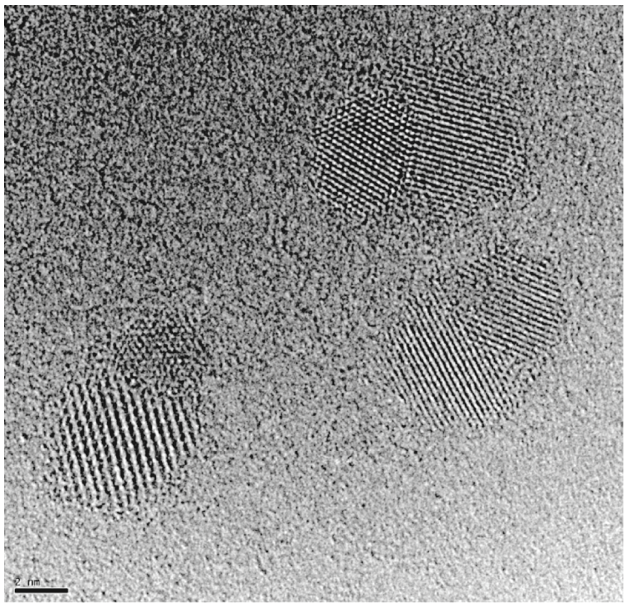

Fig. 4.5 HR-TEM image of dimer-like PbSe/CdSe heteronanocrystals obtained by *in situ* thermal annealing at 200 °C under vacuum (10^{-7} mbar) in the high resolution TEM. The scale bar corresponds to 2 nm.

bottom-left particle clearly shows that the volume of the CdSe shell was significantly larger than that of the PbSe core. The PbSe/CdSe hetero-interface is considerably different from that observed for equal volume bi-hemispheres, in the sense that it is no longer a flat interface, as can be clearly observed for the two particles in the right-hand side of Fig. 4.5.

We have investigated if the thermally induced reconstruction to bi-hemisphere HNCs also occurs under conditions that are technologically more relevant. PbSe/CdSe core/shell QDs were heated for 1 h at 160 °C under vacuum (10^{-6} mbar) in a rotavap (or at 175 °C in a Schlenk line), and were subsequently redissolved in toluene and deposited on TEM grids for imaging. STEM images (Fig. 4.6) and EDX analysis (Fig. 4.7 and Fig. 4.8) show that the initial shape of the HNCs was preserved and that at least part of the PbSe/CdSe core/shell QDs reconstructed into PbSe/CdSe bi-hemisphere HNCs. Notice that the STEM images correspond to different possible 2D projections of the HNCs, due to their different 3D orientation on the substrate (see scheme in Fig. 4.6). This is confirmed by the EDX analyses of different HNCs, which revealed different elemental distribution traces depending on the relative orientation of the HNCs (Fig. 4.7). There are no substantial

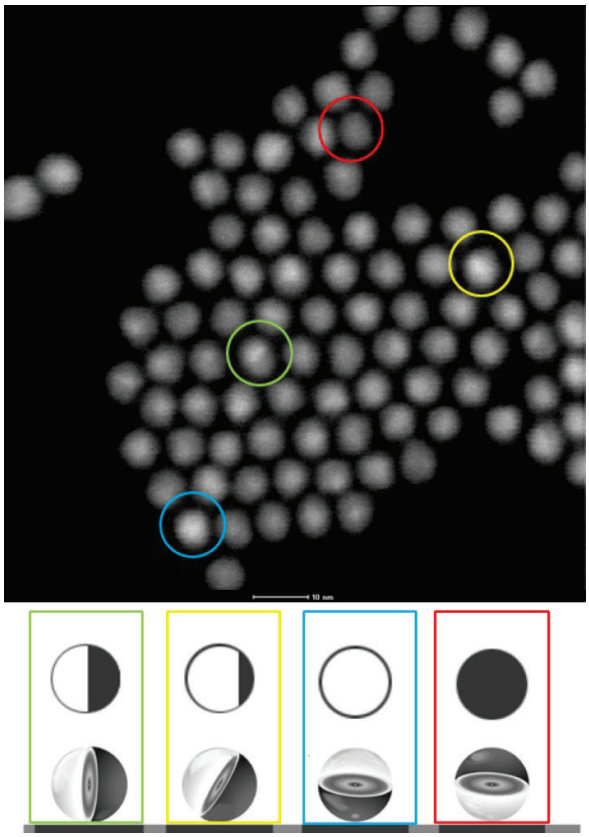

Fig. 4.6 (Top) Scanning TEM image of PbSe/CdSe bi-hemisphere heteronanocrystals obtained by annealing PbSe/CdSe core/shell QDs for 1 h at 160 °C under vacuum (10^{-6} mbar) in a rotary evaporator. The scale bar corresponds to 10 nm. (Bottom) Scheme representing possible 3D orientations of bi-hemisphere particles on the substrate and their 2D projections, respectively. The colour code refers to the particles marked in the STEM image.

differences between the samples treated at 160 °C or 175 °C. It should be noted that the easy redissolution of the thermally treated HNCs in toluene implies that the oleic acid capping layer was at least partly preserved, despite the dramatic atomic reconstruction of the HNCs.

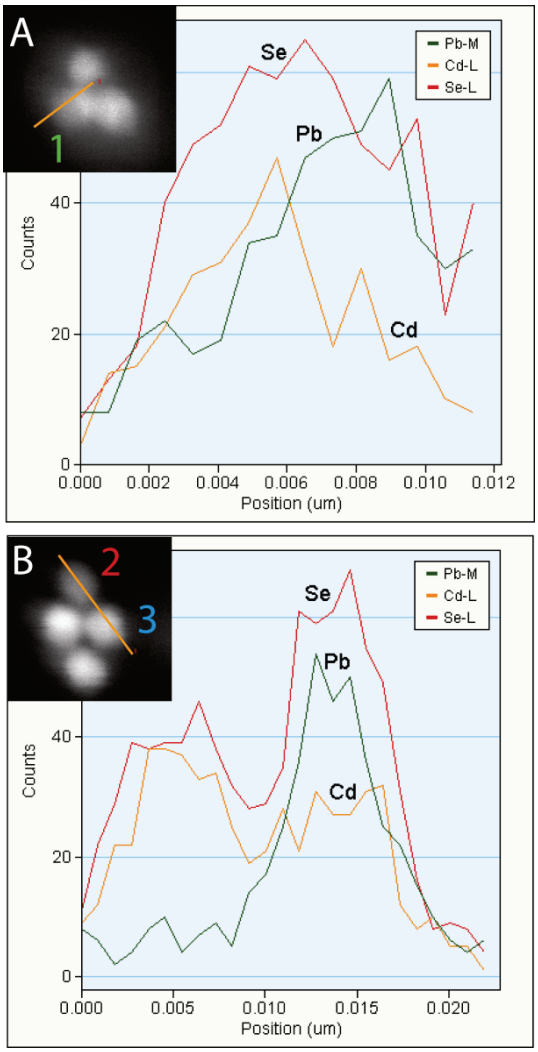

Fig. 4.7 Scanning TEM image (insets) and EDX analysis traces of PbSe/CdSe bi-hemisphere heteronanocrystals obtained by annealing PbSe/CdSe core/shell QDs for 1 h at 175 °C under vacuum (10^{-6} mbar) in a rotary evaporator. The lines in the STEM images indicate the regions through which the EDX analyses were carried out. The colour code is the same used in Figure 4.6, and indicates different possible orientations of the heteronanocrystals on the substrate. (A) Heteronanocrystal oriented in such a way that its bi-hemispherical configuration is clearly observed both in STEM image and in the EDX trace. (B) Two heteronanocrystals oriented with the PbSe hemisphere facing down (2) or at an angle with respect to the substrate (3).

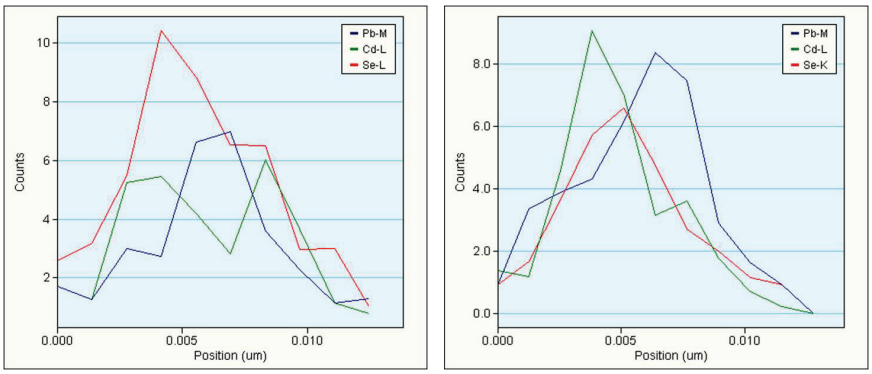

Fig. 4.8 EDX analysis of two different PbSe/CdSe HNCs heated for 1.5 h at 160°C under vacuum (10^{-6} mbar) in a Schlenk line.

High-resolution TEM images (Fig. 4.9) show that some of the QDs with unequal core/shell volume ratios undergo a reconstruction into "peacock eye" shaped HNCs (Fig. 4.9C), in which small PbSe cores are situated at one side of HNCs, partially surrounded by a thicker and uneven CdSe shell. Depending on the orientation of the HNC with respect to the substrate (*viz*., core at the side, at the top or at the bottom of the nanoparticle), the PbSe core will be observed either at the side or at the centre of the imaged HNC (as, *e.g*., in Fig. 4.9A,B). The PbSe/CdSe hetero-interface in these HNCs has a complex geometry, involving a variety of different orientations of the Se plane. Further, some of the PbSe cores still possess octahedral-like shapes, as clearly seen in the [100] projection (Fig. 4.9B).

Interestingly, PbSe/CdSe core/shell QDs with unequal PbSe and CdSe volumes preserve their total spherical shape (bi-hemispherical or "peacock eye"-shaped) after thermal annealing under vacuum (10^{-6} mbar) in the rotavap or Schlenk line, but reconstruct to elongated, dimer-like HNCs after *in-situ* annealing at 200 °C in the high-resolution TEM (Fig. 4.5). A possible explanation is that the *in-situ* heating in the HR-TEM is more effective and therefore leads to full reconstruction, producing dimer-like HNCs when the PbSe and CdSe volumes are unequal, while annealing in the rotavap leads to an intermediate step of reconstruction ("peacock eye" HNCs) due to the lower temperatures used (160 – 175 °C).

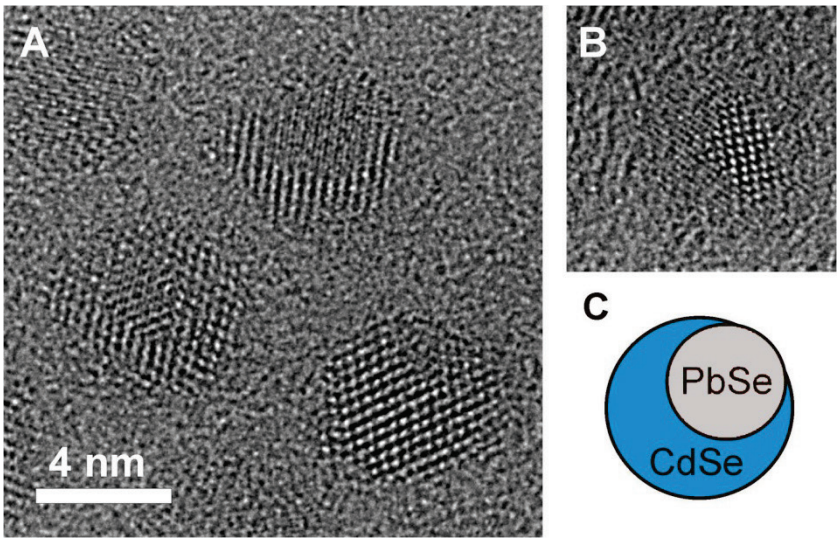

Fig. 4.9 High-resolution TEM images of PbSe/CdSe HNCs obtained by annealing PbSe/CdSe core/shell QDs for 1 h at 160 °C under vacuum (10^{-6} mbar) in a rotary evaporator. (A) Several bi-hemisphere HNCs in different projections. In many cases, a larger and uneven CdSe shell and a smaller Pbse core at the side of the nanoparticle can be distinguished. (B) PbSe/CdSe bi-hemisphere HNC in a [100] projection. (C) Schematic cross-sectional view of the "peacock eye"-like bi-hemispherical HNC produced by thermal annealing in a rotary evaporator. The smaller PbSe core is present at one side of the particle, partly surrounded by a much larger and uneven CdSe shell. Depending on the orientation of the particle, the core can be observed *in projection* either at the side or at the centre of the imaged HNC (as in A,B).

The annealing temperature is thus an important parameter in the reconstruction of the PbSe/CdSe core/shell QDs into bi-hemisphere HNCs. The results presented above indicate that a temperature of 150 – 200 °C (depending on the heating method) is required to form PbSe/CdSe bi-hemisphere HNCs. These temperatures are sufficiently high to induce atom-by-atom structural reconstruction of the HNCs, but are not enough to remove the oleic acid (OA) ligands from the HNC surface. Additional experiments were performed by *in situ* heating in the high resolution TEM at 300 °C and 400 °C (TEM images not shown). At 300 °C the bi-hemisphere HNCs start to coalesce, indicating that the OA capping molecules are beginning to detach from the surface. Upon further annealing at 400 °C, a very strong agglomeration is observed whereby the HNCs attach into large polycrystalline agglomerates. The PbSe parts of the HNCs separate and coalesce into larger NCs, which

reconstruct into cubic shapes. In this way, the {110} and {100} PbSe surfaces, which possess lower surface energies,[34] become dominant, while the Se{111} interfacial planes vanish.

These results show that the presence of capping molecules at the surface of the HNCs is essential to prevent coalescence and inter-particle ripening during the thermally induced reconstruction, suggesting that the nature of the capping molecules may also play a crucial role in the formation of the bi-hemisphere HNCs. The oleic acid (OA) molecules used in this work as ligands bind tightly to the metal atoms at NC surface, and remain bound to the surface even after thermal annealing of the HNCs. The integrity of the OA capping layer in the thermally annealed HNCs is clearly demonstrated by the fact that the PbSe/CdSe HNCs are still readily soluble in toluene after being heated at 160 °C (or 175 °C) under vacuum (10^{-6} mbar) for 1 h. This shows that the coordinating bond between the carboxylic head group of the OA molecules and the metal atoms (Pb and Cd) at the HNC surface is much stronger than the ligand-ligand or ligand-TEM grid interactions. It is well known that ligands modify the surface free energies of the different crystallographic facets of NCs, therefore playing a decisive role in the faceting and shape of colloidal NCs.[7, 36] It is thus likely that the presence of the OA capping layer during the structural reconstruction is necessary for the preservation of the HNC's original (nearly) spherical shape, and also to prevent particle coalescence and interparticle mass transport.

The important role played by the OA capping molecules during the thermally induced structural reconstruction of the HNCs would suggest that this process could also take place in colloidal suspensions. However, our investigations clearly established that the reconstruction of PbSe/CdSe core/shell QDs into bi-hemisphere HNCs takes place only when the thermal annealing is carried out under vacuum. Heating of colloidal suspensions of PbSe/CdSe core/shell QDs in ODE, TOPO, TOP or HDA invariably resulted in aggregation of the HNCs followed by ripening and/or coalescence. DPE proved to be a better solvent, producing stable colloidal suspensions over a wide temperature range. Nevertheless, thermal annealing of colloidal suspensions of PbSe/CdSe core/shell QDs in DPE also failed to produce PbSe/CdSe bi-hemisphere HNCs. Heating in DPE at temperatures below 200 °C does not induce any observable change in the HNCs, which remain stable in suspension and retain their core/shell structures (Fig. 4.10). The overall shape and size dispersion remain the same, demonstrating that the thermal stability of PbSe/CdSe core/shell QDs is much higher than that of PbSe QDs, which are known to undergo pronounced interparticle (Ostwald) ripening at temperatures as low as 80 °C.[8] Annealing at temperatures in the range 200 – 240 °C induce changes in the HNCs structure, CdSe parts of the HNC start to separate and single-composition PbSe and CdSe NCs are observed, alongside with PbSe/CdSe HNCs (Figures 4.11 and 4.12). However, the structure

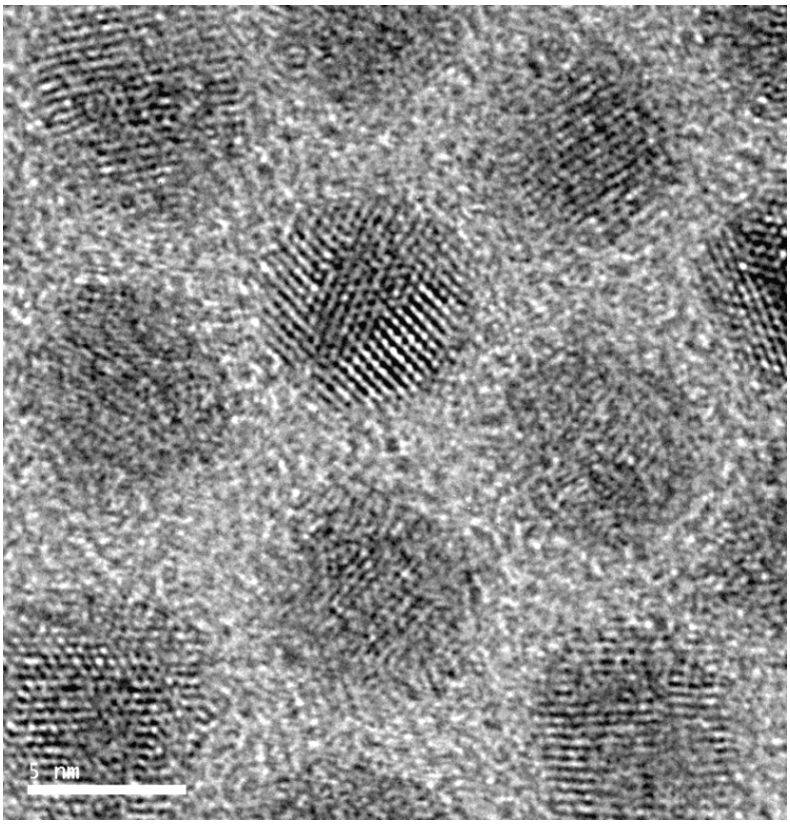

Fig. 4.10 HR-TEM image of PbSe/CdSe HNCs after heating in diphenylether at 150 °C. The HNCs still possess a core/shell structure. The scale bar correspond to 5 nm.

of the remaining PbSe/CdSe HNCs is difficult to determine. Although the typical core/shell structure is no longer observed, bi-hemisphere or dimer-type HNCs are also not evident (Fig. 4.11). Annealing at 240 °C in DPE leads to a drastic destabilization of the HNCs, which undergo a pronounced coalescence and Ostwald ripening process, resulting in a very polydisperse distribution of NCs (Fig. 4.13). These experiments show that vacuum is essential during the thermally induced reconstruction process.

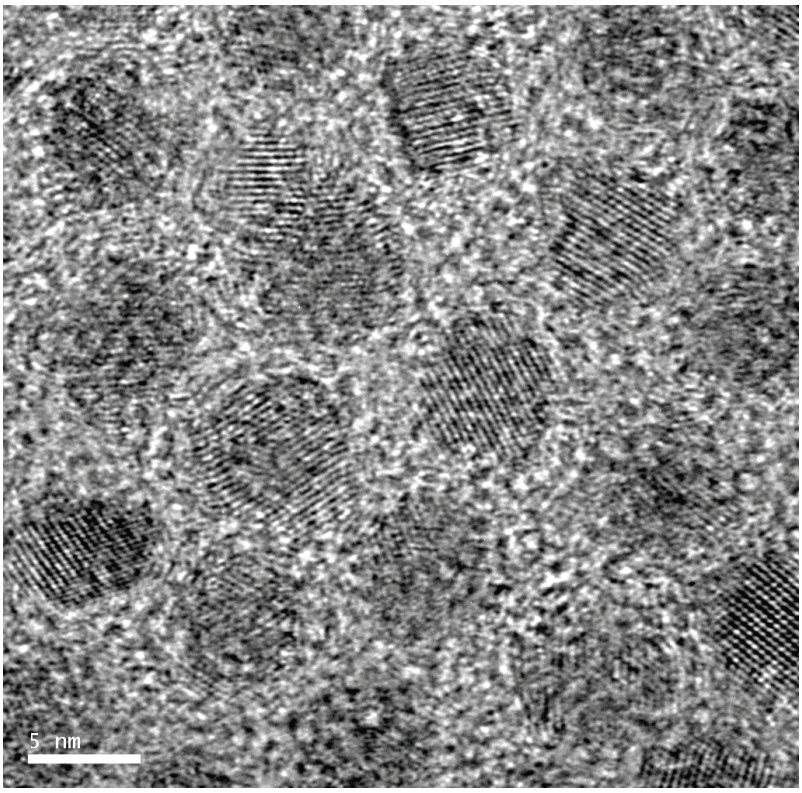

Fig. 4.11 HR-TEM image of PbSe/CdSe HNCs after heating in diphenylether at 200 °C. Core/shell structures are difficult to identify, but nevertheless bi-hemisphere HNCs are also not present. The scale bar corresponds to 5 nm.

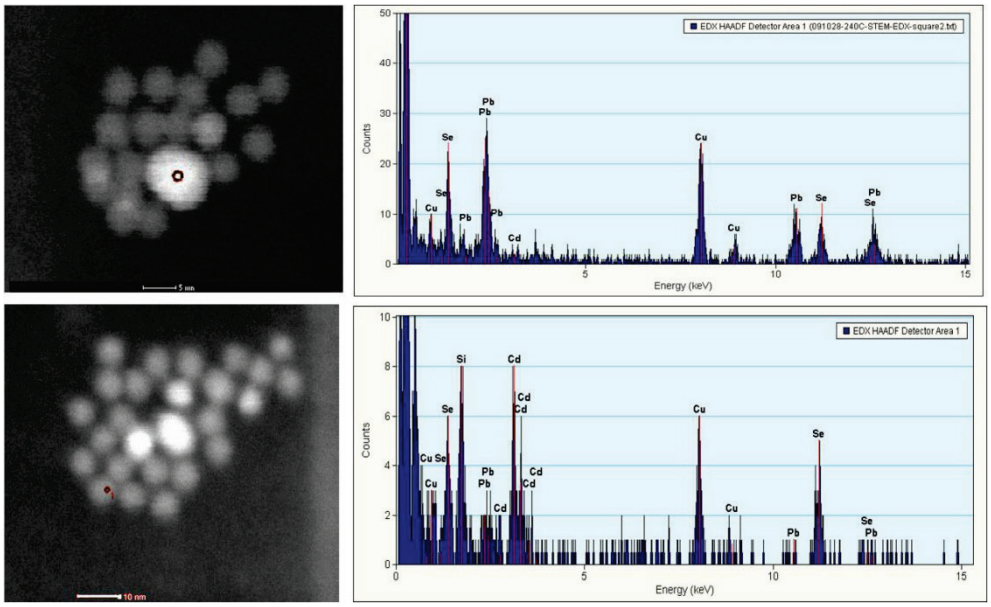

Fig. 4.12 STEM images (right) and EDX analysis (left) of PbSe/CdSe HNCs heated in diphenylether at 220 °C. The red spots indicate the area on which the EDX analyses were done.

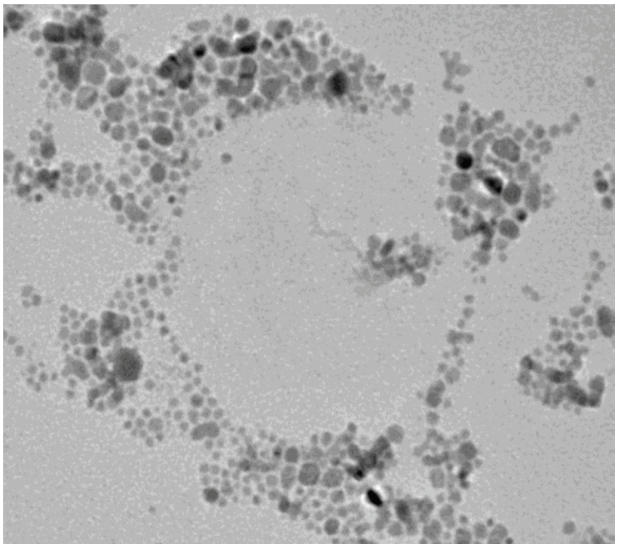

Fig. 4.13 TEM image of PbSe/CdSe HNCs after heating in diphenylether at 240 °C.

The thermally induced structural reconstruction of the PbSe/CdSe HNCs leads to pronounced changes in their optical properties, even though the total amount of CdSe and PbSe per HNC remains constant. Figure 4.14 compares the photoluminescence (PL) and absorption spectra of a colloidal suspension of PbSe/CdSe core/shell QDs (5.6 nm total diameter and 3.6 nm diameter core) prior to (Fig. 4.14A) and after (Fig. 4.14B) thermal annealing at 160 °C under vacuum (10^{-6} mbar) in a rotavap. As discussed above, this thermal treatment converts the core/shell QDs into bi-hemisphere HNCs (Fig. 4.9). Before discussing the changes induced by this structural reconstruction on the optical properties of the HNCs, it is useful to address the properties of the PbSe/CdSe core/shell QDs. These properties have been discussed in detail in the literature,[8, 19] (and in Chapter 2 of this thesis) therefore we will here only summarize the most important aspects. As mentioned above, the PbSe/CdSe core/shell QDs investigated in this work were prepared by a Pb for Cd ion-exchange reaction, in which the total diameter and shape of the QDs are preserved, while the PbSe cores progressively shrink as the CdSe shell grows. As an illustrative example of the evolution of the optical properties of PbSe/CdSe core/shell QDs with increasing reaction time, Figure 4.15 presents the absorption and emission spectra of the parent PbSe QDs (diameter 3.7 nm), and of the PbSe/CdSe core/shell QDs obtained from the latter after 5 and 30 min of Pb/Cd ion exchange (PbSe core diameter of 3.2 and 2.3 nm, respectively). The absorption spectrum of the parent PbSe QDs shows two sharp absorption peaks, assigned to the $1S_h$-$1S_e$ and $1P_h$-$1P_e$ transitions, respectively.[19] The $1S_h$-$1S_e$ emission peak is located at 0.88 eV, slightly red shifted with respect to the corresponding absorption peak and has a full width at half maximum (FWHM) of 100 meV. The in-growth of a CdSe shell leads to a reduction of the PbSe core size, and markedly changes the optical properties. The lowest-energy absorption and the emission peaks shift to higher energies and become broader with increasing duration of Pb/Cd ion-exchange. At room temperature, the maximum of the emission peak shifts from 0.88 eV (3.7 nm PbSe QD, Fig. 4.15A), to 0.95 eV (3.2 nm PbSe core, Fig. 4.15B) and to 1.06 eV (2.3 nm PbSe core, Fig. 4.15C). The blue-shift of the absorption and emission spectra can be ascribed to the decreasing size of the remaining PbSe core in the PbSe/CdSe core/shell HNC, under the understanding that the exciton remains confined in the PbSe core.[19] Resonant scanning tunnelling microscopy on single PbSe/CdSe core/shell QDs[20] and optical spectroscopic investigations[19] indicate that these HNCs can best be described as a type-I system (or Type-$I^{1/2}$), in which the s-electron wave function is centred in the PbSe core, (or extended into the CdSe shell), and the hole wave function is completely confined into the core.[19, 20]

We turn now to the changes in the optical spectra induced by structural reconstruction of the PbSe/CdSe core/shell QDs into bi-hemisphere HNCs. The most evident differences occur in the absorption (and photoluminescence excitation, PLE) spectra (Figures 4.14 and 4.16). The lowest energy exciton transition in the absorption spectrum of the core/shell QDs is observed at 0.97 eV (Fig. 4.14A and Fig. 4.16A). This peak is followed by

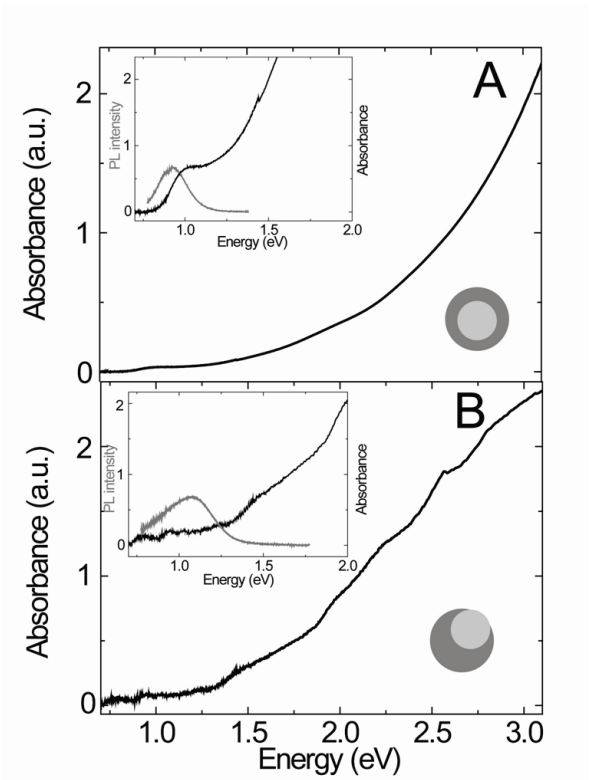

Fig. 4.14 Absorption spectra of: (A) PbSe/CdSe core/shell QDs with a total diameter of 5.6 nm and 3.6 nm diameter core; and (B) PbSe/CdSe "peacock eye"-like bi-hemisphere HNCs obtained by thermal annealing of the sample shown in (A) at 160 °C under vacuum (10^{-6} mbar) in a rotary evaporator (see Fig. 4.9 for illustrative HR-TEM images). Insets show the photoluminescence spectra (grey lines) in combination with the absorption spectra in the 0.8 to 2.0 eV energy range.

two peaks at 1.1 eV and 1.25 eV (Fig. 4.14A and Fig. 4.16A), which are assigned to exciton transitions in the PbSe core.[19] At energies above ~1.3 eV the absorption spectrum of the core/shell QDs consists of a featureless band which increases in intensity with increasing energies (Fig. 4.14A). In contrast, the absorption spectrum of the "peacock eye"-like bi-hemisphere HNCs (Fig. 4.14B) displays a number of well-defined peaks at higher energies (*viz*., 1.5, 2.0, 2.3, 2.5 and 2.8 eV). The three highest energy peaks are particularly clear in the PLE spectrum of the bi-hemisphere HNCs (Fig. 4.16B). The higher spectral resolution observed in the PLE spectra (Fig. 4.16) is due to a number of reasons.[11] First, only the

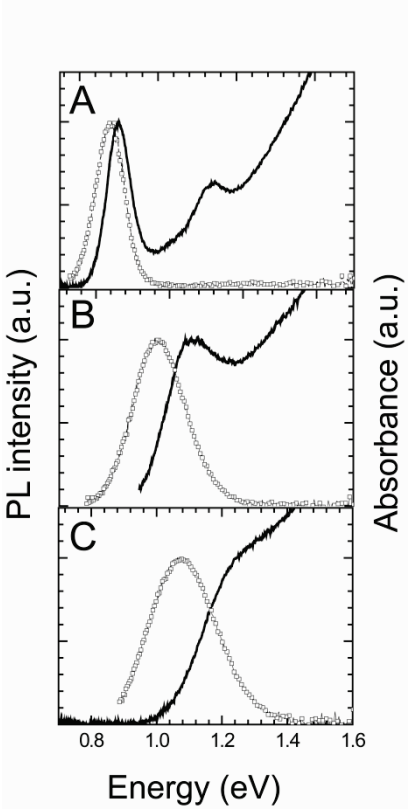

Fig. 4.15 Room temperature absorption (solid line) and photoluminescence spectra (circles) of the parent PbSe NCs (3.7 nm in diameter) (A), and of PbSe/CdSe core/shell quantum dots obtained from the latter after 5 min (B, 3.2 nm diameter core) and 30 min (C, 2.3 nm diameter core) of Pb/Cd ion-exchange. The total diameter of the parent PbSe NC is preserved during the ion-exchange.

emitting HNCs contribute to the PLE spectra, while the absorption spectra contains contributions from all absorbing species in the volume sampled (*i.e.*, non-emitting HNCs, impurities, surfactants, etc.). Second, the PLE technique allows a narrow portion of the ensemble of emitting HNCs to be spectrally selected, thereby minimizing the impact of size and shape inhomogeneities. Interestingly, the highest energy peak positions are in good agreement with the four lowest energy exciton absorption transitions of ~3.7 nm diameter colloidal CdSe QDs.[15] This diameter is comparable to the dimensions of the CdSe part of the PbSe/CdSe bi-hemisphere HNCs, and therefore the peaks at 2.0, 2.3, 2.5 and 2.8 eV can

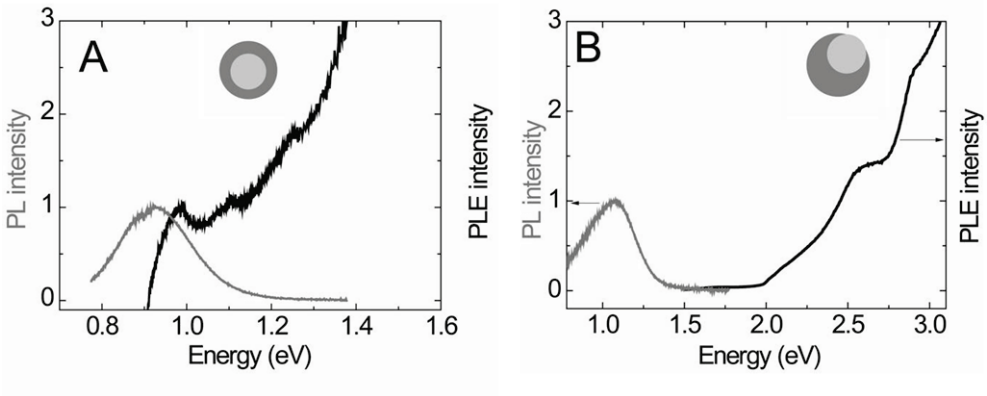

Fig. 4.16 Photoluminescence (PL, grey line) and PL Excitation (PLE, black line) spectra of: (A) PbSe/CdSe core/shell QDs with a total diameter of 5.6 nm and 3.6 nm diameter core; and (B) PbSe/CdSe "peacock eye"-like bi-hemisphere HNCs obtained by thermal annealing of the sample shown in (A) at 160 °C under vacuum (10^{-6} mbar) in a rotary evaporator (see Figure 4.9 for illustrative HR-TEM images).

be assigned to CdSe exciton absorption transitions. This is in remarkable contrast to the case of PbSe/CdSe core/shell QDs, for which no clear indications of CdSe exciton transitions are observed in the absorption spectra. Figure 4.14 clearly shows that the relative intensity of the higher energy transitions is much higher for the PbSe/CdSe bi-hemisphere HNCs (Fig. 4.14B) than for the PbSe/CdSe core/shell QDs, suggesting that the oscillator strengths of the CdSe transitions increase after the structural reorganization. This can be ascribed to the fact that the CdSe part of the HNC has reconstructed from a thin (and possibly discontinuous) shell into a single and larger NC, in which the strength of the quantum confinement is reduced. This shifts the CdSe transitions to lower energies and increases their intensities, since the oscillator strengths of the excitonic transitions are proportional to the volume of the semiconductor NC.[15]

PbSe transitions are not clearly observed in the absorption (or PLE) spectra of PbSe/CdSe bi-hemisphere HNCs, possibly due to the very low concentration of the colloidal suspension used for the measurements. Nevertheless, a tail can be observed at energies below 1.9 eV in the absorption spectrum (Fig. 4.14B), which can be assigned to exciton transitions of the PbSe part of the HNC. Lower energy transitions cannot be clearly observed because the signal to noise ratio below 1.5 eV is very poor. The much weaker intensity of the PbSe transitions can be understood considering the smaller volume of the

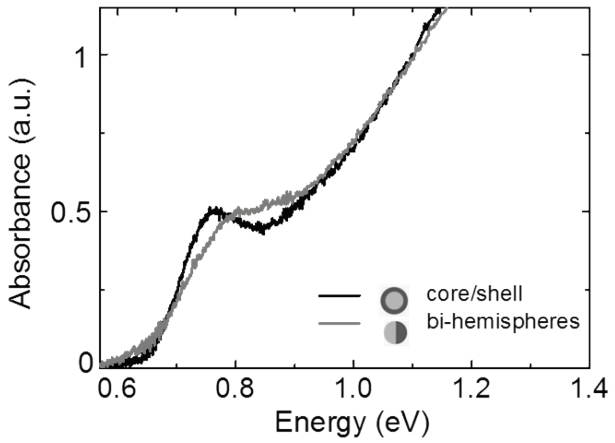

Fig. 4.17 Absorption spectra of PbSe/CdSe core/shell QDs with a total diameter of 7.6 nm (black line) and PbSe/CdSe bi-hemisphere HNCs (grey line) obtained by thermal annealing of the sample shown in 160 °C under vacuum (10^{-6} mbar) in a rotary evaporator.

PbSe part of the HNCs and the much smaller oscillator strengths of the PbSe exciton transitions with respect to those of CdSe QDs. A rough estimate based on the radiative lifetimes of PbSe and CdSe QDs (*viz*., ~1 μs,[37] and ~20 ns,[15] respectively) indicates that the PbSe exciton transitions should be two orders of magnitude weaker than those of CdSe QDs for similarly sized NCs. The use of more concentrated PbSe/CdSe bi-hemisphere HNC solutions allowed us to observe the lower energy absorption transitions as well (Fig. 4.17). Figure 4.17 shows the absorption spectrum of PbSe/CdSe bi-hemisphere HNCs together with the parent PbSe/CdSe core/shell samples with 7.6 nm of the total diameter. It can be seen that the thermal reconstruction into bi-hemispheres does not lead to considerable changes in the PbSe NC transitions, since the volume of PbSe stays constant during the transformation. The small blue shift of *ca.* 40 meV can be assigned to the changes in the PbSe core shape, which is no longer spherical, and the reduction of the CdSe shell, what may cause stronger confinement of electron wave function into the PbSe part of the HNC.

The structural reconstruction of the PbSe/CdSe HNCs after the thermal annealing has also a pronounced influence on their emission properties, since the PL peak is observed to shift from 0.92 eV (Fig. 4.14A) to 1.07 eV (Fig. 4.14B), while the FWHM doubles. The PL quantum efficiency does not seem to be affected. Although it is clear that the emission cannot originate from intrinsic CdSe transitions, its exact nature is not yet understood. Recent investigations have shown that the emitting state in PbSe/CdSe core/shell QDs is

different in nature from the lowest energy absorption transition, which is still primarily localized in the PbSe core[19] (see also Chapter 2 of this thesis). In contrast, the emitting transition in PbSe/CdSe core/shell QDs has a much lower oscillator strength than that in PbSe QDs and originates from lower energy states that are different from the lowest energy absorbing states, possibly due to the partial extension of the electron wavefunction into the CdSe shell.[19] In this context, the blue shift of the PL peak after the reorganization of the PbSe/CdSe core/shell HNC into a bi-hemisphere HNC may be ascribed to the fact that the electron wavefunction becomes more strongly confined, since a shell is no longer present. The increase in the linewidth is probably due to an increase in the size and shape dispersion of the PbSe cores after the transformation. It is also possible that the structural reconstruction alters the localization regime of the photoexcited carriers, leading to the formation of a dipolar spatially indirect exciton, but the present results are as yet insufficient to allow definitive conclusions in this respect. Further work is needed in order to shed light on the nature of the emitting state and on the detailed electronic structure of PbSe/CdSe bi-hemisphere hetero-nanocrystals.

4.4 Conclusions

Upon thermal annealing under vacuum colloidal PbSe/CdSe core/shell quantum dots are observed to undergo a dramatic structural and morphological reconstruction whereby the PbSe core and the CdSe shell reorganize into hemispheres joined by a common {111} Se plane. The reconstruction involves primarily the reorganization of the CdSe component, which starts migrating from one side to the other side of the HNC at temperatures between 150 °C to 200 °C. The exact temperature required to form the bi-hemisphere HNCs depends on the heating method (*i.e.*, *in-situ* heating in the HR-TEM, heating in a STM, or heating in a rotavap). Our results show that the presence of oleic acid capping molecules at the surface of the HNCs during the thermally induced reconstruction is essential to prevent coalescence and inter-particle ripening. Nevertheless, the reconstruction takes place only when the thermal annealing is carried out under vacuum. A complete understanding of this intriguing atomic reconstruction process will require detailed atomistic simulation studies of the evolution of the free energy of oleic acid capped PbSe/CdSe core/shell quantum dots under thermal annealing conditions. The structural reconstruction of the PbSe/CdSe HNCs has also a pronounced effect on their optical properties, affecting both the absorption and emission transitions. However, further work is needed in order to unravel the detailed electronic structure of PbSe/CdSe bi-hemisphere HNCs and to elucidate the nature of their emitting state.

References

1. Sashchiuk, A., L. Amirav, M. Bashouti, M. Krueger, U. Sivan, and E. Lifshitz, *PbSe Nanocrystal Assemblies: Synthesis and Structural, Optical, and Electrical Characterization.* Nano Letters, 2004. **4**(1): p. 159-165.
2. Wise, F.W., *Lead Salt Quantum Dots: the Limit of Strong Quantum Confinement.* Accounts of Chemical Research, 2000. **33**(11): p. 773-780.
3. Moreels, I., K. Lambert, D. De Muynck, F. Vanhaecke, D. Poelman, J.C. Martins, G. Allan, and Z. Hens, *Composition and Size-Dependent Extinction Coefficient of Colloidal PbSe Quantum Dots.* Chemistry of Materials, 2007. **19**(25): p. 6101-6106.
4. Law, M., M.C. Beard, S. Choi, J.M. Luther, M.C. Hanna, and A.J. Nozik, *Determining the Internal Quantum Efficiency of PbSe Nanocrystal Solar Cells with the Aid of an Optical Model.* Nano Letters, 2008. **8**(11): p. 3904-3910.
5. Rauch, T., M. Boberl, S.F. Tedde, J. Furst, M.V. Kovalenko, G. Hesser, U. Lemmer, W. Heiss, and O. Hayden, *Near-infrared imaging with quantum-dot-sensitized organic photodiodes.* Nat Photon, 2009. **3**(6): p. 332-336.
6. Sukhovatkin, V., S. Hinds, L. Brzozowski, and E.H. Sargent, *Colloidal Quantum-Dot Photodetectors Exploiting Multiexciton Generation.* Science, 2009. **324**(5934): p. 1542-1544.
7. de Mello Donegá, C., *Synthesis and properties of colloidal heteronanocrystals.* Chemical Society Reviews, 2011. **40**: p. 1512.
8. Pietryga, J.M., D.J. Werder, D.J. Williams, J.L. Casson, R.D. Schaller, and V.I. Klimov, *Utilizing the Lability of Lead Selenide to Produce Heterostructured Nanocrystals with Bright, Stable Infrared Emission.* Journal of the American Chemical Society, 2008. **130**(14): p. 4879-4885.
9. Lambert, K., B.D. Geyter, I. Moreels, and Z. Hens, *PbTe|CdTe Core|Shell Particles by Cation Exchange, a HR-TEM study.* Chemistry of Materials, 2009. **21**(5): p. 778-780.
10. Sykora, M., A.Y. Koposov, J.A. McGuire, R.K. Schulze, O. Tretiak, J.M. Pietryga, and V.I. Klimov, *Effect of Air Exposure on Surface Properties, Electronic Structure, and Carrier Relaxation in PbSe Nanocrystals.* ACS Nano, 2010. **4**(4): p. 2021-2034.
11. de Mello Donegá, C., *Formation of nanoscale spatially indirect excitons: Evolution of the type-II optical character of CdTe/CdSe heteronanocrystals.* Physical Review B, 2010. **81**(16): p. 165303.
12. Cozzoli, P.D., T. Pellegrino, and L. Manna, *Synthesis, properties and perspectives of hybrid nanocrystal structures.* Chemical Society Reviews, 2006. **35**(11): p. 1195-1208.
13. Yin, Y. and A.P. Alivisatos, *Colloidal nanocrystal synthesis and the organic-inorganic interface.* Nature, 2005. **437**(7059): p. 664-670.
14. Springholz, G. and G. Bauer, *Molecular beam epitaxy of IV-VI semiconductor hetero- and nano-structures.* physica status solidi (b), 2007. **244**(8): p. 2752-2767.
15. de Mello Donegá, C. and R. Koole, *Size Dependence of the Spontaneous Emission Rate and Absorption Cross Section of CdSe and CdTe Quantum Dots.* The Journal of Physical Chemistry C, 2009. **113**(16): p. 6511-6520.
16. Martinez, G., M. Schlüter, and M.L. Cohen, *Electronic structure of PbSe and PbTe. Band structures, densities of states, and effective masses.* Physical Review B, 1975. **11**(2): p. 651.
17. Dalven, R., *Calculation of effective masses in cubic CdS and CdSe.* physica status solidi (b), 1971. **48**(1): p. K23-K26.
18. Heiss, W., E. Kaufmann, M. Böberl, T. Schwarzl, G. Springholz, G. Hesser, F. Schäffler, K. Koike, H. Harada, M. Yano, R. Leitsmann, L.E. Ramos, and F. Bechstedt, *Highly luminescent nanocrystal quantum dots fabricated by lattice-type mismatched epitaxy.* Physica E: Low-dimensional Systems and Nanostructures, 2006. **35**(2): p. 241-245.

19. De Geyter, B., Y. Justo, I. Moreels, K. Lambert, P.F. Smet, D. Van Thourhout, A.J. Houtepen, D. Grodzinska, C. de Mello Donega, A. Meijerink, D. Vanmaekelbergh, and Z. Hens, *The Different Nature of Band Edge Absorption and Emission in Colloidal PbSe/CdSe Core/Shell Quantum Dots.* ACS Nano, 2011. **5**(1): p. 58-66.
20. Swart, I., Z. Sun, D.l. Vanmaekelbergh, and P. Liljeroth, *Hole-Induced Electron Transport through Core-Shell Quantum Dots: A Direct Measurement of the Electron-Hole Interaction.* Nano Letters, 2010. **10**(5): p. 1931-1935.
21. Xu, S.J., X.C. Wang, S.J. Chua, C.H. Wang, W.J. Fan, J. Jiang, and X.G. Xie, *Effects of rapid thermal annealing on structure and luminescence of self-assembled InAs/GaAs quantum dots.* Applied Physics Letters, 1998. **72**(25): p. 3335-3337.
22. Koike, K., T. Itakura, T. Hotei, M. Yano, H. Groiss, G. Hesser, and F. Schäffler, *Thermal precipitation of self-organized PbTe quantum dots in CdTe host matrix.* physica status solidi (c), 2008. **5**(9): p. 2746-2749.
23. Houtepen, A.J., R. Koole, D. Vanmaekelbergh, J. Meeldijk, and S.G. Hickey, *The Hidden Role of Acetate in the PbSe Nanocrystal Synthesis.* Journal of the American Chemical Society, 2006. **128**(21): p. 6792-6793.
24. van Huis, M.A., N.P. Young, G. Pandraud, J.F. Creemer, D. Vanmaekelbergh, A.I. Kirkland, and H.W. Zandbergen, *Atomic Imaging of Phase Transitions and Morphology Transformations in Nanocrystals.* Advanced Materials, 2009. **21**(48): p. 4992-4995.
25. van Huis, M.A., L.T. Kunneman, K. Overgaag, Q. Xu, G. Pandraud, H.W. Zandbergen, and D.l. Vanmaekelbergh, *Low-Temperature Nanocrystal Unification through Rotations and Relaxations Probed by in Situ Transmission Electron Microscopy.* Nano Letters, 2008. **8**(11): p. 3959-3963.
26. Zhong, X., M. Han, Z. Dong, T.J. White, and W. Knoll, *Composition-Tunable ZnxCd1-xSe Nanocrystals with High Luminescence and Stability.* Journal of the American Chemical Society, 2003. **125**(28): p. 8589-8594.
27. Koo, B. and B.A. Korgel, *Coalescence and Interface Diffusion in Linear CdTe/CdSe/CdTe Heterojunction Nanorods.* Nano Letters, 2008. **8**(8): p. 2490-2496.
28. Yang, J. and J.Y. Ying, *Diffusion of Gold from the Inner Core to the Surface of Ag2S Nanocrystals.* Journal of the American Chemical Society, 2010. **132**(7): p. 2114-2115.
29. Mokari, T., A. Aharoni, I. Popov, and U. Banin, *Diffusion of Gold into InAs Nanocrystals.* Angewandte Chemie International Edition, 2006. **45**(47): p. 8001-8005.
30. Franchini, I.R., G. Bertoni, A. Falqui, C. Giannini, L.W. Wang, and L. Manna, *Colloidal PbTe-Au nanocrystal heterostructures.* Journal of Materials Chemistry, 2010. **20**(7): p. 1357-1366.
31. Zanella, M., A. Falqui, S. Kudera, L. Manna, M.F. Casula, and W.J. Parak, *Growth of colloidal nanoparticles of group II-VI and IV-VI semiconductors on top of magnetic iron-platinum nanocrystals.* Journal of Materials Chemistry, 2008. **18**(36): p. 4311-4317.
32. *http://www.rsc.org/suppdata/jm/c0/c0jm04458j/c0jm04458j.mov*.
33. *http://www.rsc.org/suppdata/jm/c0/c0jm04458j/c0jm04458j_2.mov*.
34. Fang, C., M.A. van Huis, D.l. Vanmaekelbergh, and H.W. Zandbergen, *Energetics of Polar and Nonpolar Facets of PbSe Nanocrystals from Theory and Experiment.* ACS Nano, 2010. **4**(1): p. 211-218.
35. Manna, L., Wang, R. Cingolani, and A.P. Alivisatos, *First-Principles Modeling of Unpassivated and Surfactant-Passivated Bulk Facets of Wurtzite CdSe: A Model System for Studying the Anisotropic Growth of CdSe Nanocrystals.* The Journal of Physical Chemistry B, 2005. **109**(13): p. 6183-6192.
36. Schapotschnikow, P., M.A. van Huis, H.W. Zandbergen, D.l. Vanmaekelbergh, and T.J.H. Vlugt, *Morphological Transformations and Fusion of PbSe Nanocrystals Studied Using Atomistic Simulations.* Nano Letters, 2010. **10**(10): p. 3966-3971.

37. Oron, D., A. Aharoni, C. de Mello Donega, J. van Rijssel, A. Meijerink, and U. Banin, *Universal Role of Discrete Acoustic Phonons in the Low-Temperature Optical Emission of Colloidal Quantum Dots.* Physical Review Letters, 2009. **102**(17): p. 177402.

5

Electronic Structure of PbSe/CdSe Bi-hemisphere Heteronanocrystals Measured by STM

This chapter presents a scanning tunneling microscopy (STM) and spectroscopy (STS) study of PbSe/CdSe bi-hemisphere heteronanocrystals, created upon in-situ heating in the STM vacuum chamber. Our data show that depending on the orientation of the PbSe/CdSe bi-hemispheres in the double barrier tunneling junction (DBTJ), different spectra can be observed with characteristic features for PbSe and CdSe semiconductor quantum dots.

5.1 Introduction

Lead chalcogenide nanocrystals NC (*e.g.,* composed of PbSe, PbS or PbTe) have recently received a lot of attention due to their optical properties in the near-infrared (NIR) spectral range.[1-7] The small effective masses and large Bohr exciton radius leads to strong confinement of the charge carrier wave functions. As a consequence, the properties of these nanocrystal quantum dots can be easily tuned by simply changing the size of the NC. In general, lead chalcogenides crystallize in a rock-salt structure and the fundamental bandgap is located at the L point of the Brillouin zone (BZ).[1-3, 8] Since there are four L-points, the highest valence level and the lowest conduction level are eight times degenerate (if the spin degeneracy is included). This leads to a 64-fold degeneracy of the lowest exciton state ($1S_h$-$1S_e$). The degeneracy is partially lifted due to a number of effects (*viz.,* intraband and intervalley couplings and electron-hole exchange).[1, 9] The exciton fine structure of PbSe and PbSe-based heteronanocrystals, *e.g*., PbSe/CdSe HNCs[10-12] is not completely investigated. Optical spectroscopy has been extensively used in order to investigate the electronic structure of HNCs composed of lead chalcogenides (*e.g.,* PbSe/CdSe, PbS/CdS or PbSe/PbS core/shell QDs).[11, 13, 14] Optical spectroscopy gives information about allowed transitions only, and therefore, not all of the energy levels can be determined. Moreover, due to inhomogeneity of the sample, the optical results acquired on a nanocrystal suspension are usually broadened. In contrast, scanning tunneling microscopy (STM) and spectroscopy (STS) can provide the topography and complete electronic structure of a single nanocrystal under investigation, [15-17] where the STS conductance spectrum (dI/dV_b) is proportional to the local density of states of the measured nanocrystal. Scanning tunneling spectroscopy of a single NC is based on the tunneling of electrons through a double-barrier tunnel junction (DBTJ), consisting of the tip/NC and NC/substrate junction. The number of additional electrons (holes) in the NC is a crucial parameter indicating one of the two possible tunneling regimes, called shell-tunneling and shell-filling regimes.[16, 17]

The shell-tunneling regime occurs if the rate of electron tunneling into the NC, Γ_{in} is much smaller than the rate of tunneling out of the NC, Γ_{out} (see Fig. 5.1). This condition can be reached for example, by increasing the tip-dot distance. In this regime the electron (hole) tunnels through the NC one by one, *i.e*., inter-particle interactions do not occur. Therefore the measured spectrum directly reflects the density of single-particle states of the NC. The potential distribution over the DBTJ in this regime is usually asymmetric and the largest fraction of the potential drops between tip and QD ($\eta \sim 1$). The first resonance (peak) is observed when the bias is sufficient to align the Fermi level of the tip with the first electron level of the nanocrystal: [18]

$$\eta V_b = E_{e1} + \Sigma_{e1} \tag{5.1}$$

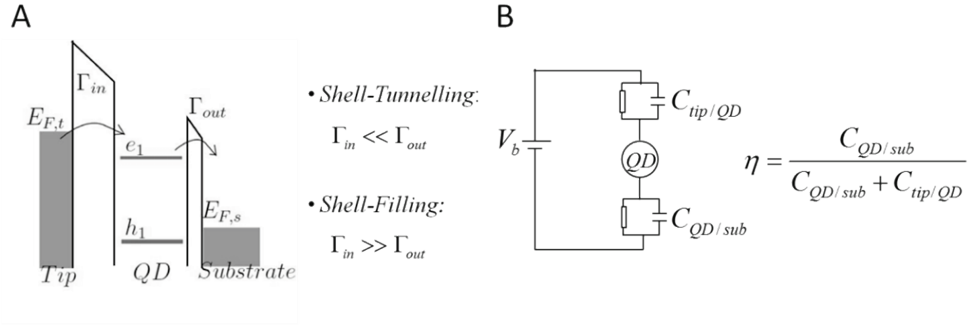

Fig. 5.1 (A) The energy configuration of the two tunnelling junctions, where e_1 is the lowest conduction level of the QD and h_1 is the highest valence level. Reprinted from.[19] (B) Scheme of electric circuit of the DBTJ.

where E_{e1} is the energy of the lowest unoccupied electron level and Σ_{e1} is the polarization energy (the energy needed to add one electron to the level $e1$). Similarly, the first hole is added when

$$\eta V_b = E_{h1} - \Sigma_{h1} \tag{5.2}$$

In the shell-filling regime, *i.e.,* when Γ_{in} is (much) higher then Γ_{out}, the electrons (holes) accumulate in the NC and the Coulomb interactions between charges are observed. This causes the degeneracy of the levels to be lifted, and the tunneling spectrum shows additional resonances (peaks). In practice, the shell-filling regime can be obtained by *e.g.,* decreasing the tip-dot distance or by increasing the dot-substrate distance. In the shell-filling regime a second electron can be added to the same energy level. This occurs at a bias V_b given by:

$$\eta V_b = E_{e1} + \Sigma_{e1} + J_{e-e} \tag{5.3}$$

where J_{e-e} is the electron-electron repulsion between the added electrons.

The potential distribution over the DBTJ characterized by η (sometimes called lever-arm) is an important parameter which defines the ratio of the potential drop between the tip and the nanocrystal divided by the overall applied bias. The DBTJ can be described by the electric circuit presented in Fig. 5.1B. The lever-arm is then defined as the ratio between the QD/substrate capacitance ($C_{QD/sub}$) and the sum of the QD/substrate ($C_{QD/sub}$) and tip/QD ($C_{tip/QD}$) capacitances, *i.e.*, $\eta = C_{QD/sub}/(C_{QD/sub} + C_{tip/QD})$. Knowing η is crucial in order to

understand the STS spectra. In most cases the potential distribution is asymmetric, *i.e.*, the tip-QD barrier width is larger than the QD-substrate barrier width, so the ($C_{tip/QD}$) is much smaller than ($C_{QD/sub}$) and the lever-arm is close to 1. However, a symmetric potential distribution is possible when the thickness of both tunneling barriers are similar *i.e.,* ($C_{QD/sub} \approx C_{tip/QD}$) and $\eta \sim 0.5$. In that case, tunneling of electrons and holes can occur on both sides of zero-conductivity gap. This is known as bipolar transport.[20, 21]

Understanding the electronic structure of nanocrystals and heteronanocrystals is crucial for possible photonic applications. It is known that a transformation of HNC into another structure (*e.g.*, PbSe/CdSe core/shell QDs into PbSe/CdSe bi-hemisphere HNCs)[12] can change the electronic fine structure. Scanning tunneling spectroscopy is a suitable technique in order to measure the electronic structure of simple QDs and more complex heteronanocrystals, like PbSe/CdSe bi-hemisphere HNCs.[22, 23] Here, we present a STM and STS study of PbSe/CdSe bi-hemispheres formed by *in-situ* STM annealing of PbSe/CdSe core/shell QDs in vacuum, where the transformation into PbSe/CdSe bi-hemispheres occurs.[12] Since the PbSe/CdSe bi-hemisphere nanocrystals are non-centro symmetric, the nanocrystals can have different orientations in the DBTJ. This leads to a plethora of tunneling spectra and additional difficulties in the interpretation. Here, we attempt to interpret some recurrent spectra that possibly reflect a well-defined orientation of the PbSe/CdSe bi-hemisphere in the DBTJ.

5.2 Experimental Section

The colloidal PbSe/CdSe core/shell QDs with 7.6 nm total diameter and 5.6 nm PbSe core were synthesized by the ion-exchange method.[14] Next, the QDs were drop casted on highly oriented pyrolytic graphite (HOPG) and heated in the STM preparation chamber in vacuum to approximately 100°C overnight. Upon heating in vacuum, the PbSe/CdSe core/shell QDs transform into bi-hemispheres as presented in Fig. 5.2. The transformation of PbSe/CdSe core/shell QDs into PbSe/CdSe bi-hemispheres is discussed in detail in Chapter 4. STM experiments (LT-STM, Omicron GmbH) were carried out at 4.8 K in ultra high vacuum UHV ($5 \cdot 10^{-11}$ mbar) with cut PtIr tips. STM topography images were typically obtained at bias of 2.5 V and a set-point current of 10 pA. The differential conductance spectra (dI/dV_b *vs* V_b) were obtained by positioning the tip above a single HNC and performing the measurement with the feedback loop disconnected. A lock-in amplifier was used to detect the differential conductance signal. STM topographic images and tunneling spectra were investigated by LT-STM at Utrecht University (with Dr. Z. Sun and Dr. I. Swart), additional measurements have been performed at the University of Lille (Dr. B. Grandidier and Corentin Durand).

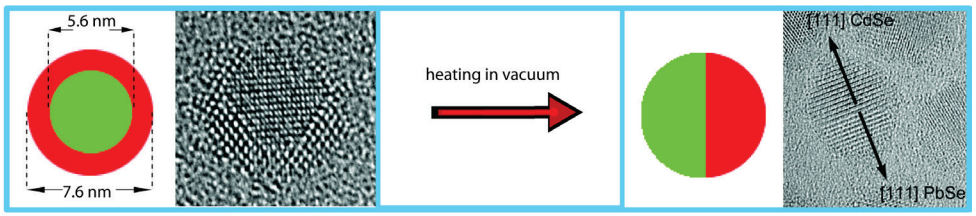

Fig. 5.2 Schematic representation of transformation of PbSe/CdSe core/shell QD into PbSe/CdSe bi-hemispheres upon heating in vacuum. (For details, see Chapter 4)

5.3 Results and Discussion

Figure 5.3 (A,C) shows STM topography images of PbSe/CdSe HNCs deposited on a HOPG substrate. One can see that the heteronanocrystals ordered in a hexagonal monolayer on the substrate. The HNC monolayer was stable under STM imaging. The apparent height of the HNCs is found to be 7.5 nm, as extracted from the height profile shown in Fig. 5.3 B This is in very good agreement with the size obtained from TEM images and from optical measurements (~7.6 nm). A histogram (63 particles involved in the analysis) is given in Fig. 5.3 D. The width of the nanocrystals from STM images is usually larger than the NC height, especially for isolated NCs. This can arise because the tip has an effective radius of curvature that broadens the lateral size of the nanocrystals due to convolution effects. For nanocrystals in the arrays, however, the lateral broadening is usually small because a tip cannot reach the surface anymore. Therefore, in our case the width of the HNC (Fig. 5.3B) does not differ significantly from the HNCs height.

After the STM imaging the tip was stabilized above an individual PbSe/CdSe HNC to perform spectroscopy. Series of tunneling spectra for different tunneling conditions (set-point current and bias voltage) were taken for many different HNCs (in total approximately 80 particles were studied). In general, the quantitative features of the spectra vary widely from dot to dot. In this chapter, we will present and interpret tunneling spectra that were recurrently observed (for different dots) and could, at least qualitatively, be understood.

After heating, the PbSe/CdSe core/shell QDs transformed into the PbSe/CdSe bi-hemispheres (see Chapter 4). The broken symmetry leads to a large variety of possible configurations of the HNC in the double barrier tunneling junction, the three configurations which will be the easiest to understand are depicted in Fig. 5.4. It is important to note that the orientation of the PbSe/CdSe bi-hemispheres on the substrate cannot be determined from the topographic images. It is hence required to assume a given configuration when

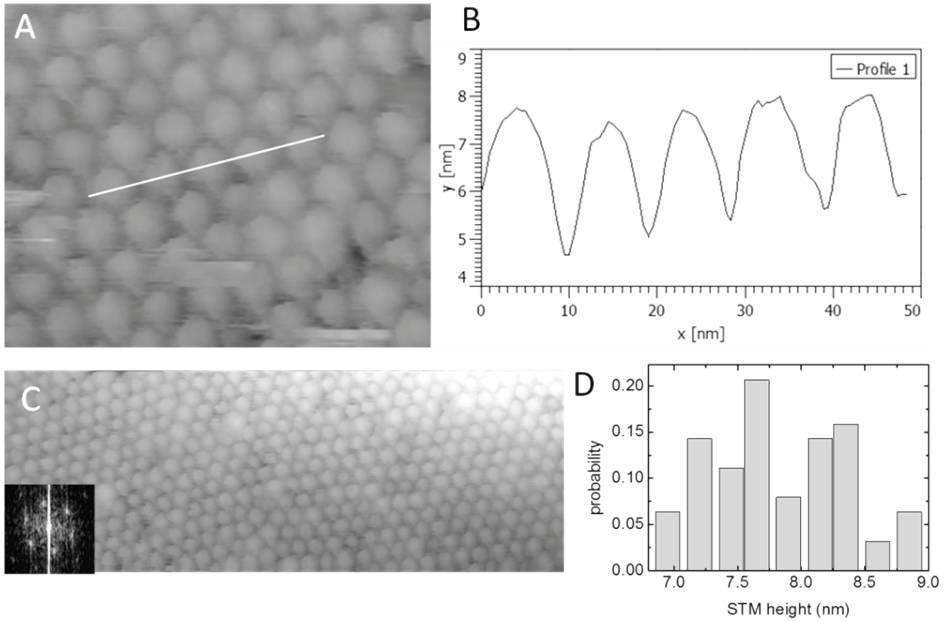

Fig. 5.3 (A) Constant-current STM image of PbSe/CdSe HNCs on HOPG substrate. The image was acquired at a bias voltage V_b =2.5 V and set-point current of I = 10 pA. (B) The apparent height profile of the white line shown in (A). (C) Constant-current STM image of PbSe/CdSe HNCs on HOPG substrate. Imaging parameters: bias voltage V_b = 2.5 V and set-point current of I = 10 pA. Inset: Fourier transform of the STM image. (D) Histogram of height of PbSe/CdSe HNCs.

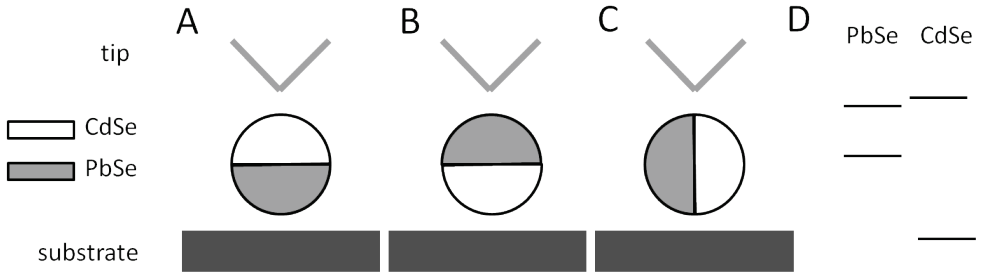

Fig. 5.4 (A-C) Different configurations of PbSe/CdSe bi-hemispheres in the double barrier tunnel junction between STM tip and the substrate. (D) Scheme of PbSe/CdSe band alignment.

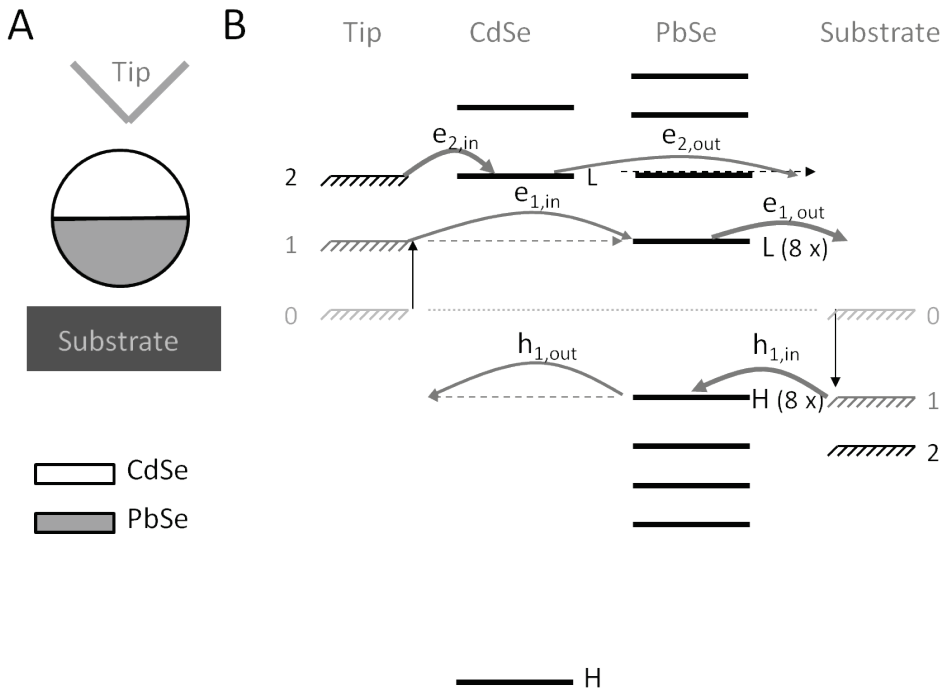

Fig. 5.5 (A) Possible configurations of PbSe/CdSe bi-hemispheres in the DBTJ between STM tip and the substrate, where the CdSe part is on the tip side and PbSe is on the substrate side. (B) Scheme of energy levels for PbSe/CdSe bi-hemispheres in DBTJ.

tunneling spectra are analyzed. "Intermediate" orientations lead to variable and complex spectra. Furthermore, we will assume that there is no significant hybridization of the CdSe and PbSe states. We will now briefly discuss what kind of STS spectra one would expect for the three simplest configurations.

An anticipated tunneling scheme for the first configuration shown in cartoon (Fig.5.4A) is presented in Fig. 5.5B. The energy-level scheme that we assume here is tentative and based on results obtained for core/shell quantum dots (Fig. 5.4D). Depending on the bias voltage and lever-arm η we can distinguish several situations. First, the situation marked by "0" (Fig. 5.5B) corresponds to no bias applied. Next, when a (low) positive bias is applied

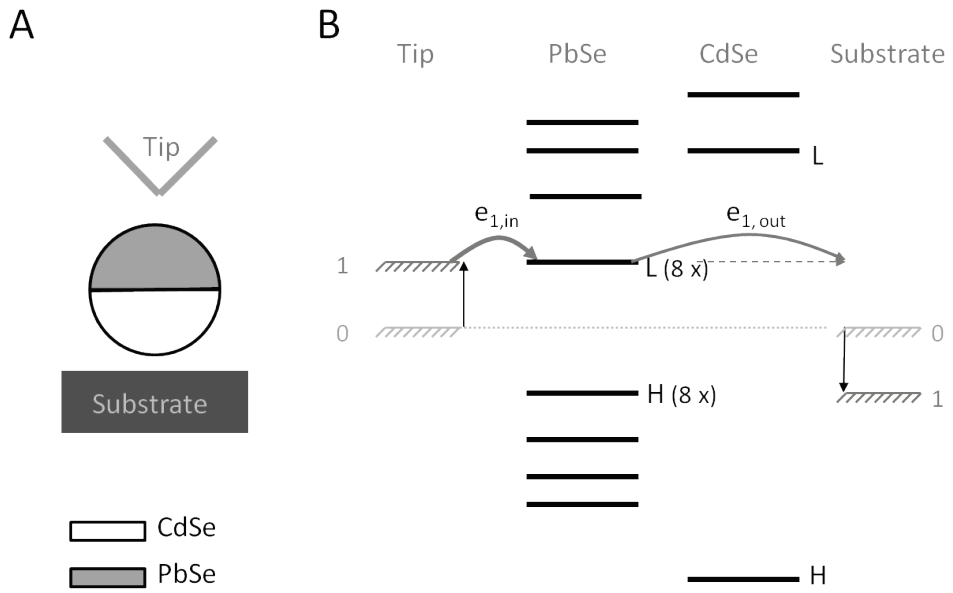

Fig. 5.6 (A) Possible configurations of PbSe/CdSe bi-hemispheres in the DBTJ between STM tip and the substrate, where PbSe part is on the tip side and CdSe is on the substrate side. (B) Scheme of energy levels for PbSe/CdSe bi-hemispheres in DBTJ.

that is sufficient to align the tip Fermi level with the first electron level of PbSe (situation "1"), electron transport through the CdSe part to the lowest LUMO (first) energy level of PbSe (8 fold degenerated LUMO) is possible. Considering the thickness of CdSe (~3.5 nm), there is still a detectable probability of electron transfer from the tip (through CdSe) into the PbSe part of HNC. In this configuration, the electron tunneling rate out of the PbSe ($e_{1,out}$) will be much higher than the electron tunneling rate into the PbSe part ($e_{1,in}$) (shell-tunneling regime). When the potential distribution is more symmetric ($\eta \sim 0.5$) the hole transport from the substrate to the highest (first) hole energy level (8-fold degenerate HOMO level) of PbSe is possible at low positive bias. From the PbSe, the hole has to tunnel directly into the tip. Hence, hole-transport will occur in the shell-filling regime. When a larger positive bias voltage is applied (situation "2", Fig. 5.5), which is sufficient to align the Fermi level of the tip with the first electron level of CdSe (LUMO), electron transport via this state is possible. Considering the band alignment, the electron can migrate to the PbSe part of the HNC before tunneling to the substrate. Depending on the set-point conditions, this could lead to transport in the shell-filling regime.

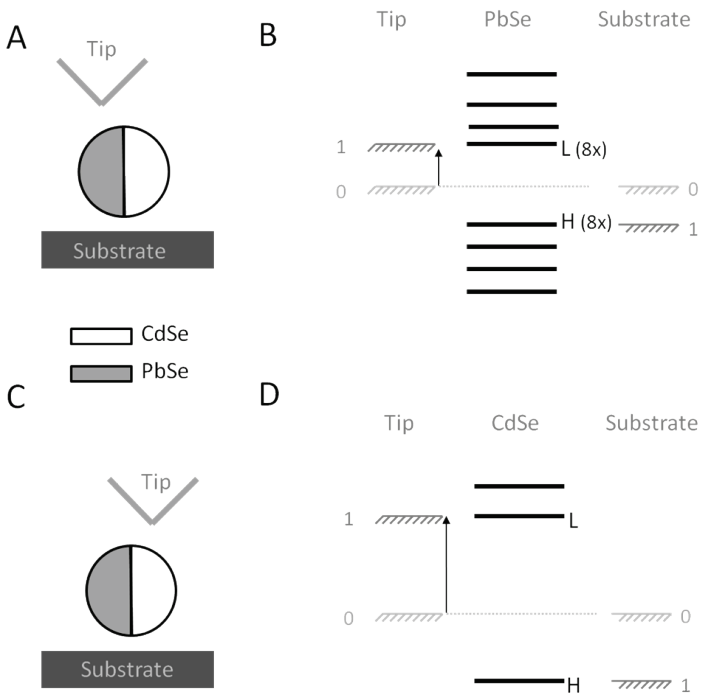

Fig. 5.7 Possible configurations of PbSe/CdSe bi-hemispheres in the DBTJ where (A) PbSe lies between STM tip and the substrate and (C) CdSe lies between STM tip and the substrate. (B) Scheme of energy levels for PbSe/CdSe bi-hemispheres in DBTJ presented in sketch (A). (D) Scheme of energy levels for PbSe/CdSe bi-hemispheres in DBTJ presented in sketch (C).

The second possible configuration of the bi-hemisphere PbSe/CdSe HNC in the DBTJ is presented in the Fig. 5.6. Here, the PbSe part is closer to the tip and CdSe lies on the substrate side. When a low bias voltage is applied (situation "1") electron transport from the tip to the LUMO levels of PbSe can occur, followed by direct tunneling into the substrate. Hence, shell-filling is expected. Hole transport from the substrate to the first hole level (HOMO) of the CdSe part is not possible due to the energy level configuration. Tunneling of holes from the substrate directly into the PbSe HOMO through the CdSe is unlikely. If this would occur, shell-tunneling is expected. Applying a larger positive bias voltage would cause electron tunneling from the tip into higher lying PbSe electron levels.

Another possible configuration of the bi-hemispheres PbSe/CdSe HNC in the DBTJ is shown in the Fig. 5.7. Here, the charge transport is less complicated, since only one semiconductor material is involved in the tunneling process. Depending on the tip position (which can be situated above PbSe or CdSe part) typical spectra for PbSe or CdSe are expected. In principle, charge transport can occur in both shell-tunneling and shell-filling regimes.

Types of spectra which are most frequently observed are shown in Figures 5.8, 5.9 and 5.10. We found that the experimental spectra show mostly two types of peaks: sharp ones (Fig. 5.9) and the broad ones with additional replicas (Fig. 5.8 and 5.10). In general, when an electron is transferred to a NC, its charge interacts with the lattice and thus leads to local lattice distortion. As the dimensions of the crystal decreases, the coupling between incoming electrons and polar (longitudinal optical) LO-phonons can become significant. Especially in CdSe nanocrystals, the coupling between electrons and photons is well documented.[24]

Figure 5.8 shows one type of spectrum, where at higher bias voltage (above 1.1 V) the series of equally spaced pairs of peaks (*i.e.*, *e-f* and *i-k* pairs) each with replicas (named *g, h, j, l, m, o*) are observed. These replicas can be unambiguously related to the electron-phonon interaction in CdSe nanocrystals.[24, 25] From theoretical calculations, the longitudinal optical (LO) phonon mode in CdSe has an energy of 26 meV. [25] Our spectra show the separation between peaks. By dividing the theoretical phonon energy by the experimental separation between replicas, the lever arm η can be determined, which in turn allows us to estimate the position of the CdSe and PbSe parts in the DBTJ. We find η = 0.66 ± 0.03, which is considerably below one and smaller than expected for pure PbSe NCs. Hence we conclude that the CdSe part must be closest to the tip as presented in the sketch in Fig. 5.5.

The equally spaced pairs of peaks (*e-f* and *i-k*) can be assigned to electron-electron repulsion J_{e-e} in CdSe. This would indicate the shell-filling regime (as shown in situation "2", Fig. 5.5B). It follows that we can assign peak *e* and *f* as electron S states and *i* and *k* as electron P states of CdSe. The distance between *e-f* and *i-k* is equal to 119 mV. Converting it to the energy scale (using η=0.66) we get J_{e-e}= 79 meV. The electron-electron repulsion in a spherical nanocrystal can be calculated from:[18, 26]

$$J = \frac{e^2}{4\pi\varepsilon_0 R}\left(\frac{1}{\varepsilon_{out}} + \frac{0.79}{\varepsilon_{in}}\right) \tag{5.4}$$

where R is the NC radius and $\varepsilon_0, \varepsilon_{in}, \varepsilon_{out}$ are dielectric constant of vacuum, nanocrystal material and surrounding medium, respectively. Knowing that the volume of the CdSe hemisphere of the HNC equals the volume of a CdSe QD with diameter of 6.4 nm, we can

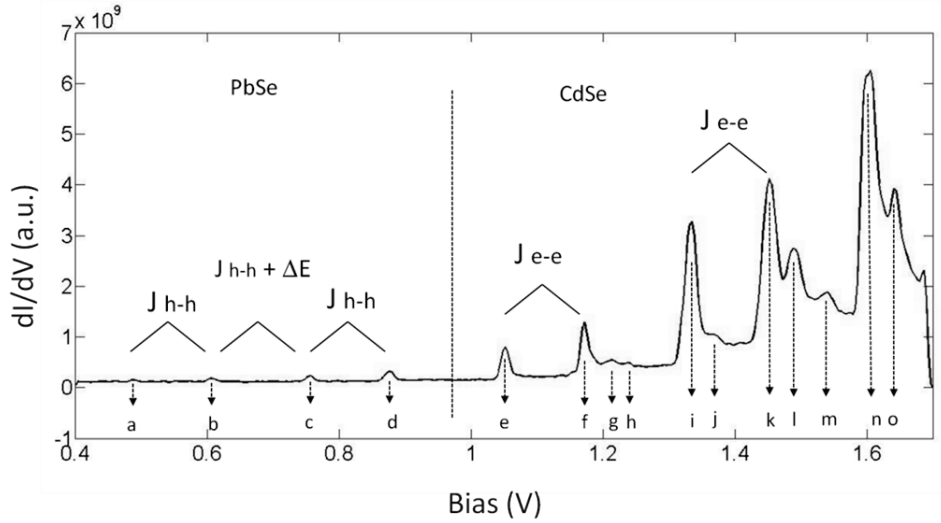

Fig. 5.8 Spectroscopy of PbSe/CdSe bi-hemisphere HNC with clear indication of electron-phonon coupling in the CdSe part, (replicas *g, h, j, l, m, o*). STS settings are: 800 pA of set-point current and 1.7 V of bias voltage.

calculate J_{e-e}. [From optical measurements the 6.4 nm CdSe QDs should have a band gap of 1.95 eV.[27]] This gives an electron repulsion energy of J_{e-e} =95 meV. This value is reasonably close to our experimental value of 79 meV. This supports the idea that the double peaks *e-f* and *i-k* result from electron-electron repulsion (shell-filling regime).

A series of small, equally spaced pairs of peaks are visible in the range of lower bias voltage (Fig. 5.8 peaks *a-b*, *c-d*, below 1V). These resonances possibly reflect tunneling into the PbSe part of HNC. Since the potential distribution in the DBTJ is rather symmetric, hole transport is possible at low positive bias. The pair of peaks can be attributed the hole-hole repulsion indicating the shell-filling regime for hole transport in PbSe (see, Fig. 5.5B). The spacing between *a-b* and *c-d* is 117 mV. Converting it to energy scale by multiply by values of η =0.66 we found lower limit of J_{h-h} = 77 meV. In practice the J_{h-h} value can be bigger since lever arm may be larger than that of η =0.66. The estimated values, however, is in agreement with the calculated from eq. (5.1) values of J_{h-h} =89 meV for 5.6 nm PbSe QDs. The pair of peaks *a-b* and *c-d* can hence be assigned to hole-hole interaction in the S electron state.

As was discussed in Chapter 3, the fundamental band gap of the rock salt PbSe comes from 4 equivalent L points in the BZ. As the dimensions of the NC decrease, and quantum

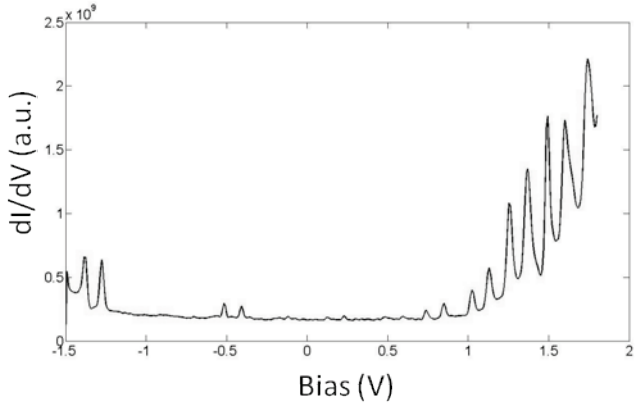

Fig. 5.9 Spectroscopy of PbSe/CdSe bi-hemisphere HNC. STS parameters: bias voltage V_b = 1.8 V and set-point current of I = 500 pA.

confinement become stronger, the inter-valley splitting becomes significant, especially for NCs smaller than 5 nm (see Chapter 3). In our case the PbSe/CdSe HNC has a PbSe volume equal to that of a 5.6 nm diameter PbSe QD. For this relatively large NCs the intervalley splitting is small, however still noticeable. Our spectra (Fig. 5.8) show that the intervalley splitting, marked in the picture as ΔE is 21 meV. This experimental value is in good agreement with the estimated value of 23 meV presented in Chapter 3 in Fig. 3.10C for NCs with 5.6 nm diameter.

Another type of frequently observed STS spectrum for PbSe/CdSe bi-hemisphere QDs is presented in Fig. 5.9. It can be seen that the spectrum in Fig. 5.9 is characterized by series of sharp peaks at positive and negative bias voltage. Most probably these peaks reflect PbSe energy levels, since no characteristic CdSe features (*i.e.,* phonon replicas) are observed. This spectrum can be related to the sketch in the Figure 5.6, where the PbSe part is located at the tip side. Here, the spectrum should be dominated by features related to PbSe levels under shell-filling conditions. A series of double peaks, which is characteristic for shell-filling conditions, are visible at positive and negative bias side with the constant separation of 109 mV. Since we observe possibly bipolar transport, the STS band gap cannot be easily extracted from such spectra. To give a rough idea, the band gap obtained from optical measurements for 5.6 nm PbSe QDs is 0.76 meV.

A third type of STS spectrum is presented in Figure 5.10. It differs considerably from the previous one (Fig.5.9). These kinds of spectra were also frequently observed for many different QDs. Here, in contrast to sharp peaks one can see broad peaks with additional

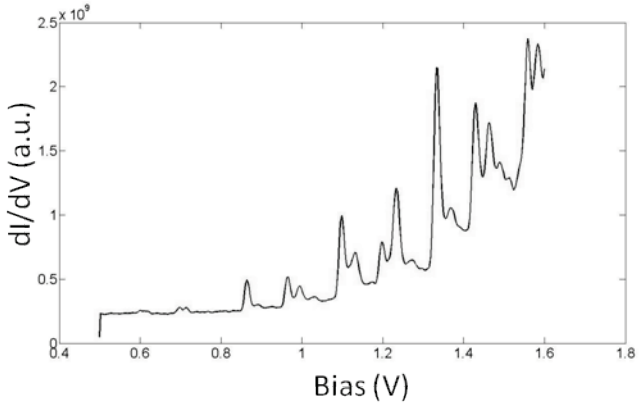

Fig. 5.10 Spectroscopy of PbSe/CdSe bi-hemisphere HNC. STS parameters: bias voltage V_b = 1.6 V and set-point current of I = 400 pA.

replicas characteristic for CdSe. It is clear that these peaks reflect CdSe states showing electron-phonon coupling (also observed in Fig. 5.8). We tentatively assign these spectra to bi-hemispheres oriented as presented in Fig. 5.7C, where only the CdSe part is located between tip and the substrate. However, besides characteristic peaks for CdSe, small peaks (around 0.6 and 0.7 mV), which can be attributed to PbSe, are observed. It could be that the interface between the PbSe and CdSe parts of the bi-hemisphere is not perfectly perpendicular to the surface. Another possibility is that there is quantum mechanical coupling between electronic states of the PbSe and CdSe. Consequently, it is difficult to achieve a full understanding of the features in these type of spectra.

5.4 Conclusions

In summary, we have presented an STM and STS study of PbSe/CdSe bi-hemispheres. These structures can be created by heating core/shell QDs in the vacuum chamber of the STM, as was shown in a previous study. The measured spectra are complex, vary from dot to dot, and show mostly multiple features characteristic for PbSe and CdSe semiconductors. We made an attempt to understand the spectra using well-defined orientations of the PbSe/CdSe bi-hemispheres in DBTJ. Our interpretation was helped by the characteristic phonon replica in the CdSe NCs. We were able to obtain values for the intervalley splitting and Coulomb repulsion in the PbSe in fair agreement with leading models. A large number of non-trivial STS spectra showed that, possibly due to the random orientation of the bi-

hemisphere, it is not straightforward to derive the electronic structure of PbSe/CdSe bi-hemisphere nanocrystals from STS data.

References

1. Allan, G. and C. Delerue, *Confinement effects in PbSe quantum wells and nanocrystals.* Physical Review B, 2004. **70**(24): p. 245321.
2. An, J.M., A. Franceschetti, S.V. Dudiy, and A. Zunger, *The Peculiar Electronic Structure of PbSe Quantum Dots.* Nano Letters, 2006. **6**(12): p. 2728-2735.
3. An, J.M., A. Franceschetti, and A. Zunger, *The Excitonic Exchange Splitting and Radiative Lifetime in PbSe Quantum Dots.* Nano Letters, 2007. **7**(7): p. 2129-2135.
4. Du, H., C. Chen, R. Krishnan, T.D. Krauss, J.M. Harbold, F.W. Wise, M.G. Thomas, and J. Silcox, *Optical Properties of Colloidal PbSe Nanocrystals.* Nano Letters, 2002. **2**(11): p. 1321-1324.
5. Harbold, J.M. and F.W. Wise, *Photoluminescence spectroscopy of PbSe nanocrystals.* Physical Review B, 2007. **76**(12): p. 125304.
6. Brumer, M., A. Kigel, L. Amirav, A. Sashchiuk, O. Solomesch, N. Tessler, and E. Lifshitz, *PbSe/PbS and PbSe/PbSexS1–x Core/Shell Nanocrystals.* Advanced Functional Materials, 2005. **15**(7): p. 1111-1116.
7. Suzuki, N., K. Sawai, and S. Adachi, *Optical properties of PbSe.* Journal of Applied Physics, 1995. **77**(3): p. 1249-1255.
8. Martinez, G., M. Schlüter, and M.L. Cohen, *Electronic structure of PbSe and PbTe. Band structures, densities of states, and effective masses.* Physical Review B, 1975. **11**(2): p. 651.
9. Grodzińska, D., J. Van Rijssel, M. Van Huis, A. Meijerink, C. de Mello Donegá, and D. Vanmaekelbergh, *Two-fold emission from the S-shell of PbSe(core)/CdSe(shell) quantum dots.* Small, 2011.
10. Casavola, M., M.A. van Huis, S. Bals, K. Lambert, Z. Hens, and D. Vanmaekelbergh, *Anisotropic Cation Exchange in PbSe/CdSe Core/Shell Nanocrystals of Different Geometry.* Chemistry of Materials, 2012. **24**(2): p. 294-302.
11. De Geyter, B., Y. Justo, I. Moreels, K. Lambert, P.F. Smet, D. Van Thourhout, A.J. Houtepen, D. Grodzinska, C. de Mello Donega, A. Meijerink, D. Vanmaekelbergh, and Z. Hens, *The Different Nature of Band Edge Absorption and Emission in Colloidal PbSe/CdSe Core/Shell Quantum Dots.* ACS Nano, 2011. **5**(1): p. 58-66.
12. Grodzinska, D., F. Pietra, M.A. van Huis, D. Vanmaekelbergh, and C. de Mello Donega, *Thermally induced atomic reconstruction of PbSe/CdSe core/shell quantum dots into PbSe/CdSe bi-hemisphere hetero-nanocrystals.* Journal of Materials Chemistry, 2011. **21**(31): p. 11556-11565.
13. Sashchiuk, A., L. Langof, R. Chaim, and E. Lifshitz, *Synthesis and characterization of PbSe and PbSe/PbS core-shell colloidal nanocrystals.* Journal of Crystal Growth, 2002. **240**(3-4): p. 431-438.
14. Pietryga, J.M., D.J. Werder, D.J. Williams, J.L. Casson, R.D. Schaller, and V.I. Klimov, *Utilizing the Lability of Lead Selenide to Produce Heterostructured Nanocrystals with Bright, Stable Infrared Emission.* Journal of the American Chemical Society, 2008. **130**(14): p. 4879-4885.
15. Binnig, G. and H. Rohrer, *Scanning tunneling microscopy - from birth to adolescence.* Reviews of Modern Physics, 1987. **59**(3): p. 615-625.

16. Liljeroth, P., L. Jdira, K. Overgaag, B. Grandidier, S. Speller, and D. Vanmaekelbergh, *Can scanning tunnelling spectroscopy measure the density of states of semiconductor quantum dots?* Physical Chemistry Chemical Physics, 2006. **8**(33).
17. Liljeroth, P., P.A.Z. van Emmichoven, S.G. Hickey, H. Weller, B. Grandidier, G. Allan, and D. Vanmaekelbergh, *Density of States Measured by Scanning-Tunneling Spectroscopy Sheds New Light on the Optical Transitions in PbSe Nanocrystals.* Physical Review Letters, 2005. **95**(8): p. 086801.
18. Overgaag, K., *Ph.D thesis. Electronic coupling in self-assembled nanocrystal arrays. A scunning tunneling microscopy study*. 2008, Utrecht University: Utrecht. p. 118.
19. Sun, Z., *Atomic and Elactronic Structure of Quantum Dots Measured with Scanning Probe Techniques*. 2012, Ph.D Thesis,Utrecht University: Utrecht. p. 102.
20. Niquet, Y.M., C. Delerue, G. Allan, and M. Lannoo, *Interpretation and theory of tunneling experiments on single nanostructures.* Physical Review B, 2002. **65**(16): p. 165334.
21. Wu, S.W., G.V. Nazin, X. Chen, X.H. Qiu, and W. Ho, *Control of Relative Tunneling Rates in Single Molecule Bipolar Electron Transport.* Physical Review Letters, 2004. **93**(23): p. 236802.
22. Steiner, D., D. Dorfs, U. Banin, F. Della Sala, L. Manna, and O. Millo, *Determination of Band Offsets in Heterostructured Colloidal Nanorods Using Scanning Tunneling Spectroscopy.* Nano Letters, 2008. **8**(9): p. 2954-2958.
23. Swart, I., Z. Sun, D.l. Vanmaekelbergh, and P. Liljeroth, *Hole-Induced Electron Transport through Core-Shell Quantum Dots: A Direct Measurement of the Electron-Hole Interaction.* Nano Letters, 2010. **10**(5): p. 1931-1935.
24. Sun, Z., I. Swart, C. Delerue, D.l. Vanmaekelbergh, and P. Liljeroth, *Orbital and Charge-Resolved Polaron States in CdSe Dots and Rods Probed by Scanning Tunneling Spectroscopy.* Physical Review Letters, 2009. **102**(19): p. 196401.
25. Klein, M.C., F. Hache, D. Ricard, and C. Flytzanis, *Size dependence of electron-phonon coupling in semiconductor nanospheres: The case of CdSe.* Physical Review B, 1990. **42**(17): p. 11123-11132.
26. Delerue, C. and M. Lannoo, *Nanostructures. Theory and Modeling*. 2004: Springer. 304.
27. de Mello Donegá, C. and R. Koole, *Size Dependence of the Spontaneous Emission Rate and Absorption Cross Section of CdSe and CdTe Quantum Dots.* The Journal of Physical Chemistry C, 2009. **113**(16): p. 6511-6520.

Summary

This thesis describes a study of the structural and opto-electronic properties of colloidal PbSe/CdSe core/shell QDs. PbSe/CdSe heteronanocrystals are of considerable interest as novel optoelectronic materials operating in the near IR. The atomic structure of the PbSe/CdSe heteronanocrystals determines the energy level spectrum and optical properties, and is thus crucial. On the other hand, the presence of organically capped surfaces and a PbSe/CdSe interface in each nanocolloid raises questions on the (thermal) stability of such systems.

In the first chapter, a general introduction to semiconductor nanocrystal quantum dots QDs is given, followed by an explanation of their electronic structure and of so-called quantum confinement effects. An introduction to semiconductor heteronanocrystals and scanning tunneling microscopy and spectroscopy is also presented in this chapter.

Chapter 2 present the synthesis of PbSe/CdSe core/shell quantum dots and their room temperature optical properties for different core diameters and shell thicknesses. High-resolution transmission electron microscopy studies are presented and indicate that the PbSe core has an octahedral like shape with eight Se{111} interfacial planes shared with the CdSe shell, and that the CdSe shell has a non-uniform thickness. An analysis of the absorption and luminescence spectra of PbSe/CdSe core/shell QDs shows that the absorption oscillator strength of the first exciton transition is similar to that of plain PbSe QDs of comparable sizes. In contrast, the oscillator strength of the emitting transition is reduced by at least 75%, compared to PbSe QDs. Moreover, the addition of an electron scavenger quenches the PbSe/CdSe QD emission, while a hole scavenger does not. This suggests that the electron wave function reaches the QD surface, while the hole is confined to the PbSe core, indicating the Type I ½ carrier localization regime.

Chapter 3 deals with the optical properties of PbSe/CdSe core/shell quantum dots with core sizes smaller than 4 nm in the 5–300 K range. The low temperature photoluminescence spectra show two peaks, which become increasingly separated in energy as the core diameter is reduced below 4 nm. It is shown that these peaks are due to intrinsic exciton transitions in each quantum dot. The energy separation between the peaks is most probably due to inter-valley coupling between the L-points of PbSe. The evolution of the two luminescence peaks with the temperature is non-trivial and implies an intricate communication between bright and dark states.

In Chapter 4 we have investigated the atomic reconstruction of colloidal PbSe/CdSe core/shell quantum dots upon annealing under vacuum. We show that thermal annealing

under vacuum at temperatures between 150 °C and 200 °C induces a structural and morphological reconstruction of the HNCs whereby the PbSe core and the CdSe shell are reorganized into two hemispheres joined by a common Se{111} plane. This thermally induced reconstruction leads to considerable changes in the optical properties of the colloidal PbSe/CdSe HNCs.

Chapter 5 presents a scanning tunneling microscopy and spectroscopy study of PbSe/CdSe bi-hemisphere heteronanocrystals HNCs, created upon in-situ heating in the STM vacuum chamber. This chapter deals with the question: what kind of spectra can we observe for different orientations of the PbSe/CdSe bi-hemispheres in the double barrier tunneling junction (DBTJ)? We show that measured spectra are complex, vary from dot to dot, and exhibit mostly multiple features characteristic for PbSe and CdSe semiconductor quantum dots.. We made an attempt to understand the spectra using well-defined orientations of the PbSe/CdSe bi-hemispheres in the DBTJ. Our interpretation was helped by the characteristic phonon replica in the CdSe NCs. We were able to obtain values for the intervalley splitting and Coulomb repulsion in the PbSe in fair agreement with leading models. A large number of non-trivial STS spectra showed that, possibly due to the random orientation of the bi-hemisphere, it is not straightforward to derive the electronic structure of PbSe/CdSe bi-hemisphere nanocrystals from STS data.

Samenvatting

Dit proefschrift beschrijft een studie van de structurele en opto-elektronische eigenschappen van colloïdale nanokristallen bestaande uit een PbSe kern omringd door een CdSe schil. Deze PbSe/CdSe heteronanokristallen staan in de belangstelling als nieuwe opto-elektronische materialen met overgangen in het nabije infrarood. De atomaire structuur van PbSe/CdSe heteronanokristallen bepaalt de ligging van de energieniveaus, en daarmee de optische eigenschappen. Kennis van en controle over de atomaire structuur is daarom van groot belang. Het oppervlak van de nanokristallen is beschermd door organische moleculen, en binnenin hebben ze een PbSe/CdSe kern/schil oppervlak. De (thermische) stabiliteit van deze oppervlakken wordt in dit proefschrift onderzocht.

Het eerste hoofdstuk bevat een algemene inleiding over halfgeleider nanokristallen (ook wel quantum dots [QDs] genoemd), gevolgd door een beschrijving van hun elektronische structuur en van het zogenaamde "quantum confinement effect". Daarna volgt een inleiding over heteronanokristallen, d.w.z. nanokristallen bestaande uit twee materialen. Aan het einde van het eerste hoofdstuk worden de principes van scanning tunneling microscopy (STM) en scanning tunneling spectroscopy (STS) uitgelegd.

In hoofdstuk twee wordt de synthese van PbSe/CdSe kern/schil QDs besproken. De optische eigenschappen bij kamertemperatuur worden gepresenteerd, voor verschillende kerndiameters en schildiktes. Hoge-resolutie transmission electron microscopy (TEM) plaatjes laten duidelijk zien dat de PbSe kern een octaëdrische vorm heeft en dat de CdSe schil de kern niet uniform bedekt. Bovendien tonen de TEM-plaatjes dat de kern en de schil, die immers verschillende kristalstructuren hebben, in elkaar overgaan via een gezamenlijk Se{111} kristalvlak. Een analyse van de absorptie en fotoluminescentie van de PbSe/CdSe kern/schil QDs toont aan dat de oscillatorsterkte van de eerste absorptiepiek vergelijkbaar is met die van zuivere PbSe QDs van gelijke grootte. De oscillatorsterkte van de emitterende overgang, daarentegen, is ongeveer 75% zwakker dan voor zuivere PbSe QDs. De emissie van PbSe/CdSe QDs kan worden gedoofd door naburige moleculen die elektronen wegvangen. Naburige moleculen die gaten zouden kunnen wegvangen, doven de emissie echter niet. Dit suggereert dat in PbSe/CdSe kern/schil QDs type I½ lokalisatie van ladingsdragers plaatsvindt: de elektronen verspreiden zich over de gehele QD, terwijl de gaten zich alleen in de PbSe kern bevinden.

Hoofdstuk 3 behandelt de optische eigenschappen van PbSe/CdSe kern/schil QDs met kernen kleiner dan 4 nm diameter bij variërende temperatuur tussen 5 K en 300 K. Bij lage temperaturen vertonen de fotoluminescentiespectra twee emissiepieken, met een scheiding in energie die toeneemt als de PbSe kern kleiner wordt. Deze twee pieken zijn afkomstig van intrinsieke excitonovergangen die plaatsvinden in elk van de QDs. De splitsing in energie is waarschijnlijk een gevolg van koppeling tussen de ontaarde laagst-energetische excitontoestanden op de L-punten in de Brillouinzone van PbSe. De temperatuurafhankelijkheid van de relatieve intensiteiten van de twee emissiepieken wijst op een complexe interactie tussen heldere (stralende) en donkere (niet-stralende) excitontoestanden.

Hoofdstuk 4 bevat een studie van de atomaire reorganisatie van colloïdale PbSe/CdSe kern/schil QDs wanneer deze worden verwarmd in vacuum. Bij temperaturen tussen 150°C en 200°C transformeren de PbSe/CdSe kern/schil QDs in een nieuwe bolvormige structuur bestaande uit een halve bol van zuiver CdSe en een halve bol van zuiver PbSe. De twee halve bollen zitten aan elkaar vast via een gemeenschappelijk Se{111} kristalvlak. De transformatie van PbSe/CdSe kern/schil naar PbSe/CdSe halve-bol/halve-bol QDs leidt tot opmerkelijke veranderingen in de optische eigenschappen.

In hoofdstuk 5 worden de PbSe/CdSe halve-bol/halve-bol QDs, gevormd in-situ door de verhitting van kern/schil QDs in de vacuümkamer van de STM, bestudeerd met STM en STS. Deze halve-bol/halve-bol QDs hebben een anisotrope vorm. Het energieniveauspectrum gemeten in STS is dus afhankelijk van de oriëntatie van de specifieke QD onder de STM naald. De spectra van twee verschillende QDs kunnen dan ook zeer verschillend zijn, wat de interpretatie niet eenvoudig maakt. Veelal zijn zowel karakteristieken te zien van PbSe als van CdSe. De interpretatie van de spectra wordt gedaan aan de hand van een aantal goed-gedefinieerde oriëntaties van de QDs onder de naald. Hierbij zijn de karakteristieke fotonreplica's in het energieniveauspectrum van CdSe QDs van groot belang. De interpretatie levert waarden voor de Coulombrepulsie en voor de energiesplitsing tussen de laagst-energetische excitontoestanden in het PbSe deel die in goede overeenstemming zijn met literatuurwaarden.

List of publications

This thesis is based on following publications:

- De Geyter, B., Y. Justo, I. Moreels, K. Lambert, P.F. Smet, D. Van Thourhout, A.J. Houtepen, D. Grodzińska, C. de Mello Donega, A. Meijerink, D. Vanmaekelbergh, and Z. Hens, *The Different Nature of Band Edge Absorption and Emission in Colloidal PbSe/CdSe Core/Shell Quantum Dots.* ACS Nano, 2011. 5(1): p. 58-66. *Chapter 2*

- Grodzińska, D., W.H. Evers, R. Dorland, J. van Rijssel, M.A. van Huis, A. Meijerink, C. de Mello Donegá, and D. Vanmaekelbergh, *Two-Fold Emission From the S-Shell of PbSe/CdSe Core/Shell Quantum Dots.* Small, 2011. 7(24): p. 3493-3501. *Chapter 3*

- Grodzińska, D., F. Pietra, M.A. van Huis, D. Vanmaekelbergh, and C. de Mello Donega, *Thermally induced atomic reconstruction of PbSe/CdSe core/shell quantum dots into PbSe/CdSe bi-hemisphere hetero-nanocrystals.* Journal of Materials Chemistry, 2011. 21(31): p. 11556-11565. *Chapter 4*

- Swart, I., D. Grodzińska, Z. Sun., C. Durand, T. H. Nguyen, B. Grandidier, C. Delerue, and D. Vanmaekelbergh, *Electronic Structure of PbSe/CdSe Bi-hemisphere Heteronanocrystals Measured by STM.* in preparation. *Chapter 5*

Beyond the scope of this thesis:

- Kuchowicz, M., R. Szukiewicz and D. Grodzińska, *Dependence of STM Images on Bias Polarity for Sm Layers on Mo(110) and Mo (211) Surfaces.* Acta Physica Polonica A, 2008, 114, S.59-69.

Acknowledgments

I would like to thank everybody who (in scientific and non-scientific way) contributed to creating this thesis.

First of all, I would like to thank my supervisors Daniël Vanmaekelbergh and Celso de Mello Donegá for giving me opportunity to join CMI group and work on HERODOT project, even if my background was in different field. I know you will never forget my "power-point" presentation at the interview ☺. The beginning was hard for me, nevertheless, you made everything to make my start smoother. Celso thank you for introduction to nano-colloidal-world, for the interesting lectures (and synthesis lessons) you gave to your student in which I could participate. I learn a lot from it. I need to thank you for all these hours you spend on helping me with my presentations (especially the first one). Thank you for your instructive suggestions and good words of motivation. Daniel, I really appreciate your help in solving my housing and registration problems at the beginning of my stay. I need to also thank you for being so patient while reading my Polish/English pre-chapter and putting all the articles in the correct places. I would like to thank both of you for your care, number of valuable and extensive discussions and your help in interpreting and understanding of the experimental results. Dziękuję ☺.

I am extremely grateful to the reading committee *i.e.,* Sara Bals, Andries Meijerink, John Kelly, Zeger Hens and Albert Philipse for their comments and quick reading of my thesis.

I would like to thank to all my CMI colleagues with who I have been working during the past 4 years. Especially, many thanks to Wiel. This thesis could never have been accomplished without you. Thank you for helping me with everything and being my teacher at the beginning. You teach me how to make a "coffee" in the lab and showed me that the King`s water is not so dangerous, as I thought. Francesca (Franczusia) my dear, I had a great pleasure to supervise you, my excellent Master student and PhD friend. You gave an important contribution to this thesis and doing experiments with you was a pure pleasure. Thank you for supporting me at work and in many aspect in personal life. I will never forget our girlish conversations with the wine (sorry for the trousers ☺). You gave me a lot of positive energy. I love you Fra. Many thanks go out to my best office-mate, Yiming. I will never forget the time we spend on scientific and less-scientific discussions. Thank you for your constructive suggestions and friendly conversations. I appreciate your magic hacker skills in finding every possible book in the internet. Besides being a good friend, you are the best uncle for Tofik. Thank you for taking care of him, whenever I needed to travel. Dziękuję Yimino. Rosa my dear Mariposa, gracias por su ayuda en los experimentos ópticos con el láser. Siempre me acuerdo de nuestras conversaciónes de viejas locas y los bailes en la pista de baile. Gracias por su ayuda con la tarea de español.

Mi niña perdida. Gracias. Marianna (Marianuszka) thank you for your support and kindness. I will miss our culinary meetings. You showed me how to make a real Italian pizza. I will miss you a lot Mari. Darku, dziękuję Ci za wsparcie i za to, że zawsze chętnie służyłeś mi pomocą w każdej sytuacji. Nigdy nie zapomnę naszej cudownej wycieczki do Barcelony. Będzie mi Ciebie brakowało Dareczku. Zahar, my super hero! thank you for saving my life and sorry for destroying your bike. You enlarged my top-favorite-food-list by showing me humus. Zhixiang thank you for your great support with STM. I highly appreciate your contribution to Chapter 5. I will never forget our refilling of STM at the weekends and the unexpected fire alarm that we caused. I would like to thank all the members of the CMI group which names I have not mention yet for the nice and pleasant working atmosphere. Special thanks to Esther, Wiebke, Joren, Leon (thanks for biking me home ☺), Mark and Relinde. Many thanks to Freddy for Dutch translation of the summary and Ingmar for his helpful suggestions and comments on Chapter 5. Stephan, thank you for solving all my computer problem and killing the virus, which almost crushed my work discussion. Hans thank you for helping with all the technical problems with the apparatus and for sharing your good humor and enthusiasm with us.

Alku i Justyno dziękuję Wam za pomoc i gościnnosc jaką ofiarowaliscie przyjmujac mnie pod swoj dach na początku mojego pobytu w Utrechcie.

Special thanks go to Hans Meeldijk and Marijn van Huis for the great help in HR-TEM measurements. I appreciate your patience in searching of hemispheres for many long hours.

In addition I would like to thank the following collaborators who have contributed to this thesis: Bruno Grandidier, Christophe Delerue, Corentin Durand and Hai Nguyen from France for their commitment and assistance in STM measurements. Many thanks go out to Sergey and Tosia from Dortmund, thank you for the nice atmosphere you created during my stay. Although the measurements did not give a desire results I enjoy staying in your group and I will never forget your great Russian hospitality.

My thanks also go to Barbara Hendrix. I cordially appreciate your support and taking care of all the bureaucratic details regarding my thesis.

Finally, I would like to thank to my family for the constant support and love. Dziękuję Wam kochani rodzice za troskę i miłośc jaką mi okazujecie. Dziękuję, za to że wspieraliście mnie w każdej sytuacji, co pozwiliło mi przetrwac rozłąkę od rodzinnego kraju. Siostrzyczko moja, dzięki za wszystko a szczególnie za słowa wsparcia i otuchy, kiedy ich najbardziej potrzebowałam.

Podziękowania dla moich przyjaciół i znajomych, a w szczególności Ewci, Estery, Pani Teresy Dreszer, Marty L i Wojtka. Szczególne podziękowania dla Damiana. Dziękuję Ci za Twoją wiarę, wrażliwość i wsparcie.

Curriculum Vitae

The author of this thesis was born on February 12th 1983 in Krapkowice, Poland. On June 11th 2002 she finished High School at biological-chemical profile. In October of that year she started her study in Physics majoring in Medical Physics at Faculty of Physics and Astronomy at University of Wrocław. She obtained her B.Sc. degree in February 27th 2006 by studying the applications of mass spectroscopy in medical physics. During the master study she focused on experimental physics and received M. Sc. degree in June 20th 2007 by studying Scanning Tunneling Microscopy on thin metal layers.

From October 1st 2008 she started her PhD research in the Condensed Matter and Interfaces group of Debye Institute for Nanomaterials Science at Utrecht University. Under the supervision of prof. dr. Daniel Vanmaekelbergh and dr. Celso de Mello Donega, she studied optical and electronic properties of colloidal quantum dots. The research was part of European Seventh Framework Programme FP7 under the name of HERODOT project of Marie Curie Action. The results of her PhD project are described in this thesis and were published in scientific journals. Poster/oral presentations were given at several national and international conferences and meetings.

During her PhD, she supervised one Erasmus Master student (Francesca Pietra) and assisted in Quantum Chemistry classes for first-year students. She also supervised the dye-synthesized solar cell project for second year Bachelor students.